

**Design and synthesis of organic-inorganic hybrid
device materials for mechanical energy harvesting
applications**

*A thesis
submitted in partial fulfilment
of the requirements for the*

Doctorate of Philosophy

By

Sachin Kumar Singh

(20153381)



**Department of Chemistry,
Indian Institute of Science Education and Research (IISER),
Pune, India - 411008**

January 2020

Dedicated to
All Indian Farmers

CERTIFICATE

This is to certify that this dissertation entitled “*Design and synthesis of organic-inorganic hybrid device materials for mechanical energy harvesting applications*” towards the partial fulfilment of the PhD degree Programme at the Indian Institute of Science Education and Research, Pune represents original research carried out by **Mr. Sachin Kumar Singh** at IISER Pune under our supervision. The work presented here or any part of it has not been included in any other thesis submitted previously for the award of any degree or diploma from any other university or institution.

Date: 9th January 2020

Prof. R. Boomi Shankar
(Research Supervisor)

Prof. Satishchandra Ogale
(Research Co-Supervisor)

DECLARATION

I, **Mr. Sachin Kumar Singh**, declare that this written submission represents my ideas in my own words and wherever other's ideas have been included, I have adequately cited and referenced the original sources. I also declare that I have adhered to all principles of academic honesty and integrity and have not misrepresented or fabricated or falsified any idea / data / fact / source in my submission. I understand that violation of the above will cause for disciplinary action by the Institute and can also evoke penal action from the sources which have thus not been properly cited or from whom proper permission has not been taken when needed.

Date: 9th January 2020

Mr. Sachin Kumar Singh
(Reg. No: 20153381)

Acknowledgements

On successful completion of this thesis, it is my pleasure to acknowledge all those who have contributed towards it, be it through encouragement, guidance or support.

I would first like to express my sincere gratitude towards my research supervisor Prof. R. Boomi Shankar and co-supervisor Prof. Satishchandra Ogale for their excellent guidance throughout the course of my doctoral studies. Their understanding behavior, emphasis on the rigorousness of concepts and constant encouragement at every step of the research has allowed me to mould into an independent researcher. I also thank them for permitting me to work on this research problem and encouraging me to cultivate my understanding of the literature. Prof. Satishchandra Ogale is the best role model in Science for me. I have gained immense knowledge from him at morning coffee conversations.

I want to thank my RAC Members, Dr. Manjusha Shelke and Dr. Pramod Pillai for their valuable comments during my annual RAC meetings. Their criticality and attention to detail encouraged me to investigate my claims and understanding of concepts more thoroughly before presenting, whether in written or oral form.

I want to thank all my lab mates for reviewing my work critically, suggesting me with experiments and comforting me during several roadblocks during this long tenure of 5 years. I specially thank the support and help provided by Dr. Subas Muduli, Swati Deswal and Neha Sharma during my Ph.D. tenure.

I can't imagine my Ph.D. with the constant love and support of my family and friends. They have played a very significant role in ensuring that I am always in the best mental health to conduct my research and cope with the failures therein.

I would also like to thank CSIR-NCL-Pune, IIT Bombay and University of Cambridge where a lot of experiments were carried out.

Sachin kumar Singh

Table of Contents

Synopsis	X
Abbreviations	XIII
List of Publications	VI
Chapter 1: Introduction	1-26
1.1 Global Energy Need	1
1.2 Types of renewable energy	4
1.3 Mechanical Energy Harvesting	6
1.4 Nanogenerator	8
1.5 Piezoelectric Nanogenerator	9
1.5.1 Concept and materials	9
1.5.2 Basics of Piezoelectric Nanogenerator	11
1.5.3 Piezoelectric Nanogenerator based on Nanomaterials	12
1.5.4 Piezoelectric Nanogenerator based on Polymer Composite	14
1.6 Triboelectric Nanogenerator	16
1.6.1 Concepts, materials and devices	16
1.7 Characterization of Nanogenerator	19
1.8 Applications of Nanogenerators	20
1.8.1 Self-powered devices, blue energy and micro-nano energy harvester	20
1.9 Plan for the thesis	22
1.10 References	23
Chapter 2: High power mechanical energy harvester based on exfoliated Black phosphorous–polymer composite and its multiple applications	27-55

2.1 Introduction	28
2.2 Experimental Methods	29
2.2.1 Synthesis of Black Phosphorus (BP) nanosheets	29
2.2.2 Fabrication of the flexible piezoelectric composite NG and testing	30
2.3 Characterization techniques	31
2.3.1 Field emission scanning electron microscopy (FESEM)	31
2.3.2 Transmission electron microscopy (TEM)	31
2.3.3 Atomic Force Microscopy	31
2.3.4 X-ray diffraction (XRD)	31
2.4 Result and Discussion	31
2.5 Nanogenerator device architecture and performance	34
2.6 Piezoresponse force microscopy (PFM) studies	42
2.7 Computational Density functional theory (DFT) calculations	43
2.8 Device applications	46
2.9 Analyses of experimental results	49
2.10 Conclusions	52
2.11 References	52
Chapter 3: Seed Power: Natural seed and electrospun PVDF nanofiber based triboelectric nanogenerators with high output power density	56-76
3.1 Introduction	57
3.2 Experimental	58
3.2.1 Materials	58
3.2.2 Synthesis of PVDF electrospun nanofibers mat	58
3.2.3 Extraction of glucosinolates and isothiocyanates	58
3.2.4 Characterization of triboelectric layers	59
3.2.5 LCMS analysis of glucosinolates and isothiocyanates	59

3.2.6 Carbohydrate estimation	59
3.2.7 Fabrication of seed based nanogenerator	59
3.2.8 Output performance of Nanogenerator	60
3.2.9 Polarisation and dielectric measurements	60
3.3 Results and discussion	60
3.4 Conclusions	73
3.5 References	73
Chapter 4: A neutral 1D-coordination polymer [Rb(ⁱPr₂N)]_n exhibiting ferroelectric to paraelectric phase transition and mechanical energy harvesting application	77-90
4.1 Introduction	78
4.2 Experimental Section	
4.2.1 Synthesis of 1	79
4.2.2 Preparation of 1-PVA composite films	80
4.2.3 Crystallography	80
4.2.4 Dielectric, Ferroelectric, and Piezoelectric Measurements	80
4.3 Results and Discussions	81
4.4 Conclusion	87
4.5 References	87
Chapter 5: Mechanical energy harvesting using different materials of emergent interest	91-109
5.1 Piezoelectric Nanogenerator based on LFO-PDMS composite film	92
5.1.1 Materials Synthesis and Characterization	92
5.1.2 Ferroelectric and Nanogenerator Measurements	93
5.1.3 Nanogenerator device fabrication and performance	94

5.1.4 Polarization and nanogenerator performance	94
5.2 Triboelectric Nanogenerator based PLD grown MoS ₂ /h-BN thin films	96
5.2.1 Materials Synthesis and Characterization	96
5.2.2 TENG Results of MoS ₂ /h-BN thin films	98
5.3 Triboelectric Nano-generator based PLD grown Max thin film	100
5.3.1 Materials Synthesis and Characterization	101
5.3.2 Fabrication and testing of MAX –TENG	102
5.4 Conclusions	104
5.5 References	105
Chapter 6: Thesis conclusion and future perspectives	110-111
6.1 Thesis summary	110
6.2 Future directions	110

Synopsis

Use of electronic devices has become an integral part of our day to day activities; a major part of it is associated with storing, receiving, and sending information. The domains of piezoelectricity and triboelectricity (friction) are two important phenomena, which are majorly employed in harvesting mechanical energy through devices known as piezoelectric nanogenerators (NG) and triboelectric nanogenerators (TENG). The former one deals with mechanical impact, vibration or deformation-induced changes in electric polarization and the corresponding voltage and displacement current output. The latter one deals with a real charge separation between two material systems driven by different frictional avenues. Herein, we describe the fabrication of piezoelectric/triboelectric nanogenerators of polymer composites composed of organic/inorganic materials and naturally occurring (green) precursors. The present thesis deals with materials and device developments to harness, store and apply mechanical energy around us.

Chapter 1: Introduction

The introduction draws out an overview of the contemporary status of energy research and scientific advancements made so far. The chapter presents the worldwide distribution of energy consumption and increasing demands, large dependence on non-renewable sources of energy and an imminent call towards developing a new green energy harvesting system. The chapter principally focuses on harvesting different kinds of mechanical motions towards realizing a new and clean energy harvesting system. Concept of nanogenerators and its various types viz. piezoelectric, pyroelectric and triboelectric are comprehensively laid down. Towards the end, the broad applications of nanogenerators in self-powered systems and blue energy is highlighted. The chapter is finally concluded with the scope of the current thesis research.

Chapter 2: High power mechanical energy harvester based on exfoliated black phosphorous–polymer composite and its multiple applications

In this chapter, we demonstrated that a uniformly dense dispersion of few-layer BP (FLBP) nanosheets in PDMS (Polydimethylsiloxane) matrix, with a high 2D-dielectric interface density, renders a unique composite which exhibited a remarkably strong mechanical

energy harvesting effect. The 2D BP nanosheets were found to exhibit a fairly high piezoelectric coefficient of ~ 20 pm/V as revealed by Piezoresponse Force Microscopy (PFM). First-principles DFT calculations suggested the existence of strain-induced polarization via deformation-induced redistribution of intra-layer electron charge density. We outlined a synergistic multi-mechanism effect as the cause of the strength of the observed effect.

Chapter 3: Seed Power: Natural seed and electrospun PVDF nanofiber based triboelectric nanogenerators with high output power density

In this chapter, we explored a simple TENG device design based on natural seeds in an attempt to move toward a greener approach to mechanical energy harvesting. The choice of seeds was based on a common experience that mustard seeds get easily charged up and dance in a plastic container when shaken. The design involved a counter-electrode in the form of electrospun PVDF nanofibers, which are triboelectrically negative. The mustard (flax) seed based TENG was shown to render a very impressive power density of 334 mW m^{-2} (324 mW m^{-2}). The high powering capability of the mustard-based S-TENG was clearly established via flash lightning of 120 LEDs following 60 s charging of the device.

Chapter 4: A neutral 1D-coordination polymer $[\text{Rb}(\text{Pr}_2\text{N})]_n$ exhibiting ferroelectric to paraelectric phase transition and mechanical energy harvesting application

In this chapter, a piezoelectric nanogenerator composed of organic-inorganic hybrid ferroelectric material, a 1D-coordination polymer of di-isopropyl imido rubidium assembly, was synthesized and studied for mechanical energy harvesting application. A good ferroelectric response was displayed by the compound which exhibited a remnant polarization value of $2.7 \mu\text{C}/\text{cm}^2$. The mechanical energy harvesting device fabricated by the inclusion of this compound in poly vinyl alcohol matrix furnished an open circuit voltage of 20 V.

Chapter 5: Mechanical energy harvesting using different materials of emergent interest

In this chapter, we scanned several specially engineered materials for NG and TENG applications. One such study involved the use of a multi-ferroic LuFeO_3 in nanoparticle and nanofibre forms with differing hexagonal (h) and orthorhombic (o) phase contributions. Impressive nanogenerator performance was noted with the nanofibers. Similarly, other interesting materials such as inorganic halide perovskites (FAPbBr_3 , $\text{MoS}_2/\text{h-BN}$ 2D/2D

composite films etc.) and their new device concepts were also examined for their viability for mechanical energy harvesting.

Abbreviations

AFM	Atomic Force Microscopy
BTO	Barium titanate
BFO	Bismuth Ferite
CCDC	Cambridge Crystallographic Data Centre
cm	centimeter
DFT	Density Functional Theory
DMF	N, N-Dimethyl formamide
DMSO	Dimethyl sulphoxide
DSC	Differential Scanning Calorimetry
E_c	Coercive field
FT-IR	Fourier Transform Infrared Spectroscopy
FESEM	Field Emission Scanning Electron Microscopy
FTO	F-Doped Tin Oxide
Hz	Hertz
ITO	Sn-Doped Indium Oxide
I_{sc}	Short Circuit Current
MeOH	Methanol
mg	Milligram
MOF	Metal-Organic Framework
M.P.	Melting Point
NCs	Nanocrystals
NMR	Nuclear Magnetic Resonance
PET	Polyethylene Terephthalate
P_r	Remnant Polarization
P_s	Saturation Polarization
PVA	Poly Vinyl Alcohol
PVDF	Polyvinylidene difluoride
PXRD	Powder X-ray Diffraction

PZT	Lead Zirconate Titanate
RT	Room Temperature
SCXRD	Single Crystal X-ray Diffraction
T_c	Curie Temperature
TGA	Thermogravimetric Analysis
HRTEM	High Resolution Electron Microscopy
VB	Valance Band
V_{oc}	Open Circuit Voltage

List of Publications

1. **Singh, S. K.**; Muduli, S.; Dhakras, D.; Pandey, R.; Babar, R.; Singh, A.; Kabra, D.; Kabir, M.; Boomishankar, R.; Ogale, S., High power mechanical energy harvester based on exfoliated black phosphorous–polymer composite and its multiple applications. *Sustainable Energy & Fuels* 2019, 3 (8), 1943-1950.
2. **Singh, S. K.**; Kumar, P.; Magdum, R.; Khandelwal, U.; Deswal, S.; More, Y.; Muduli, S.; Boomishankar, R.; Pandit, S.; Ogale, S., Seed Power: Natural Seed and Electrospun Poly(vinyl difluoride) (PVDF) Nanofiber Based Triboelectric Nanogenerators with High Output Power Density. *ACS Applied Bio Materials* 2019, 2 (8), 3164-3170.
3. Chaturvedi, S.; **Singh, S. K.**; Shyam, P.; Shirolkar, M. M.; Krishna, S.; Boomishankar, R.; Ogale, S., Nanoscale LuFeO₃: shape dependent ortho/hexa-phase constitution and nanogenerator application. *Nanoscale* 2018, 10 (45), 21406-21413. (S. Chaturvedi and S. K. Singh contributed equally to this work)
4. Parmar, S.; Biswas, A.; **Kumar Singh, S.**; Ray, B.; Parmar, S.; Gosavi, S.; Sathe, V.; Janay Choudhary, R.; Datar, S.; Ogale, S., Coexisting 1T/2H polymorphs, reentrant resistivity behavior, and charge distribution in MoS₂-hBN 2D/2D composite thin films. *Physical Review Materials* **2019**, 3 (7), 074007.
5. Deswal, S.; **Singh, S. K.**; Rambabu, P.; Kulkarni, P.; Vaitheeswaran, G.; Praveenkumar, B.; Ogale, S.; Boomishankar, R., Flexible Composite Energy Harvesters from Ferroelectric A₂MX₄-Type Hybrid Halogenometallates. *Chemistry of Materials* 2019, 31 (12), 4545-4552.
6. Pandey, R.; Sb, G.; Grover, S.; **Singh, S. K.**; Kadam, A.; Ogale, S.; Waghmare, U. V.; Rao, V. R.; Kabra, D., Microscopic Origin of Piezoelectricity in Lead-Free Halide Perovskite: Application in Nanogenerator Design. *ACS Energy Letters* 2019, 4 (5), 1004-1011.
7. Ravi, V. K.; Santra, P. K.; Joshi, N.; Chugh, J.; **Singh, S. K.**; Rensmo, H.; Ghosh, P.; Nag, A., Origin of the Substitution Mechanism for the Binding of Organic Ligands on the Surface of CsPbBr₃ Perovskite Nanocubes. *The Journal of Physical Chemistry Letters* **2017**, 8 (20), 4988-4994.

8. Mungi, C. V.; **Singh, S. K.**; Chugh, J.; Rajamani, S., Correction: Synthesis of barbituric acid containing nucleotides and their implications for the origin of primitive informational polymers. *Physical Chemistry Chemical Physics* **2018**, *20* (31), 20734-20734.
9. Abhijit Biswas, A. S., Umashankar Rajput, **Sachin Kumar Singh**, Vivek Antad, Swati Parmar, Dibyata Rout, Aparna Deshpande, Sunil Nair and Satishchandra Ogale, Growth, Properties and Applications of Layered Nanolaminate Ti_3AlC_2 MAX Phase Thin Films. *Physical Review Applied* **2019**, (Under Review)

Chapter 1

Introduction

Abstract

The introduction draws out an overview of the contemporary status of energy research and scientific advancements made so far. The chapter presents the worldwide distribution of energy consumption and increasing demands, large dependence on non-renewable sources of energy and an imminent call towards developing a new green energy harvesting system. The chapter principally focuses on harvesting different kinds of mechanical motions towards realising a new and clean energy harvesting system. Concept of nanogenerators and its various types viz. piezoelectric, pyroelectric and triboelectric are comprehensively laid down. Towards the end, the broad applications of nanogenerators in self-powered systems and blue energy is highlighted. The chapter is finally concluded with the scope of the current thesis research.

1.1 Global Energy Need:

In the present scenario, the domain that has attracted the utmost research attention is energy. In this fast age of development, we are the victims of the energy crisis. Our energy demands depend on limited natural sources to power up industries, home appliances and transportations. Natural resources (Oil, Natural Gas, Coal, etc.) are dying out very fast as our energy consumption is increasing.¹ These natural forms of energy are being depleted due to their excessive usage. Natural resources such as fossil fuels undergo incomplete combustion because of which fossil fuels are a severe concern for the environmental safety, for example, air pollution and emission of carbon dioxide (CO₂) and other hazardous gases are dangerous for human beings and other living species. Figure 1 shows the consumption of energy worldwide. The world must reduce its dependence on fossil fuels and try to transit towards lower-carbon energy resources. It is

reported that world energy consumption has increased by 2.9% in 2018, which is the highest since 2010 and has almost doubled the ten-year average (Figure1).²The energy sector is the primary constraint for global socio-economic growth. Every aspect of human life has been simplified by technology, starting from industrial growth to medicinal diagnostics. The sector-wise consumption of energy analysis shows that most of the energy consumption is mainly in the industrial sector, which is followed by the transport sector. The domestic industry occupies 22% of total energy which highlights mostly the rapid urbanization as well as the technology dependence of modern living.³

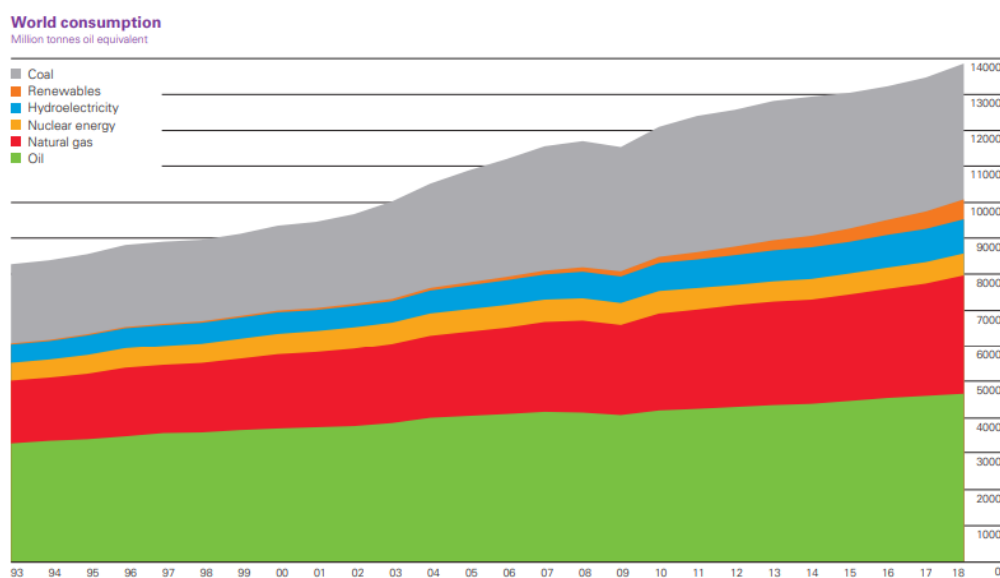


Figure 1 Layout of World energy consumption over the years

(<https://www.bp.com/content/dam/bp/business-sites/en/global/corporate/pdfs/energy-economics/statistical-review/bp-stats-review-2019-full-report.pdf>)

The growing demand for electrical energy in the entire world is shown in Figure 2, per capita, energy demand is the highest for the developed countries like America. Also, a developing nation like India, per capita energy demand is increasing significantly. (Figure 3) Therefore, to fulfill this requirement in the near future, energy harvesting from various renewable sources

(along with the existing fuel sources) should be achieved, and the required technologies should be developed. Per capita, energy consumption has increased from 19,599 Megajoules in 2011-12 to 23,555 Megajoules in 2017-18. The annual increase in per capita energy for 2017-18 over 2016-17 is 3.87%.^{4,5}

This calls for the energy conservation and preservation of natural resources for the present and future generations. The energy resources are classified into the following categories:

- a) Renewable - The naturally occurring resources which are present in the abundant amount and do not possess the threat of extinction are called as renewable energy resources such as Solar, Wind, Geothermal, Tidal and so on.
- b) Non-renewable – The non-renewable energy resources are the ones which were formed by fossil fuels such as coal, petroleum and natural gas. These were formed in the earth’s crust after the decomposition of organic matter for millions of years. These resources have limited reserves and possess the danger of getting exhausted if used unlimited. If they continue to be consumed at a rapid pace which is the scenario in today’s high technology-dependent and advanced society, they will be exhausted, and the generations to come will never get to utilize them. Apart from this, the pollution caused by burning fossil fuels has turned out to be a significant environment-related threat in this era, as mentioned earlier.^{6,7}

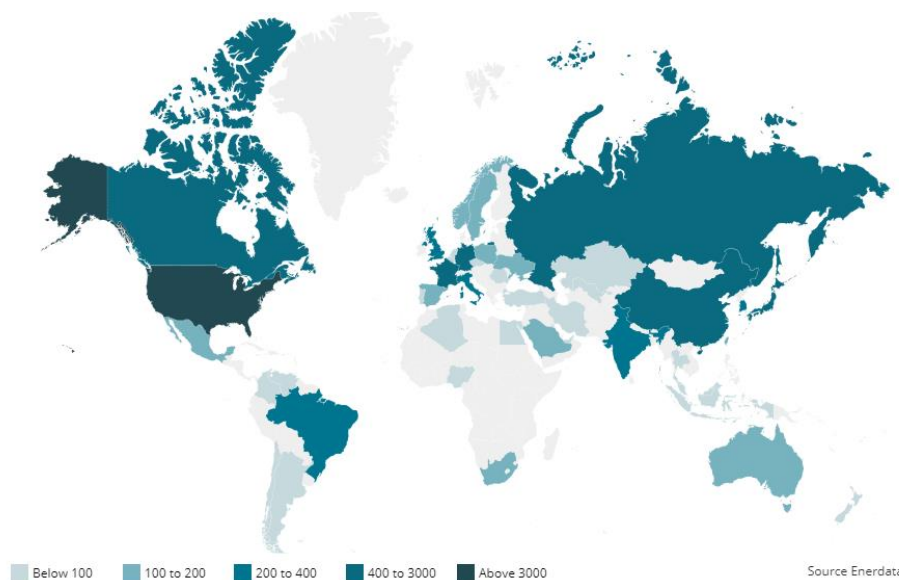


Figure 2 *Worldwide electrical energy consumption* (Source: IEA (2018), World Energy Statistics/ Renewable energy Statics. All rights reserved to IEA

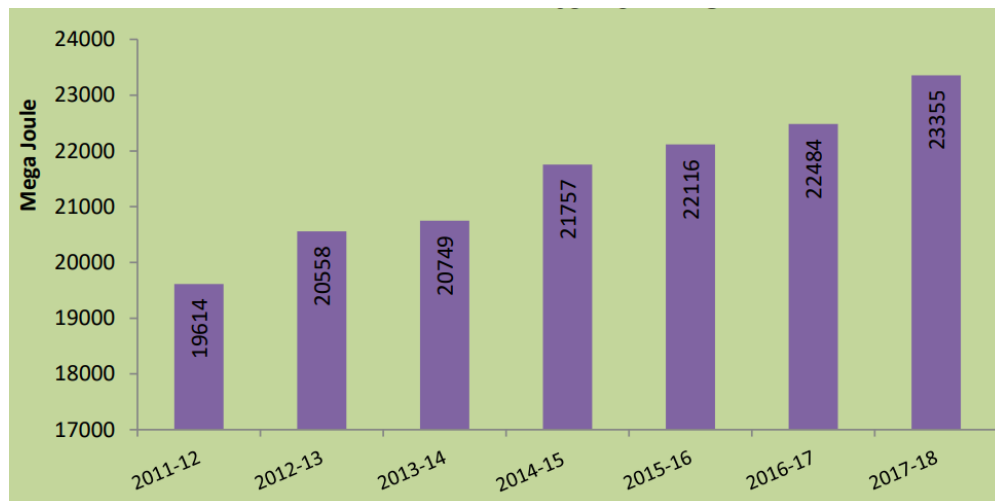


Figure 3 Per-capita Energy Consumption (Copyright © 2020 Ministry of Statistics & Programme Implementation)

(http://www.mospi.gov.in/sites/default/files/publication_reports/Energy%20Statistics%202019-finall.pdf)

1.2 Types of renewable energy

The new class of sources for clean energy harvesting are solar, wind, geothermal heat and ocean energy. Importantly, these are the renewable energy sources that mean energy harvesting from these sources can be renewable, an extremely important factor for the replacement of fossil fuel energies. Renewable energy is also important for energy security, economic benefits, energy efficiency and importantly, the technological diversification of energy sources. In 2019, the International Renewable Energy Agency (IREA, UAE) reported that to maintain the average enhancement of global temperature below two °C, renewable energy needs to grow six times faster than the current scenario. Herein the various renewable energy storage systems are listed in the form of table 1 below. These have multiple applications in various sectors (Figure 4). This thesis is focused on mechanical energy among multiple forms of renewable energy forms. In this section, the scope of mechanical energy will be described with its importance and benefits.^{8,9}

Table 1 Renewable energy storage systems (Reproduced with the permission of Ref⁸ Copyright 2015, Elsevier.)

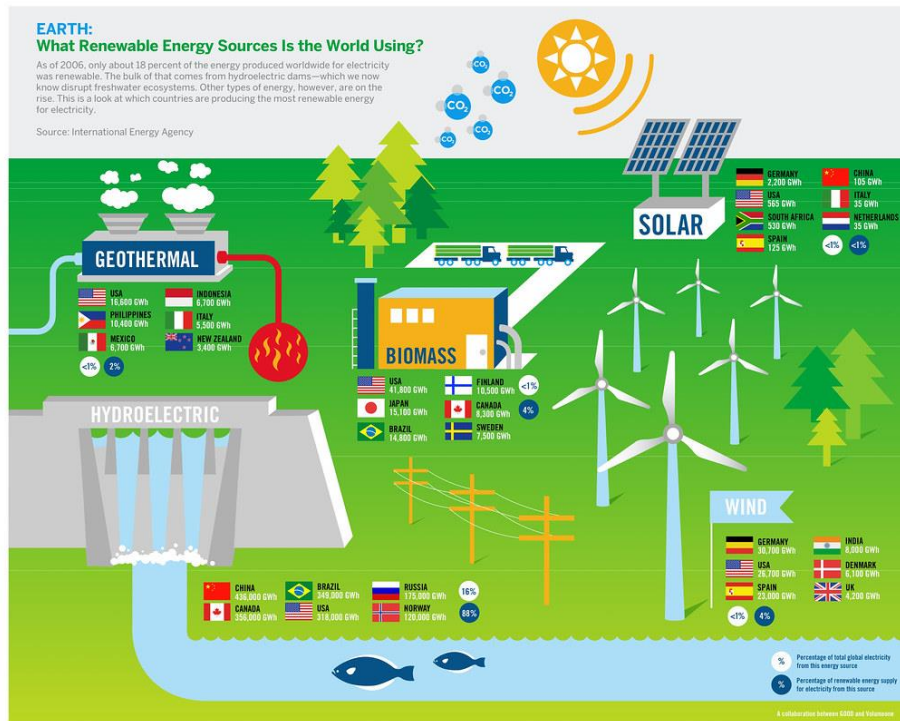
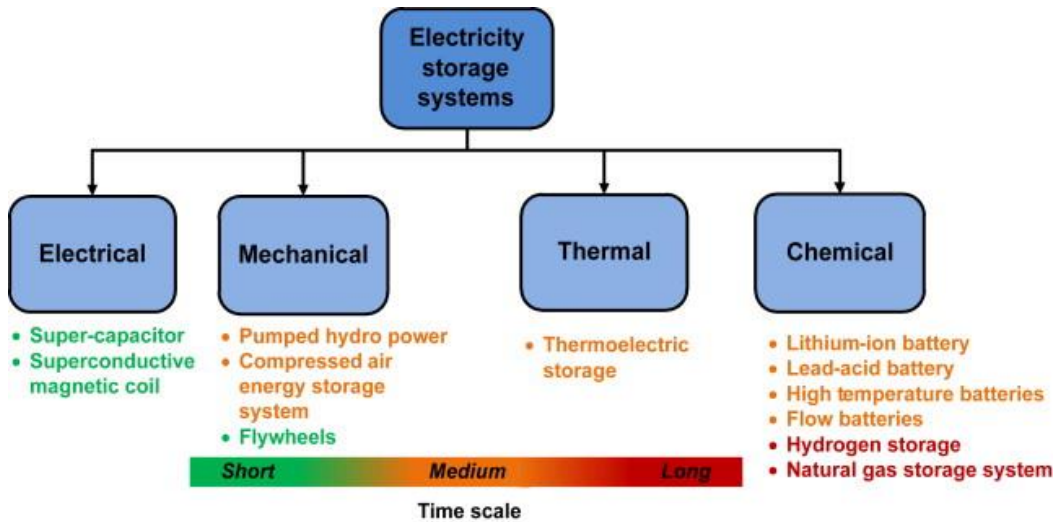


Figure 4 Renewable energy sources (<https://www.flickr.com/photos/goodmagazine/3905443690>)

1.3 Mechanical Energy Harvesting:

Apart from solar energy, thermal energy and electromagnetic induction are very well explored among many. If thousands of sensors are installed in a vast geographical area, then it will be challenging to maintain and exchange batteries at the right time. Self-powered devices will work as great alternatives. Nanodevices or smart gadgets may require small-scale power to operate as the power required is in micro-scale, but as the power requirement increases than cost increases accordingly. In most of the nanodevices, the battery is a great choice, but harvesting energy from surrounding mechanical motions might ultimately replace the battery. It would also extend the lifetime of battery for the sustainable operation.¹⁰⁻¹² An electric device can function as self-powered gadget if it harvests mechanical motions from its surrounding environment and stores this harvested energy into capacitor for later use. For example, a nanosensor is designed to sense surrounding activities, transferring the signals and perform some actions but the main target is to search a power source that can run the nanosensor without adding much weight if a nanorobot which consists of several components such as sensors, actuators and control power is implemented into the body for diagnosing and therapeutic actions.¹³⁻¹⁶ After its injection in the body, it is challenging to replace the battery. Mechanical energy harvesting might apply to solve such problems by using different mechanical vibrations or motions. Various types of mechanical movements exist in our environment (Table 2).¹² Our environment has an ample amount of various kinds of mechanical energy such as wind energy, body motions, ultrasonic waves, blood flow, mechanical vibrations, muscle stretching and wave energy. These sources have different types of characteristics in terms of magnitude and frequency of mechanical motions. In some cases, the magnitude of energy could be less enough to drive conventional energy harvesting technologies because of the insufficient amplitude of the mechanical force. Another factor is the variable frequency of the available signal. Finally, the mechanical vibrations which surround us can fluctuate.¹⁷ The age of smart technology demands for the high adaptability with the environment. The nanogenerator has potential technology from the last 13 years to solve these issues.^{10, 18-22}

Table 2: Mechanical Energy Motions

Human Body Motions	Infrastructures	Industry	Transportations	Environment
Breathing, blood flow/pressure, respiration, walking, arm motion, finger motion, jogging	Bridges, roads, tunnels, farm, house structure, control-switch, water/gas pipes, AC system	Motors, compressors, chillers, pumps, fans, vibrations, cutting and dicing, noise	Aircraft, automobile, train, tires, tracks, peddles, brakes, turbine engine, vibration, noises	Wind, ocean current/wave, acoustic wave

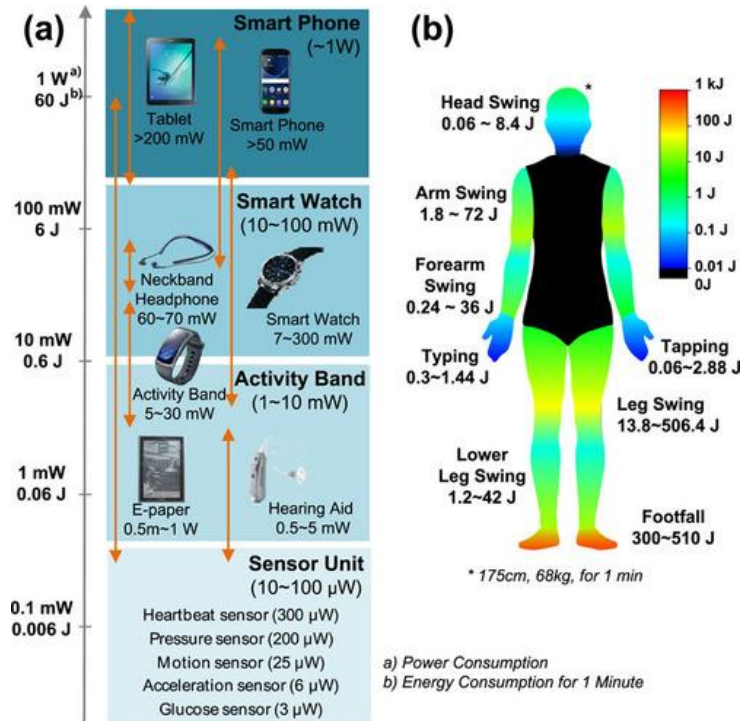


Figure 5 (a) Energy required for smart gadgets (b) Energy from different human motions
 Reproduced with the permission of Ref²³ Copyright © 2017, AIP Publishing.

1.4 Nanogenerator

In 2006, Prof. Zhong Lin Wang's group at Georgia Institute of Technology had demonstrated nanogenerator for the self-powered system for the first time. Zinc Oxide nanowires based nanogenerator were used to convert random mechanical energy into electrical energy. The mechanism of the nanogenerator describes by piezoelectric potential generated in piezoelectric nanowires by external strain.²⁴⁻²⁸ Currently, Nanogenerators have been extensively studied in this context.^{29, 30} The huge number of piezoelectric materials has been demonstrated for many applications such as sensors, transducers, actuators etc. in various fields.³¹ However, research on the use of piezoelectricity for energy harvesting purposes has expanded rapidly during the last decade. These energy harvesters can be used to acquire mechanical signals even from the ambient sources in the living environment. Most of the studies demonstrate the use of piezoelectric-semiconducting materials from the Wurtzite family.^{32, 33} These piezoelectric energy harvesters are commonly termed as nanogenerators. Much advancement has been made in the domain of piezoelectric nanogenerators (PENG) recently through the use of simple fabrication processes, leading to high mechanical stability and higher piezoelectric output. Numerous applications of this technology have been demonstrated such as self-powered nanosystems, multiple energy harvesting systems, NG as active sensors etc.³⁴ The critical points for the commercialization of this technology include the development of integration of the system, low cost and large scale fabrication processes as well as the power management circuits. Another useful point is the fundamental understanding of the nanoscale size effects of various piezoelectric materials on their properties. Among these nano-generators, triboelectric nanogenerators (TENG) have attracted significant attention due to their high output as well as energy conversion efficiency. In 2012, Prof. Zhong Lin Wang's group at Georgia Institute of Technology had demonstrated this new type of nanogenerator for the first time.³⁵⁻⁴⁰ This TENG has become a potential research area since then as there is minimal literature on the same. A conventional TENG converts external mechanical energy into electricity. The mechanism of energy conversion is based on the conjunction of the triboelectric effect and electrostatic induction.⁴¹⁻⁴³

Nanogenerators are divided mainly into four categories on the basis of their working mechanism. (Figure 6)

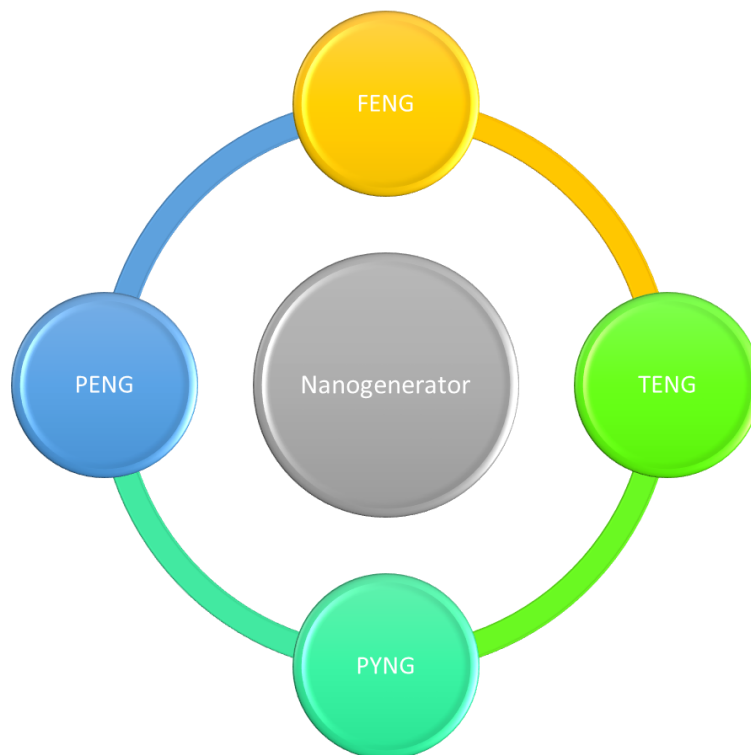


Figure 6 *Types of Nanogenerators.*

- i) Piezoelectric which generates electric pulses when subjected to strain in structure. (PENG).
- ii) Triboelectric which exploit the friction between two different material interfaces to generate suitable voltage and current density (TENG).
- iii) Pyroelectric involves the conversion of heat into electricity (PYNG).
- iv) Flexoelectric is the generation of an electric polarization response under a mechanical strain gradient (FENG).

1.5 Piezoelectric Nanogenerator (PENG):

1.5.1 Concept and materials:

Piezoelectric nanogenerators are good candidates for energy harvesting, as they are cost-effective and highly durable as compared to triboelectric generators.^{26, 44, 45} Oxides and polymers are used in piezoelectric generators because they are non-centrosymmetric and show the change in polarization under the external pressure.^{46, 47} Dielectric materials are electrical insulators, and they are categorized into three types based on crystal classes (Figure 7(a)).

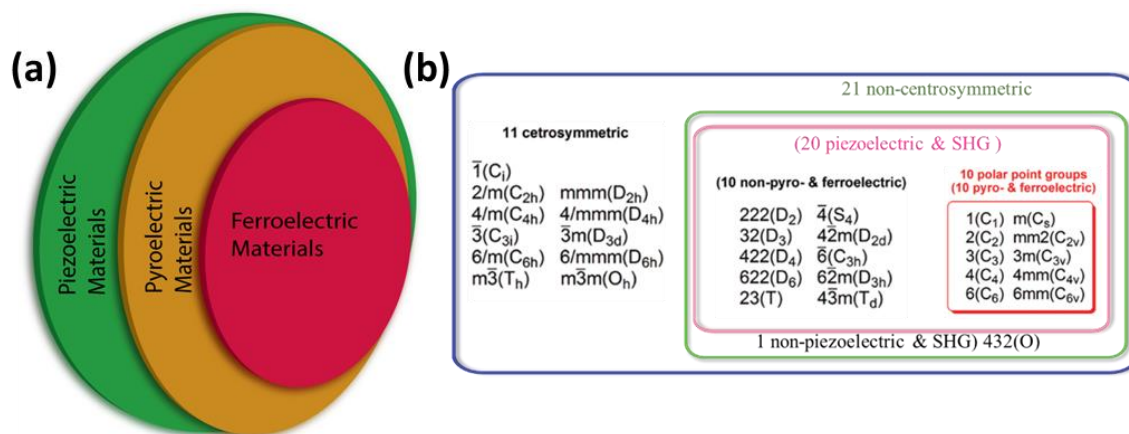


Figure 7 Classification of dielectric with crystal classes (Reproduced with permission from Ref⁴⁸ Copyright © 2012, American Chemical Society).

Out of the 32 crystal classes of dielectric crystals, 11 are centro-symmetric, 21 classes belong to the non-centro-symmetric point groups. Among these classes, only non-centrosymmetric point group based crystals show ferro, piezo as well as pyroelectric properties. Out of these 21 non-centrosymmetric point groups, 10 align in unique polar directions, which exhibit piezo, pyro and ferroelectricity and remaining 10 non-polar point groups are only piezoelectric active point groups (Figure 7(b)). So, it is clear that all the ferroelectric materials are simultaneously pyroelectric as well as piezoelectric. Likewise, all pyroelectric materials are piezoelectric, but not all of them are ferroelectric.^{48, 49}

i) Ferroelectric Materials Polar non-centrosymmetric systems which undergo switchable polarization in the presence of external electric field and display P-E hysteresis (Figure 8(a)). Such types of compounds are termed as ferroelectric materials - examples: PZT, PMN-PT, PVDF etc.⁴⁹

ii) Piezoelectric Materials: Materials which possess non-centrosymmetric crystal lattice are known as piezoelectric materials. Piezoelectric materials exhibit both direct piezoelectric effect (generation of electric charges on the application of mechanical force) and converse piezoelectric effect (Figure 8(b)) (production of the internal strain in the material on application of the electric field).⁴⁹

Examples of piezoelectric materials:

Inorganic materials: Zinc Oxide (ZnO), GaN(Gallium Nitride), InN(Indium Nitride), Lead zirconate titanate (PZT), Barium titanate (BTO) etc.

Organic Materials: Diisopropylammonium bromide (DIPAB), Croconic acid etc.

Polymers: Polyvinyl difluoride, Nylon-6 etc.

Organic-inorganic hybrid: Methyl ammonium lead Iodide (MAPbI₃), Formamidinium lead bromide (FAPbBr₃).

iii) Pyroelectric Materials

Pyroelectric materials are ten polar crystal classes, which show both piezoelectric and ferroelectric properties. Temperature gradient (dT/dt) leads to spontaneous polarization in the materials due to the displacement of electric dipoles inside the pyroelectric materials (Figure 8(c)).⁵⁰

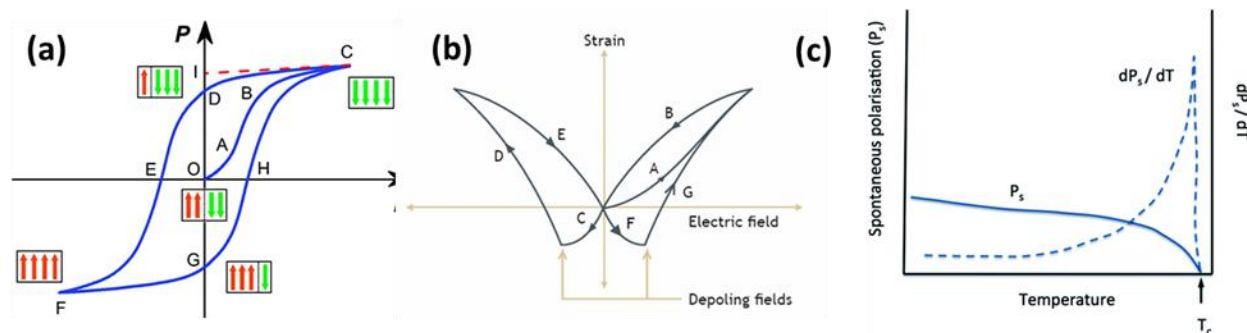


Figure 8 (a) PE hysteresis loop (b) Butterfly loop of strain versus electric field (c) Spontaneous polarisation with a temperature gradient (Reproduced with permission from Ref^{48, 50} Copyright © 2012, American Chemical Society) and Copyright, 2014, Royal Society of Chemistry.

<http://www.noliac.com/tutorials/piezo-basics/properties-of-piezoceramic-material-at-high-field/>

1.5.2 Basics of Piezoelectric Nanogenerator

Applying mechanical stress to piezoelectric material results in the deformation of the crystal lattice due to non-centrosymmetric; hence polarization occurs in the system (Figure 9 (a) and (b)). This built-in polarization will induce a potential difference at different edges of the system, which will result in producing a voltage difference and thus showing a net output voltage. Based on this principle, therefore, mechanical energy can directly be converted into electricity.

Therefore, fabricating a device based on such a mechanism will be advantageous for the smart technology.^{11, 25}

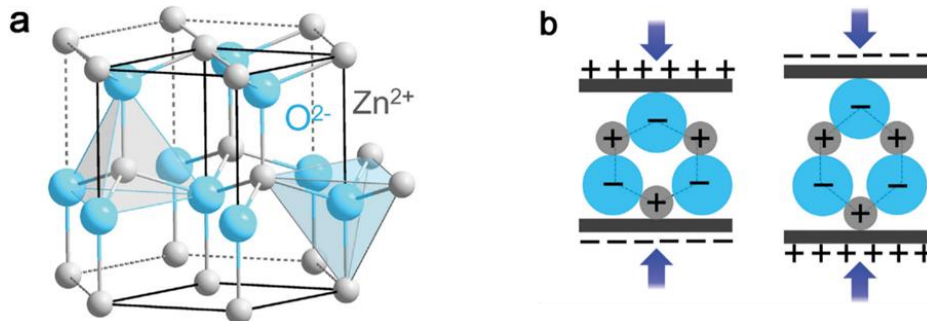


Figure 9 (a) asymmetric crystal lattice, which has a hexagonal unit cell with space group $C6mc$ (b) Polarization in crystal after deformation (*Reproduced with permission from Ref⁵¹ Copyright 2016 Wiley-VCH Verlag GmbH & Co.*)

1.5.3 Piezoelectric Nanogenerators based on Nanomaterials:

i) Zinc Oxide (ZnO)

In 2006, Z.L. Wang exhibited first Piezoelectric Nanogenerator based Zinc Oxide (ZnO) nanowires (NW). A conductive atomic force microscopy tip at contact mode was used to deflect aligned ZnO NWs. During the scanning over the top of ZnO NWs, The measured output voltage was around 6-9 mV. The mechanism was explained based on the coupling of semiconductor and piezoelectric properties (Figure 10(a) to (e)). The Schottky barrier between Si-based AFM tip and ZnO NWs served as a rectifying ‘gate’ that led to electrical charge generation.⁵²⁻⁵⁴

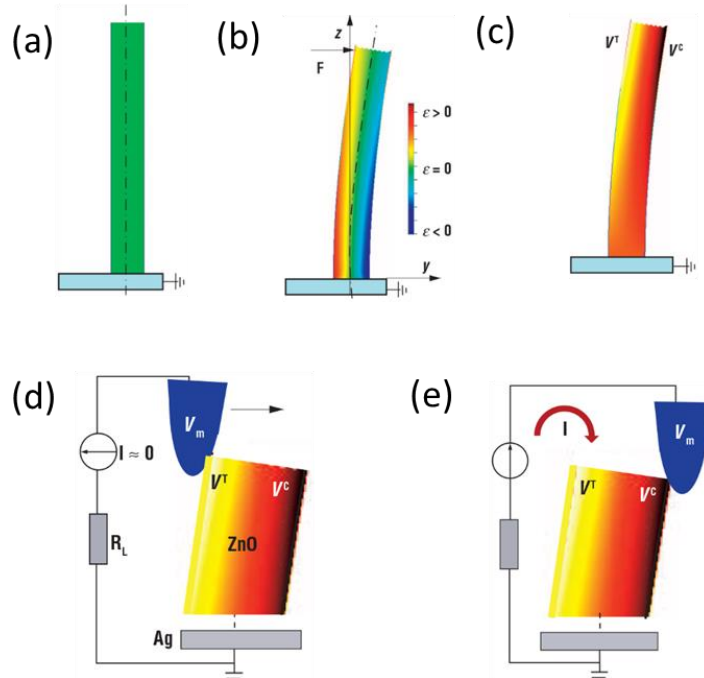


Figure 10 (a), (b), (c) and (d) Direct measurements of the asymmetric voltage distribution on the tensile and compressive side surfaces of ZnO wire (with permission from Ref⁵⁵ IEEE copyright line © 2011 IEEE).

For flexible, robustness and stability in PENG devices, Yang et al. established a single ZnO NW incorporated on flexible Kapton substrate and fully packed with polydimethylsiloxane (PDMS) (Figure11). The output performance of flexible PENG was increased compared to previous work. On the application of cyclic stretching-releasing of the piezoelectric nanowire with a strain of 0.05-0.1% results in an oscillating output voltage of up to 50mV.⁴⁶

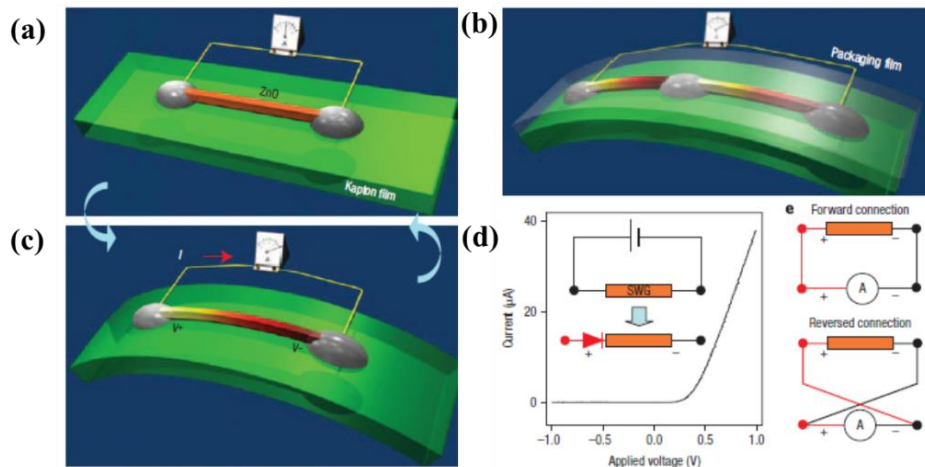


Figure 11 *Design of a piezoelectric Nanogenerator on a flexible substrate and switchable polarity test (with permission from ref⁵⁶ Copyright © 2008, Springer Nature)*

Till date, Piezoelectric output power performance of ZnO based devices is enhanced by a different type of architecture of the nanogenerator.^{26, 44, 56, 57}

1.5.4 Piezoelectric Nanogenerator based on Polymer Composite:

Numerous ceramic perovskite materials (for example PZT, BFO etc.) are conventionally used for piezoelectric applications. Excellent dielectric and piezoelectric properties of these materials are exceedingly important the harvesting energy from mechanical sources. In a broader perspective, it is difficult to fabricate devices with soft material due to brittle and rigid nature of inorganic perovskites. Hence it is of great importance to flexibility, durability and stretchability in devices with high performance for scalable applications.⁵⁸⁻⁶¹

Researchers have developed high-performing flexible piezoelectric Nanogenerator via inclusion with different polymers using simple methods. Flexible PENG based on polymer nanocomposite can be fabricated by following process 1) a simple blending 2) nanocrystal growth within a polymer matrix 3) In- situ polymerization in the presence of nanoparticles.⁶¹⁻⁶³

i) FAPbBr₃-PDMS polymer composite based piezoelectric Nanogenerators:

Ding et al. have fabricated a high-performance, flexible PENG based FAPbBr₃-PDMS polymer composite films. Uniform distribution of FAPbBr₃ nanoparticles into PDMS matrix established a freestanding nanocomposite film, which was investigated for ferroelectric characterizations and piezoelectric applications. PENG devices were fabricated by sandwiching the composite film between aluminium foil and ITO-coated PET substrate (Figure 12 (a) to (c)). Vertical compression of 0.5MPa at 6Hz frequency applied to poled PENG devices at 50kV/cm. A maximum output voltage of 8.5V and a current density of 3.8 $\mu\text{A}/\text{cm}^2$ was revealed by FAPbBr₃-PDMS based PENG.⁶⁴ (Figure 13(a) and (b))

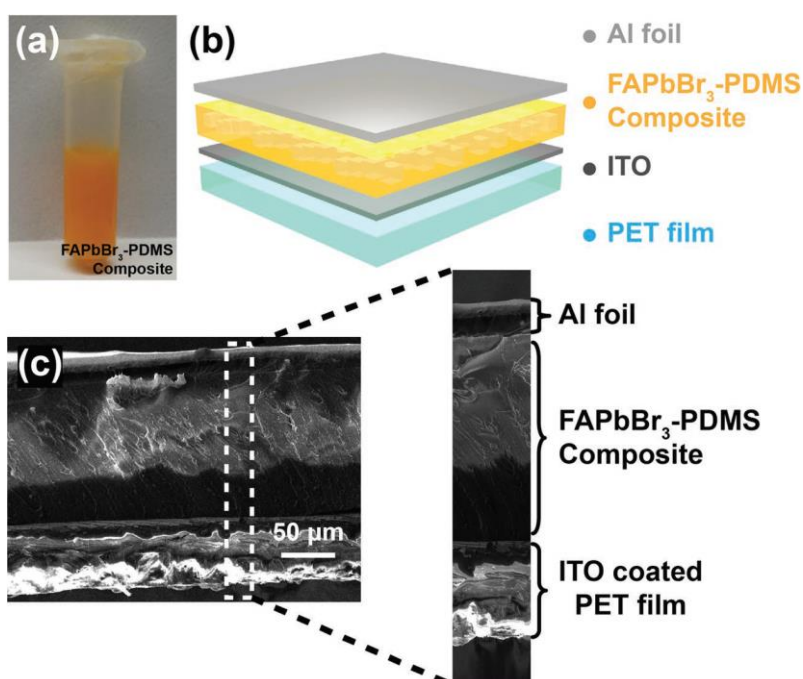


Figure 12 (a) FAPbBr₃-PDMS composite solution. (b) Schematic of fabricated flexible nanogenerator (c) The cross-sectional SEM image of PENG (Reproduced with permission from Ref⁶⁴ Copyright 2016 Wiley-VCH Verlag GmbH & Co.

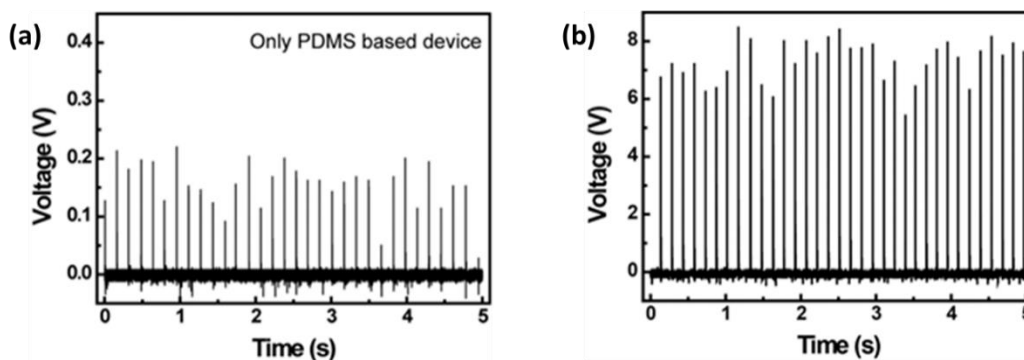


Figure 13 (a) Output voltage of only PDMS based PENG (b) Output voltage from FAPbBr₃ nanoparticle composite nanogenerator. (Reproduced with permission from ref⁶⁴ Copyright 2016 Wiley-VCH Verlag GmbH & Co.).

Organic-inorganic hybrid materials can be a good candidate in piezoelectric and ferroelectric applications because of their impressive dielectric constant.^{65, 66}

1.6 Triboelectric Nanogenerator:

1.6.1 Concepts, materials and devices

A Nanogenerator generates electricity from different mechanical energy sources through the coupling of triboelectrification and electrostatic induction. Contact electrification, also known as triboelectrification, is a common phenomenon in our environment. It creates electrical charges by mechanical contacts between two adequate materials, these charges being temporarily stored in a dielectric layer. The resulting electric fields induce charges of opposite polarity in surrounding conductors. If the geometrical configuration of the triboelectric device varies such as the electric field varies, a varying current can be observed between two conductors linked with an electrical load, generating electrical power. In that sense, triboelectric nanogenerators are similar to electret energy harvesters and sometimes called tribo-electret nanogenerator (TENG).^{36, 37}

Each and every material forms static charges on their surfaces, ubiquitously known as triboelectric charges. Materials which have aptness to loose negative triboelectric charges are triboelectric positive materials and other which acquires negative triboelectric charges on their surfaces are triboelectric negative materials. Triboelectric materials are arranged in triboelectric series according to their quantitative triboelectric charges density (Figure 14).⁶⁷ With the purpose of the best output performance of TENG; one has to choose materials which are far from each other in triboelectric series. The surface charge density of a triboelectric material depends on various parameters, such as molecular functionalization, design as well as their arrangement on

the surface. Moreover, nanomaterials based on composites have played a crucial role to heighten the surface roughness and the charge density of triboelectric materials and also in polymers.^{18, 38,}
68

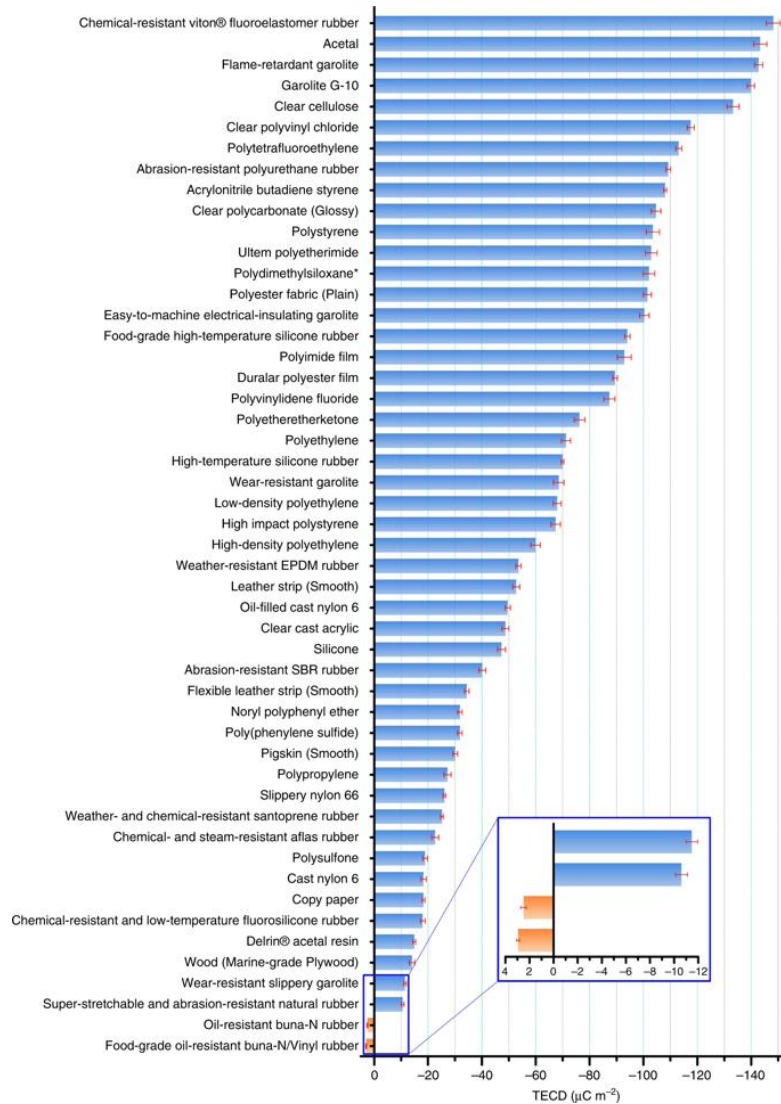


Figure 14 The quantified triboelectric series. (Reproduced with permission from Ref⁶⁷ Copyright © 2019, Springer Nature).

The output power and lifetime of Nanogenerator depend on the relative velocity, stress and friction between the two dielectric layers. There are four basic designs of the triboelectric Nanogenerator (Figure 15):

- a) vertical contact-separation
- b) lateral sliding
- c) single-electrode
- d) Freestanding

Contact separation and lateral electrode designs can be used in harnessing mechanical energy from wind and water waves. Single electrode and freestanding designs are preferred in harvesting mechanical energy from human motions and wheel motions.^{38, 69}

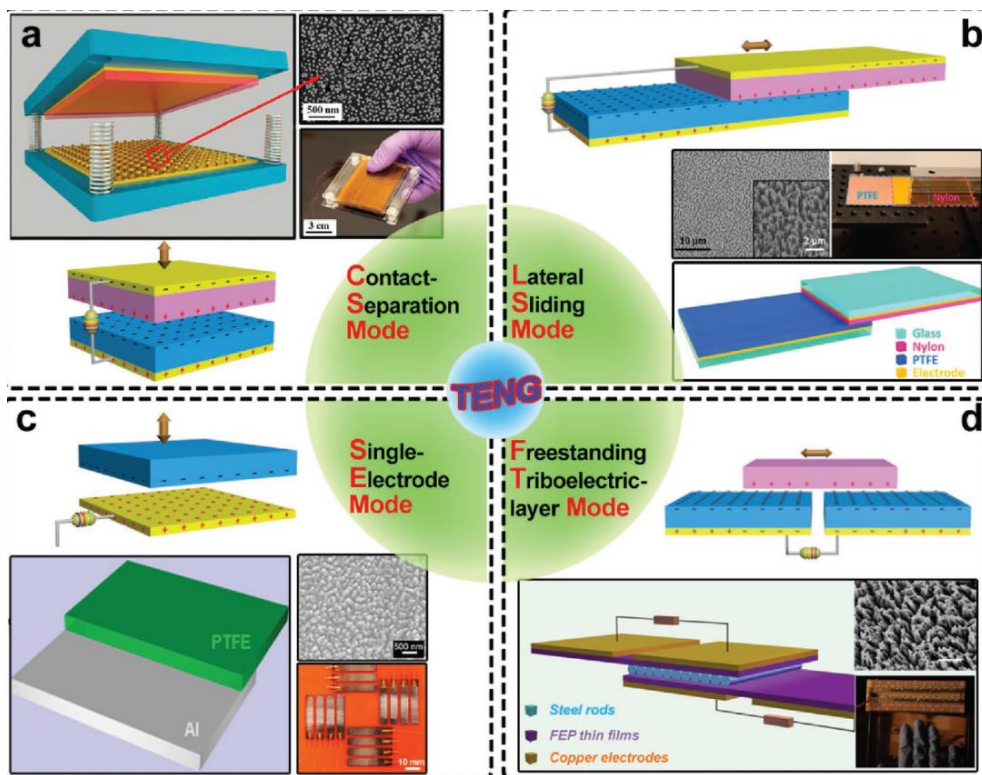


Figure 15 Four working designs of TENG. a) Vertical Contact separation. b) Lateral sliding. c) Single electrode d) Freestanding (Reproduced with permission from Ref⁷⁰ Copyright 2016 Wiley-VCH Verlag GmbH & Co.

a) Vertical contact-separation TENG

In this type of TENG figure (a), two different dielectric layers arrange on two electrodes and face with each other. When an external force is applied on a top-bottom design, dielectric layers

touch each other and transfer of charges occur between the layers. Triboelectric charges will balance the potential difference, and there will be no electric current in output. As external force is removed, it cracks the triboelectric charges between the dielectric layers and hence potential difference generates between the electrodes. Triboelectric potential disappears as the gap is closed, and the electrons flow back.^{43, 71}

b) Lateral sliding TENG

The architecture of LS-TENG is similar to a vertical contact-separation mechanism. In this, triboelectric charges are generated by relative sliding, which introduces lateral polarization along the sliding direction. Potential difference along the sliding path leads to the flow of electrons through load resistance. A periodic sliding motion apart and closing generates positive and negative signals of voltage.^{38, 43}

c) Single electrode TENG

Single electrode TENG has the best utilization in harvesting mechanical energy from mobile objects. In single electrode mode, the bottom electrode of TENG is connected to ground. The local electric field distribution is changed by toward and backwards to and movement of the top layer. The potential of the wire will be maintained through the exchange of electrons in between the bottom electrode and the ground.⁴⁰

d) Freestanding TENG

This type of TENG is based on the principle of designing two symmetric and similar size of electrodes underneath of a dielectric layer. The separation distance between the two electrodes should also be the same as the moving dielectric layer. The approach/departure movement of the dielectric object generates the asymmetric surface charge distribution between the electrodes, which causes oscillation of the electrons to balance the local potential difference. The moving dielectric layer does not need to touch the top electrodes so that free movements are achievable without direct physical contact.⁴¹

1.7 Characterization of Nanogenerator

A typical mechanical energy-harvesting configuration consists of the following components: a PENG/TENG energy converter, measuring unit (Oscilloscope), an energy harvesting circuit (full Wave rectifier), an energy storage device (Figure 16 (a)). The energy harvesting circuit converts the energy produced by the piezoelectric converter from AC to DC or from low voltage to high voltage (Figure 16 (b)).

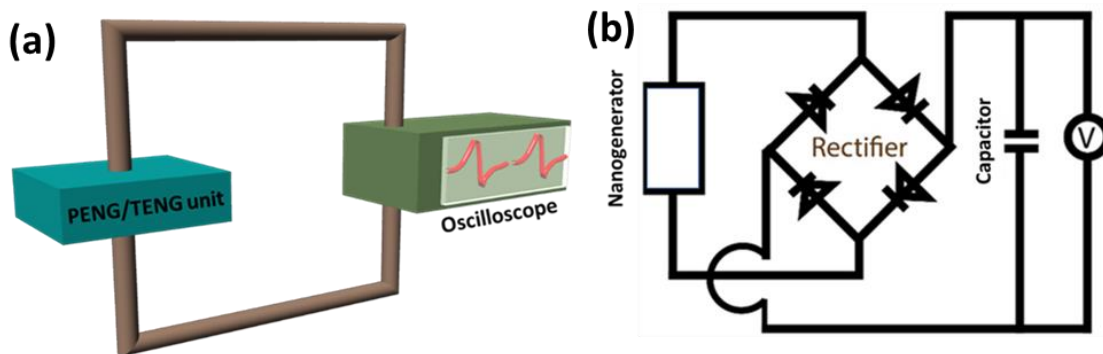


Figure 16 (a) Schematic of measurement set up (b) Full wave rectifier for converting AC current to DC.

1.8 Applications of Nanogenerators

1.8.1 Self-powered devices, blue energy and micro-nano energy harvester

Self-powered devices have been the topic of interest in the past few decades. They are a requirement of the high technology generation. As the world is facing issues related to environmental pollution, global warming and extinction of species due to various change in habitat, there is need of monitoring the ambient environment to optimize the energy consumption at all levels, to minimize the use of fossil fuels and to preserve the non-renewable sources of energy for future generations. For instance, the wind and water energy are unsoiled and extensive types of mechanical energy that are concerned with it may play a substantial role in electricity supply in the future. Global electricity request was recognized by wind power technologies as of the end of 2020. Besides, NGs (Nanogenerators) can be used to power miniature sensors. The self-rechargeable devices such as secondary batteries, supercapacitors etc., are a key for new future devices. They are capable of replacing the batteries in electronic systems and harnessing the renewable energy sources for their operation (Figure 17).⁷²

Furthermore, Wind energy harvesting can be harness using a network of TENGs in the absolute environment While it lacks in case of traditional blade-based winder power generators which work at certain wind speeds, especially in the environment for example in desert areas. TENGs have an advantage over conventional technology because it generates competent output power at low airspeed.

While finishing, TENG is a technologically perfect device because it can harvest low-frequencies and irregular vibrations and have the advantage of producing higher efficiency at low frequencies. Therefore, it can become a very powerful system for water wave-based energy harvesting making blue energy as the potential future energy source (Figure 18).^{73, 74}

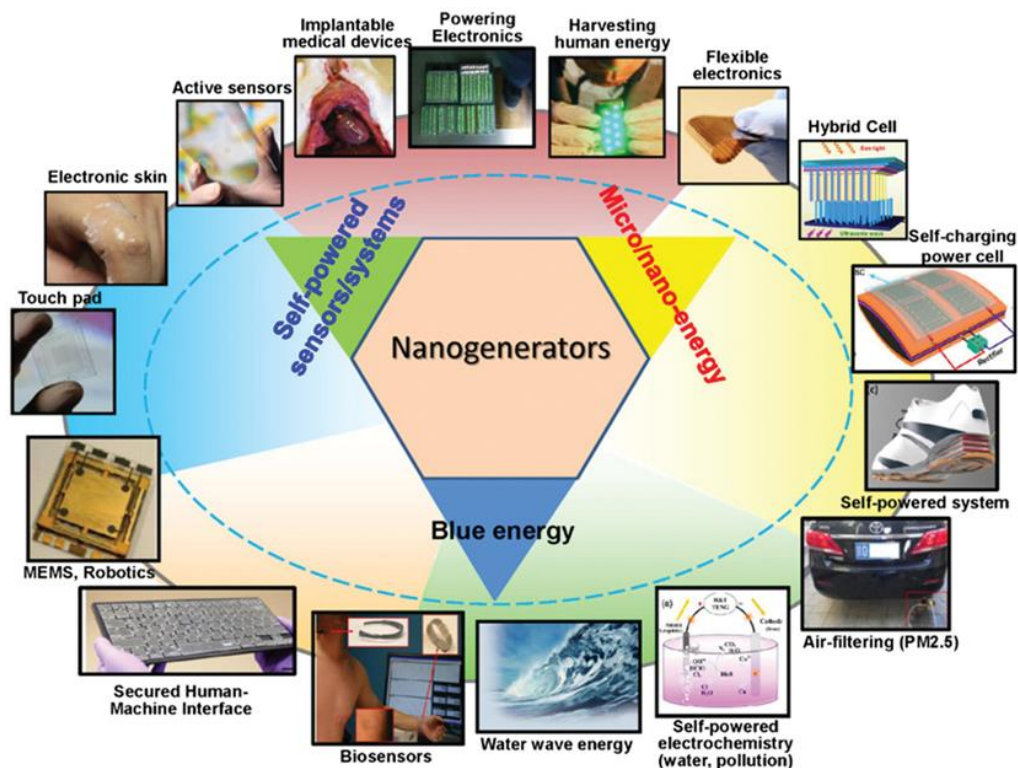


Figure 17 *Broad applications of Nanogenerators (with permission from Ref⁷⁵ Copyright 2018, Elsevier).*

There are three primary directions for different applications:

- Nanogenerators have potential future in clinical applications like monitoring the biomedical conditions of heart patients, for example, pacemakers, blood pressure sensor, pulse sensor and the cardiac sensor which need power from batteries and have the limitations of convenient charging and replacement. So, PENG/TENG as the self-powered device can replace the conventional batteries in them.^{76, 77}
- Human-Machine interface has its importance in artificial intelligence and TENG can be employed in intelligent keyboards, body motion sensors, artificial skin and acoustic sensors which can provide smartness to cyber security, human identifications and robotics.⁷⁶
- Self-powering technology has been developed sustainably by TENG as nano/micropower systems for small gadgets.⁴²

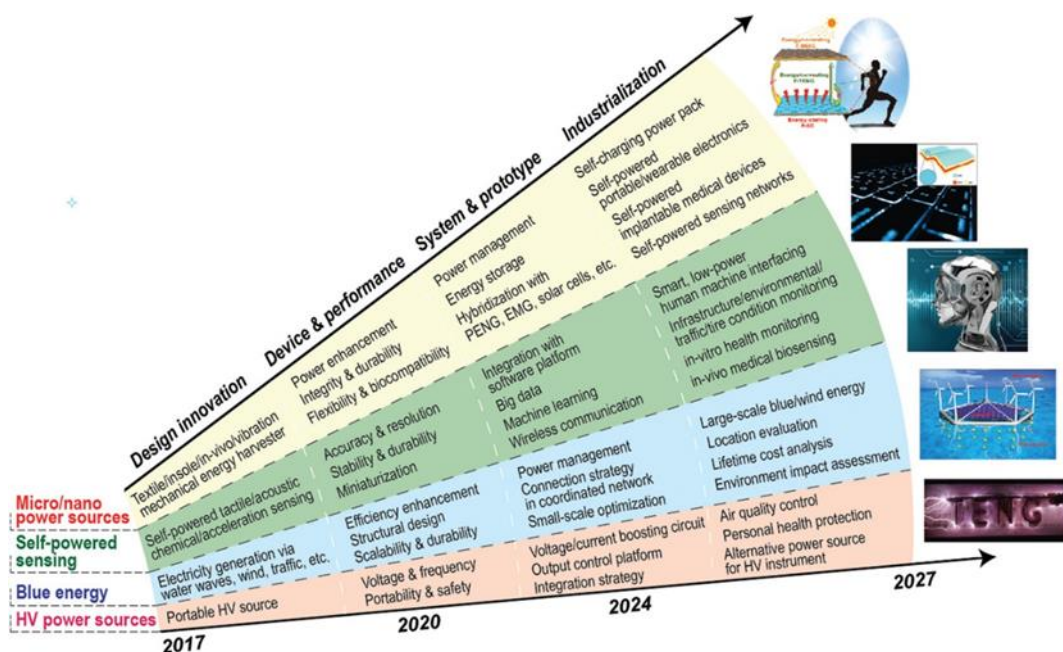


Figure 18 Road map of TENG development from 2017 to 2027 (Reproduced with permission from Ref^{d8} Copyright 2016 Wiley-VCH Verlag GmbH & Co).

1.9 Plan for the thesis

Although Nanogenerator concepts and technologies are rapidly evolving, equal attention has not yet been given to polymer system based flexible platforms, especially those from the natural and environmental sources. In this thesis, we have focused on such nanofiber-based flexible piezoelectric and triboelectric nanogenerator systems, such as polymer composites of 2D materials, natural seeds, synthetic ferroelectric materials and other emergent materials of nanoscale structures.

The **second** chapter presents the methods of synthesis, characterization and device fabrication of a polymer composite of 2D material (few-layer black phosphorus) and their mechanical energy harvesting properties.

The **third** chapter presents the fabrication of triboelectric device architectures composed of PVDF nanofibers (using electrospinning) and the different natural seeds in the other layer. All these devices were tested for their triboelectric energy harvesting application.

The **fourth** chapter presents a simple approach to synthesise a new organic-inorganic hybrid ferroelectric 1D-coordination polymer consisting of Rb cation and diisopropylamine anion and its preliminary response for mechanical energy harvesting application.

The **fifth** chapter presents an exciting designing of different triboelectric nanogenerator devices using a new material system based on nanoscale metal oxides and other hybrid oxides.

The **sixth** chapter concludes the work presented in this thesis and outlines future perspectives.

1.10 References

1. Gozgor, G.; Lau, C. K. M.; Lu, Z., Energy consumption and economic growth: New evidence from the OECD countries. *Energy* **2018**, *153*, 27-34.
2. BP Statistical Review of World Energy. *BP* **2019**, 68.
3. (2019), I., World Energy Outlook 2019. *IEA* **2019**, <https://www.iea.org/reports/world-energy-outlook-2019>.
4. MINISTRY OF STATISTICS AND PROGRAMME IMPLEMENTATION, G., ENERGY STATISTICS. **2018**, (25).
5. consumption, W. e., *Wikipedia* **2019**.
6. Götz, M.; Lefebvre, J.; Mörs, F.; McDaniel Koch, A.; Graf, F.; Bajohr, S.; Reimert, R.; Kolb, T., Renewable Power-to-Gas: A technological and economic review. *Renewable Energy* **2016**, *85*, 1371-1390.
7. Energy, R., *Wikipedia* **2019**.
8. Fuchs, G.; Lunz, B.; Leuthold, M.; Sauer, D. U., Chapter 7 - Overview of Nonelectrochemical Storage Technologies. In *Electrochemical Energy Storage for Renewable Sources and Grid Balancing*, Moseley, P. T.; Garche, J., Eds. Elsevier: Amsterdam, 2015; pp 89-102.
9. IEA, Renewables 2019. **2019**.
10. Zi, Y.; Wang, Z. L., Nanogenerators: An emerging technology towards nanoenergy. *APL Materials* **2017**, *5* (7), 074103.
11. Hu, F.; Cai, Q.; Liao, F.; Shao, M.; Lee, S.-T., Recent Advancements in Nanogenerators for Energy Harvesting. *Small* **2015**, *11* (42), 5611-5628.
12. Wang, Z. L., Nanogenerators for Self-powered Devices and Systems *SMARTech digital repository* **2011**, *1*.

13. Lu, C.; Chen, J.; Jiang, T.; Gu, G.; Tang, W.; Wang, Z. L., A Stretchable, Flexible Triboelectric Nanogenerator for Self-Powered Real-Time Motion Monitoring. *Advanced Materials Technologies* **2018**, *3* (6), 1800021.
14. Song, P.; Yang, G.; Lang, T.; Yong, K.-T., Nanogenerators for wearable bioelectronics and biodevices. *Journal of Physics D: Applied Physics* **2018**, *52* (2), 023002.
15. Ma, Y.; Zheng, Q.; Liu, Y.; Shi, B.; Xue, X.; Ji, W.; Liu, Z.; Jin, Y.; Zou, Y.; An, Z.; Zhang, W.; Wang, X.; Jiang, W.; Xu, Z.; Wang, Z. L.; Li, Z.; Zhang, H., Self-Powered, One-Stop, and Multifunctional Implantable Triboelectric Active Sensor for Real-Time Biomedical Monitoring. *Nano Letters* **2016**, *16* (10), 6042-6051.
16. Maiti, S.; Karan, S. K.; Kim, J. K.; Khatua, B. B., Nature Driven Bio-Piezoelectric/Triboelectric Nanogenerator as Next-Generation Green Energy Harvester for Smart and Pollution Free Society. *Advanced Energy Materials* **2019**, *9* (9), 1803027.
17. Zhou, M.; Al-Furjan, M. S. H.; Zou, J.; Liu, W., A review on heat and mechanical energy harvesting from human – Principles, prototypes and perspectives. *Renewable and Sustainable Energy Reviews* **2018**, *82*, 3582-3609.
18. Wu, C.; Wang, A. C.; Ding, W.; Guo, H.; Wang, Z. L., Triboelectric Nanogenerator: A Foundation of the Energy for the New Era. *Advanced Energy Materials* **2019**, *9* (1), 1802906.
19. Luo, J.; Wang, Z.; Xu, L.; Wang, A. C.; Han, K.; Jiang, T.; Lai, Q.; Bai, Y.; Tang, W.; Fan, F. R.; Wang, Z. L., Flexible and durable wood-based triboelectric nanogenerators for self-powered sensing in athletic big data analytics. *Nature Communications* **2019**, *10* (1), 5147.
20. Ma, M.; Kang, Z.; Liao, Q.; Zhang, Q.; Gao, F.; Zhao, X.; Zhang, Z.; Zhang, Y., Development, applications, and future directions of triboelectric nanogenerators. *Nano Research* **2018**, *11* (6), 2951-2969.
21. Cheng, T.; Gao, Q.; Wang, Z. L., The Current Development and Future Outlook of Triboelectric Nanogenerators: A Survey of Literature. *Advanced Materials Technologies* **2019**, *4* (3), 1800588.
22. Bai, P.; Zhu, G.; Lin, Z.-H.; Jing, Q.; Chen, J.; Zhang, G.; Ma, J.; Wang, Z. L., Integrated Multilayered Triboelectric Nanogenerator for Harvesting Biomechanical Energy from Human Motions. *ACS Nano* **2013**, *7* (4), 3713-3719.
23. Byun, K.-E.; Lee, M.-H.; Cho, Y.; Nam, S.-G.; Shin, H.-J.; Park, S., Potential role of motion for enhancing maximum output energy of triboelectric nanogenerator. *APL Materials* **2017**, *5* (7), 074107.
24. Wang, Z. L.; Song, J., Piezoelectric Nanogenerators Based on Zinc Oxide Nanowire Arrays. *Science* **2006**, *312* (5771), 242-246.
25. Wang, Z. L., Towards Self-Powered Nanosystems: From Nanogenerators to Nanopiezotronics. *Advanced Functional Materials* **2008**, *18* (22), 3553-3567.
26. Qin, Y.; Wang, X.; Wang, Z. L., Microfibre–nanowire hybrid structure for energy scavenging. *Nature* **2008**, *451* (7180), 809-813.
27. Gao, Y.; Wang, Z. L., Electrostatic Potential in a Bent Piezoelectric Nanowire. The Fundamental Theory of Nanogenerator and Nanopiezotronics. *Nano Letters* **2007**, *7* (8), 2499-2505.
28. Gao, P. X.; Song, J.; Liu, J.; Wang, Z. L., Nanowire Piezoelectric Nanogenerators on Plastic Substrates as Flexible Power Sources for Nanodevices. *Advanced Materials* **2007**, *19* (1), 67-72.

29. Wang, S.; Wang, Z. L.; Yang, Y., A One-Structure-Based Hybridized Nanogenerator for Scavenging Mechanical and Thermal Energies by Triboelectric–Piezoelectric–Pyroelectric Effects. *Advanced Materials* **2016**, *28* (15), 2881-2887.
30. Suo, G.; Yu, Y.; Zhang, Z.; Wang, S.; Zhao, P.; Li, J.; Wang, X., Piezoelectric and Triboelectric Dual Effects in Mechanical-Energy Harvesting Using BaTiO₃/Polydimethylsiloxane Composite Film. *ACS Applied Materials & Interfaces* **2016**, *8* (50), 34335-34341.
31. Yang, Y.; Guo, W.; Pradel, K. C.; Zhu, G.; Zhou, Y.; Zhang, Y.; Hu, Y.; Lin, L.; Wang, Z. L., Pyroelectric Nanogenerators for Harvesting Thermoelectric Energy. *Nano Letters* **2012**, *12* (6), 2833-2838.
32. Zhang, F.; Niu, S.; Guo, W.; Zhu, G.; Liu, Y.; Zhang, X.; Wang, Z. L., Piezo-phototronic Effect Enhanced Visible/UV Photodetector of a Carbon-Fiber/ZnO-CdS Double-Shell Microwire. *ACS Nano* **2013**, *7* (5), 4537-4544.
33. Liu, Y.; Zhang, Y.; Yang, Q.; Niu, S.; Wang, Z. L., Fundamental theories of piezotronics and piezo-phototronics. *Nano Energy* **2015**, *14*, 257-275.
34. Hu, Y.; Zhang, Y.; Xu, C.; Lin, L.; Snyder, R. L.; Wang, Z. L., Self-Powered System with Wireless Data Transmission. *Nano Letters* **2011**, *11* (6), 2572-2577.
35. Fan, F.-R.; Tian, Z.-Q.; Lin Wang, Z., Flexible triboelectric generator. *Nano Energy* **2012**, *1* (2), 328-334.
36. Wang, Z. L., Triboelectric nanogenerators as new energy technology and self-powered sensors – Principles, problems and perspectives. *Faraday Discussions* **2014**, *176* (0), 447-458.
37. Wang, S.; Lin, L.; Wang, Z. L., Nanoscale Triboelectric-Effect-Enabled Energy Conversion for Sustainably Powering Portable Electronics. *Nano Letters* **2012**, *12* (12), 6339-6346.
38. Wang, S.; Lin, L.; Xie, Y.; Jing, Q.; Niu, S.; Wang, Z. L., Sliding-Triboelectric Nanogenerators Based on In-Plane Charge-Separation Mechanism. *Nano Letters* **2013**, *13* (5), 2226-2233.
39. Zhu, G.; Chen, J.; Liu, Y.; Bai, P.; Zhou, Y. S.; Jing, Q.; Pan, C.; Wang, Z. L., Linear-Grating Triboelectric Generator Based on Sliding Electrification. *Nano Letters* **2013**, *13* (5), 2282-2289.
40. Yang, Y.; Zhang, H.; Chen, J.; Jing, Q.; Zhou, Y. S.; Wen, X.; Wang, Z. L., Single-Electrode-Based Sliding Triboelectric Nanogenerator for Self-Powered Displacement Vector Sensor System. *ACS Nano* **2013**, *7* (8), 7342-7351.
41. Wang, S.; Xie, Y.; Niu, S.; Lin, L.; Wang, Z. L., Freestanding Triboelectric-Layer-Based Nanogenerators for Harvesting Energy from a Moving Object or Human Motion in Contact and Non-contact Modes. *Advanced Materials* **2014**, *26* (18), 2818-2824.
42. Wang, Z. L., Triboelectric Nanogenerators as New Energy Technology for Self-Powered Systems and as Active Mechanical and Chemical Sensors. *ACS Nano* **2013**, *7* (11), 9533-9557.
43. Wang, Z. L., On Maxwell's displacement current for energy and sensors: the origin of nanogenerators. *Materials Today* **2017**, *20* (2), 74-82.
44. Wang, X.; Song, J.; Liu, J.; Wang, Z. L., Direct-Current Nanogenerator Driven by Ultrasonic Waves. *Science* **2007**, *316* (5821), 102-105.
45. Xu, S.; Qin, Y.; Xu, C.; Wei, Y.; Yang, R.; Wang, Z. L., Self-powered nanowire devices. *Nature Nanotechnology* **2010**, *5* (5), 366-373.
46. Zhu, G.; Yang, R.; Wang, S.; Wang, Z. L., Flexible High-Output Nanogenerator Based on Lateral ZnO Nanowire Array. *Nano Letters* **2010**, *10* (8), 3151-3155.

47. Wang, Z. L., Nanopiezotronics. *Advanced Materials* **2007**, *19* (6), 889-892.
48. Zhang, W.; Xiong, R.-G., Ferroelectric Metal–Organic Frameworks. *Chemical Reviews* **2012**, *112* (2), 1163-1195.
49. Shi, P.-P.; Tang, Y.-Y.; Li, P.-F.; Liao, W.-Q.; Wang, Z.-X.; Ye, Q.; Xiong, R.-G., Symmetry breaking in molecular ferroelectrics. *Chemical Society Reviews* **2016**, *45* (14), 3811-3827.
50. Bowen, C. R.; Taylor, J.; LeBoulbar, E.; Zabek, D.; Chauhan, A.; Vaish, R., Pyroelectric materials and devices for energy harvesting applications. *Energy & Environmental Science* **2014**, *7* (12), 3836-3856.
51. Fan, F. R.; Tang, W.; Wang, Z. L., Flexible Nanogenerators for Energy Harvesting and Self-Powered Electronics. *Advanced Materials* **2016**, *28* (22), 4283-4305.
52. Özgür, Ü.; Alivov, Y. I.; Liu, C.; Teke, A.; Reshchikov, M. A.; Doğan, S.; Avrutin, V.; Cho, S.-J.; Morkoç, H., A comprehensive review of ZnO materials and devices. *Journal of Applied Physics* **2005**, *98* (4), 041301.
53. Law, J. B. K.; Thong, J. T. L., Lateral ZnO nanowire growth on a planar substrate using a growth barrier. *Nanotechnology* **2007**, *18* (5), 055601.
54. Lu, M.-P.; Song, J.; Lu, M.-Y.; Chen, M.-T.; Gao, Y.; Chen, L.-J.; Wang, Z. L., Piezoelectric Nanogenerator Using p-Type ZnO Nanowire Arrays. *Nano Letters* **2009**, *9* (3), 1223-1227.
55. Wang, Z. L.; Wang, X.; Song, J.; Liu, J.; Gao, Y., Piezoelectric Nanogenerators for Self-Powered Nanodevices. *IEEE Pervasive Computing* **2008**, *7* (1), 49-55.
56. Yang, R.; Qin, Y.; Dai, L.; Wang, Z. L., Power generation with laterally packaged piezoelectric fine wires. *Nature Nanotechnology* **2009**, *4* (1), 34-39.
57. Tao, R.; Parmar, M.; Ardila, G.; Oliveira, P.; Marques, D.; Montès, L.; Mouis, M., Performance of ZnO based piezo-generators under controlled compression. *Semiconductor Science and Technology* **2017**, *32* (6), 064003.
58. Lee, E. J.; Kim, T. Y.; Kim, S.-W.; Jeong, S.; Choi, Y.; Lee, S. Y., High-performance piezoelectric nanogenerators based on chemically-reinforced composites. *Energy & Environmental Science* **2018**, *11* (6), 1425-1430.
59. Surmenev, R. A.; Orlova, T.; Chernozem, R. V.; Ivanova, A. A.; Bartasyte, A.; Mathur, S.; Surmeneva, M. A., Hybrid lead-free polymer-based nanocomposites with improved piezoelectric response for biomedical energy-harvesting applications: A review. *Nano Energy* **2019**, *62*, 475-506.
60. Whiter, R. A.; Narayan, V.; Kar-Narayan, S., A Scalable Nanogenerator Based on Self-Poled Piezoelectric Polymer Nanowires with High Energy Conversion Efficiency. *Advanced Energy Materials* **2014**, *4* (18), 1400519.
61. Lee, K. Y.; Kim, D.; Lee, J.-H.; Kim, T. Y.; Gupta, M. K.; Kim, S.-W., Unidirectional High-Power Generation via Stress-Induced Dipole Alignment from ZnSnO₃ Nanocubes/Polymer Hybrid Piezoelectric Nanogenerator. *Advanced Functional Materials* **2014**, *24* (1), 37-43.
62. Shin, S.-H.; Kim, Y.-H.; Lee, M. H.; Jung, J.-Y.; Nah, J., Hemispherically Aggregated BaTiO₃ Nanoparticle Composite Thin Film for High-Performance Flexible Piezoelectric Nanogenerator. *ACS Nano* **2014**, *8* (3), 2766-2773.
63. Mao, Y.; Zhao, P.; McConohy, G.; Yang, H.; Tong, Y.; Wang, X., Sponge-Like Piezoelectric Polymer Films for Scalable and Integratable Nanogenerators and Self-Powered Electronic Systems. *Advanced Energy Materials* **2014**, *4* (7), 1301624.

64. Ding, R.; Liu, H.; Zhang, X.; Xiao, J.; Kishor, R.; Sun, H.; Zhu, B.; Chen, G.; Gao, F.; Feng, X.; Chen, J.; Chen, X.; Sun, X.; Zheng, Y., Flexible Piezoelectric Nanocomposite Generators Based on Formamidinium Lead Halide Perovskite Nanoparticles. *Advanced Functional Materials* **2016**, *26* (42), 7708-7716.
65. Dahiya, A. S.; Morini, F.; Boubenia, S.; Nadaud, K.; Alquier, D.; Poulin-Vittrant, G., Organic/Inorganic Hybrid Stretchable Piezoelectric Nanogenerators for Self-Powered Wearable Electronics. *Advanced Materials Technologies* **2018**, *3* (2), 1700249.
66. Saravanakumar, B.; Soyoon, S.; Kim, S.-J., Self-Powered pH Sensor Based on a Flexible Organic–Inorganic Hybrid Composite Nanogenerator. *ACS Applied Materials & Interfaces* **2014**, *6* (16), 13716-13723.
67. Zou, H.; Zhang, Y.; Guo, L.; Wang, P.; He, X.; Dai, G.; Zheng, H.; Chen, C.; Wang, A. C.; Xu, C.; Wang, Z. L., Quantifying the triboelectric series. *Nature Communications* **2019**, *10* (1), 1427.
68. Wang, A. C.; Wu, C.; Pisignano, D.; Wang, Z. L.; Persano, L., Polymer nanogenerators: Opportunities and challenges for large-scale applications. *Journal of Applied Polymer Science* **2018**, *135* (24), 45674.
69. Niu, S.; Wang, Z. L., Theoretical systems of triboelectric nanogenerators. *Nano Energy* **2015**, *14*, 161-192.
70. Cao, X.; Jie, Y.; Wang, N.; Wang, Z. L., Triboelectric Nanogenerators Driven Self-Powered Electrochemical Processes for Energy and Environmental Science. *Advanced Energy Materials* **2016**, *6* (23), 1600665.
71. Zhu, G.; Pan, C.; Guo, W.; Chen, C.-Y.; Zhou, Y.; Yu, R.; Wang, Z. L., Triboelectric-Generator-Driven Pulse Electrodeposition for Micropatterning. *Nano Letters* **2012**, *12* (9), 4960-4965.
72. Wang, Z. L.; Wu, W., Nanotechnology-Enabled Energy Harvesting for Self-Powered Micro-/Nanosystems. *Angewandte Chemie International Edition* **2012**, *51* (47), 11700-11721.
73. Niu, S.; Wang, X.; Yi, F.; Zhou, Y. S.; Wang, Z. L., A universal self-charging system driven by random biomechanical energy for sustainable operation of mobile electronics. *Nature Communications* **2015**, *6* (1), 8975.
74. Chen, J.; Yang, J.; Li, Z.; Fan, X.; Zi, Y.; Jing, Q.; Guo, H.; Wen, Z.; Pradel, K. C.; Niu, S.; Wang, Z. L., Networks of Triboelectric Nanogenerators for Harvesting Water Wave Energy: A Potential Approach toward Blue Energy. *ACS Nano* **2015**, *9* (3), 3324-3331.
75. Wang, Z. L., Nanogenerators, self-powered systems, blue energy, piezotronics and piezophotonics – A recall on the original thoughts for coining these fields. *Nano Energy* **2018**, *54*, 477-483.
76. Ding, W.; Wang, A. C.; Wu, C.; Guo, H.; Wang, Z. L., Human–Machine Interfacing Enabled by Triboelectric Nanogenerators and Tribotronics. *Advanced Materials Technologies* **2019**, *4* (1), 1800487.
77. Zhang, B.; Tang, Y.; Dai, R.; Wang, H.; Sun, X.; Qin, C.; Pan, Z.; Liang, E.; Mao, Y., Breath-based human–machine interaction system using triboelectric nanogenerator. *Nano Energy* **2019**, *64*, 103953.

Chapter 2

High power mechanical energy harvester based on exfoliated black phosphorous–polymer composite and its multiple applications

Abstract

Black Phosphorous (BP) and its 2D analogue Phosphorene are endowed with several striking properties due to their unique puckered structure. One attribute that can potentially attract multiple applications of interest, and yet not fully addressed, is their mechano-electric response. Herein, we demonstrate the utility of a uniformly dense dispersion of few-layer BP (FLBP) nanosheets in PDMS (Polydimethylsiloxane) matrix, with a high 2D-dielectric interface density, exhibiting a remarkably strong mechanical energy harvesting effect. A highest peak-to-peak voltage output of about 350 Volts is achieved with a maximum current density of 12.8 mA/m² under an applied impact force of 40 Newtons (N), at a frequency range of 20-25 Hz. This corresponds to a volume power density of 2 kW/m³ with active material (BP) contribution of 0.35 W/g. Notably, the 2D BP nanosheets themselves are found to exhibit a fairly high piezoelectric coefficient of ~20 pm/V as revealed by the Piezoresponse Force Microscopy (PFM). First-principles DFT calculations suggest the existence of strain-induced polarization in the BP layers via deformation-induced redistribution of intra-layer electron charge density. Based on the experimental and theoretical findings, we propose a synergistic multi-polarization mechanism that contributes to the strength of the observed energy harvesting effect. We also present three interesting practical modes of energy harvesting by subjecting them to the rapid flow of water, bicycle wheel motion and tapping induced LED lighting.

The following paper has been published based on the work documented in this chapter.

Singh, S. K.; Muduli, S.; Chakras, D.; Pandey, R.; Babar, R.; Singh, A.; Kabra, D.; Kabir, M.; Boomishankar, R.; Ogale, S., High power mechanical energy harvester based on exfoliated black phosphorous–polymer composite and its multiple applications. *Sustainable Energy & Fuels* 2019, 3 (8), 1943-1950. This chapter is reproduced from our above-mentioned article already published in *Sustainable Energy & Fuels* after acknowledging the Royal Society of Chemistry.

2.1 Introduction

Ever since the discovery of graphene, 2D materials and their few-layer forms have acquired a unique place in the emergent science of materials owing to their very peculiar and tunable physical properties.¹⁻⁴ These materials have also been attracting immense scientific attention lately for their applicability in novel device architectures.^{5,6} Amongst the 2D materials of current interest, Black Phosphorous (BP) and its monolayer form phosphorene stand out for their unique puckered layer structure, specific nature of bonding, existence of layer-number-dependent bandgap that covers visible and IR regimes, and interesting anisotropy features of their physical properties.⁷ An interesting application domain involving novel device architectures based on new functional materials that have witnessed immense growth during the past decade is mechanical energy harvesting. It involves the mechanical movement, flexing, vibration, friction, or impact via innovative nanogenerator (NG) and triboelectric-nanogenerator (TENG) device concepts. This topic evolved quite rapidly with the numerous pioneering contributions from the groups of Z. L. Wang¹³⁻⁸ and several others¹⁴⁻²² by using various functional materials such as ZnO, MoS₂, BaTiO₃ etc. While impressive, robust and application-worthy performance has been reported for a number of piezoelectric and ferroelectric materials in different forms including their nanoscale architectures, the work on nanogenerators using the 2D families of materials and their few-layer configurations is beginning to evolve only recently.^{8, 26-23}

In 2011 Michel and Verberck showed theoretically that the 3D hexagonal boron nitride (h-BN) and its multilayers with odd layer numbers are piezoelectric, while the even number of layers are silent for piezoelectric effects.²⁷ In another theoretical work, Reed and co-workers showed that strong piezoelectricity should occur in many 2D monolayer transition metal dichalcogenides (TMDCs), unlike their bulk counterparts.²⁴ Z. L. Wang and co-workers provided the first experimental evidence for the existence of piezoelectric properties in 2D MoS₂ flakes with only odd layer numbers.⁸ Reed and co-workers²⁸ and Shin and co-workers²⁹ showed that piezoelectricity can be induced in non-piezoelectric graphene or h-BN sheets through the selective/controlled adsorption of surface atoms. Kim and co-workers reported the occurrence of piezoelectric effects in the ALD grown Al₂O₃ on graphene consisting of an h-BN buffer layer,²⁶ and in bilayer WSe₂ system with turbostratic stacking.²³ Black Phosphorous (and its 2D analogue Phosphorene) with its puckered structure can be envisioned to offer a unique response to the

application of static or dynamic mechanical force or impact.^{7, 30, 31} We expected that the combination of its electronic states to the puckered configuration would give rise to strong coupling between the mechanical distortions and polarization effects leading to strong piezo and/or flexoelectric effects. Herein, we show that a solid-state nanogenerator prepared with black phosphorus (BP) nanosheets uniformly and densely dispersed in PDMS (Polydimethylsiloxane) exhibits a remarkably high peak to peak voltage output of the order of 350 Volts (Maximum current density of 12.8 mA/m² at 20MΩ Resistance) under an applied impact force of 40 Newtons (N) at a frequency of 25 Hertz (Hz). The power output generated from this device data has been found to be very high at 1400 mW/m². This corresponds to a volume power density of 2 kW/m³ with active material (BP) contribution of 0.35 W/g. The 2D black phosphorus nanosheets themselves are found to exhibit a fairly high piezoelectric coefficient of ~20 pm/V. DFT calculations suggest the existence of strain induced polarization via deformation induced redistribution of intra-layer electron charge density. We invoke a synergistic multi-mechanism effect to explain the high power output which is also supported by our experiments on folding mode operation of the same device. We also present three interesting applications of this high powering capability device. As discussed later, there have been a few previous reports involving the use of phosphorene/black phosphorous in related context, although mostly for specific low power applications, in contrast to our device design which is specifically targeted for higher power delivery operation.³²⁻³⁴

2.2 Experimental Methods:

2.2.1 Synthesis of Black Phosphorus (BP) nanosheets:

Black Phosphorus (BP) nanosheets exfoliation: BP crystals (200 mg) were treated well in stiff powder with mortar and pestle inside the glove box. The resultant powder was dissolved in 100 ml of N-Methyl-2-pyrrolidone (NMP) immediately. With the help of Probe sonicator (Vibra Cell, VCX-500W, Sonics Inc, USA), the mixture was sonicated for 6 hrs with 40% amplitude for cycle run (5s and 5s off) within temperature range 4-8 °C. For removing the un-exfoliated BP crystals, sonicated BP/NMP dispersion was relaxed for few hours, and by gravity, un-exfoliated BP crystals were allowed to settle down. The supernatant was subsequently transferred into a

Centrifuge apparatus. At a speed of 1000 rpm for 3 hrs, centrifugation removed the remaining exfoliated BP crystals. BP/NMP dispersion was collected again from the top 60% of the supernatant from centrifuge tubes. The last supernatant was centrifuged at a speed of 6000 rpm for 60-80 min, and again 80% supernatant was easily pipetted out to remove junk BP. The sediment was re-dispersed in NMP solution for the further piezoelectricity application part.

2.2.2 Fabrication of the flexible piezoelectric composite NG and testing:

The initial PENG device from as made BP nanosheets was fabricated by directly drop-casting of BP/NMP dispersion on Au/Cr coated Polyethylene Terephthalate (PET) in the glove box and heated at 80°C for 5 hrs to dry up the BP film. After drying the BP film, another set of Au/Cr coated PET was applied to the BP film and device is sealed through Araldite.

For the fabrication of Polydimethylsiloxane (PDMS) - BP nanosheets based piezoelectric NG, the exfoliated black phosphorus nanosheets were mixed with 3 ml of PDMS in different weight ratios of 0.1%, 0.15%, 0.2% and 0.3%. The resulted composite solution was drop cast onto the Au/Cr coated PET substrate and cured at 90° C temperature. After 3 hours, another Au/Cr coated PET substrate as a top electrode was assimilated to the cured composite layer. In result, BP-PDMS composite layer was sandwiched between Au/Cr coated PET. After that, we sealed device with Kapton tape such that there should not be any friction between gold and the BP-PDMS surfaces. The dimensions of flexible piezoelectric nanogenerator were $2 \times 2 \text{ cm}^2$. For the force source, we assembled a 50 g weight (area 5 cm^2) to the edge of sewing handle to get the continuous impact. The impact force from the sewing machine was used to obtain 40 to 45 N force as measured with the help of a PASPORT force sensor at a frequency of 25 Hz. The voltage generated by BP device was further used for charging a $2.2\mu\text{F}$ capacitor through a bridge rectifier circuit. The stored charge was then used to light up the LEDs by using the same bridge rectifier. Change in capacitance of devices is measured by Keithley DMM7510 7.5 multimeter. All Output voltage and current measurements were recorded on Tektronix Oscilloscope MSO 2024 and Keithley DMM7510 7.5 multimeter.

2.3 Characterization techniques:

2.3.1 Field emission scanning electron microscopy (FE-SEM): Zeiss Ultra Plus FESEM at 5-10 kV was used for SEM imaging. Only black phosphorus and BP-PDMS film were prepared by drop-casting them on a glass substrate.

2.3.2 Transmission electron microscopy (TEM): TEM imaging was performed by using JEM2200FS TEM microscope at 30-200 kV.

2.3.3 Atomic Force Microscopy: Agilent Technologies 5500 AFM instrument was used to observe the thickness of single BP nanosheet. BP nanosheet sample was prepared by drop-casting BP/NMP solution on a glass substrate.

2.3.4 X-ray diffraction (XRD): All XRD data were collected on Bruker D8 Advance diffractometer using Cu K α radiation ($\lambda = 1.5406 \text{ \AA}$).

2.4 Result and Discussion

Figure 1 presents the results of the basic characterization of the exfoliated BP nanosheets. The inset of Figure 1(b) shows high-resolution transmission electron microscopy (HRTEM) image of the BP nanosheets reflecting the (021) lattice parameter of $\sim 0.3 \text{ nm}$. The AFM image and thickness profiles of a few exfoliated flakes shown in the Figures 1(c) and 1(d), respectively, reveal the typical thickness of the nanosheets in the order of 20-30 nm. The FE-SEM images of Figure 2 show that the BP material used for inclusion in the PDMS matrix is in the form of nanosheets with a lateral size of the order of a few microns. Figures 1(e) and 1(f) reveal the XRD and Raman data, respectively, of the PDMS-BP nanosheets composite. Put together; both these measurements showed the presence of BP nanosheets embedded at the PDMS matrix. The X-ray diffraction (XRD) data shown in Figure 3 (a) depict the signature peaks of BP nanosheets corresponding to the orthorhombic phase of BP.³¹ The Raman spectrum of the BP nanosheets (Figure 3 (b)) shows three prominent peaks that can be attributed to the out-of-plane phonon mode (A^1_g) at 357.5 cm^{-1} and two in-plane modes, (B_{2g}) and (A^2_g) at 432.5 and 458.7 cm^{-1} , respectively.³⁵ Interestingly, as shown in Figure 4, all the Raman modes in the case of the composite are shifted to higher wavenumbers (hardening of modes) with reference to the BP nanosheets case signifying that the embedded BP nanosheets are under strain, which may have implications for possible piezoelectricity.

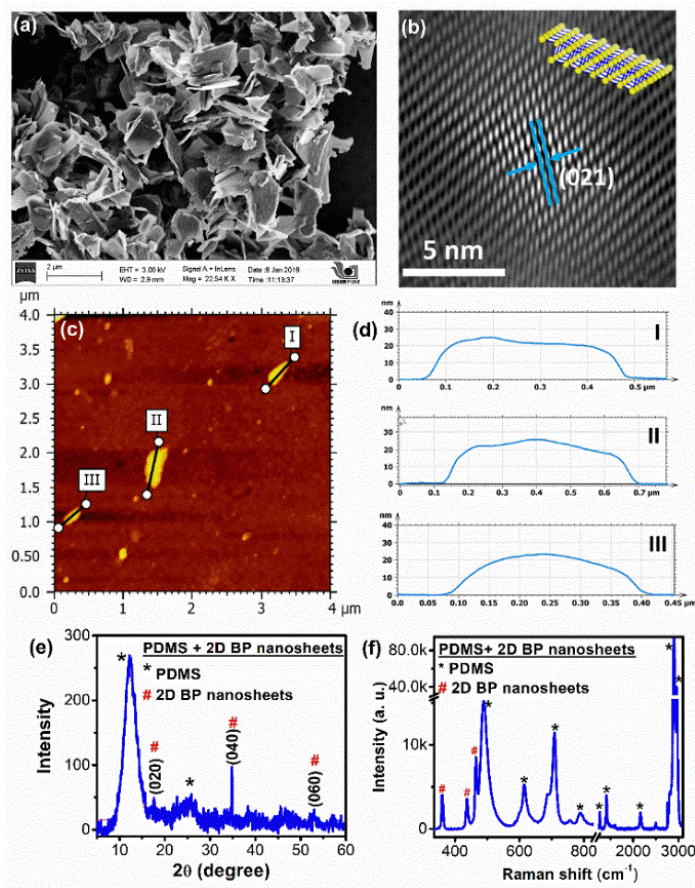


Figure 1 Characterization of BP nanosheet and PDMS-BP nanosheets composite. (a) SEM image of the BP nanosheets (scale bar, 2 μm). (b) HR-TEM image of BP nanosheets (scale bar, 2 nm), showing its zig-zag puckered layered structure along the (021) lattice orientation with 0.3 nm spacing between layers. (c) AFM image of BP nanosheets flexes (I, II, III) (d) BP nanosheets thickness (nm) profiles of I, II, III, which are in the range of 20 nm. (e) Powder XRD of PDMS-BP nanosheets composite reveals the presence of both BP nanosheets and PDMS, and (f) Raman spectrum of PDMS-BP nanosheet composite film showing the presence of characteristic signature peaks of A^1_g , B_{2g} and A^2_g phonon vibrational modes of BP nanosheets.

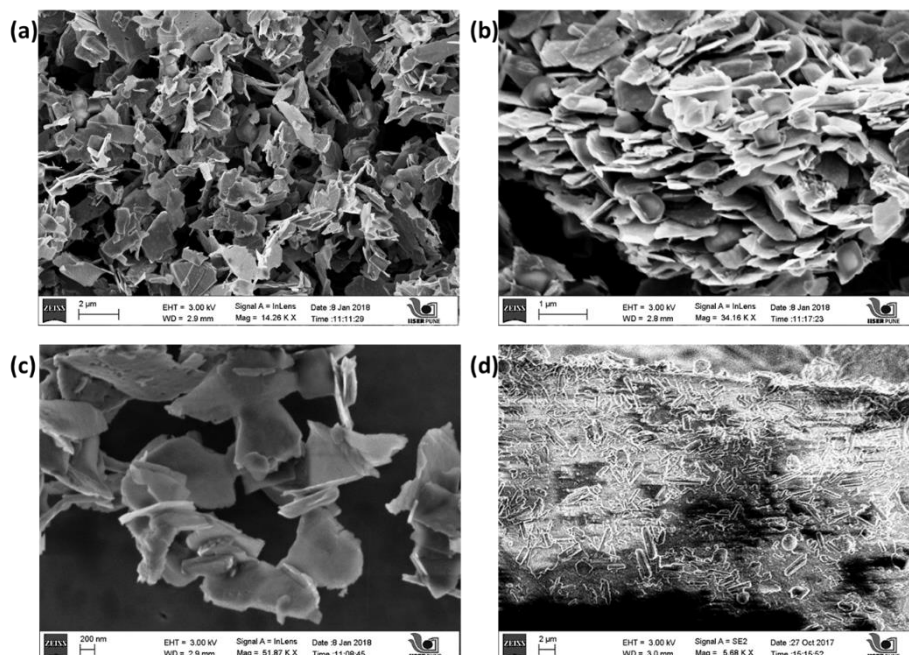


Figure 2 SEM images of BP nanosheets (a), (b) and (c) show uniform lateral size of BP nanosheets synthesized by the Probe sonication method and (d) Cross-sectional SEM image of PDMS-BP nanosheet composite film which shows homogeneous encapsulation of BP nanosheets in PDMS matrix.

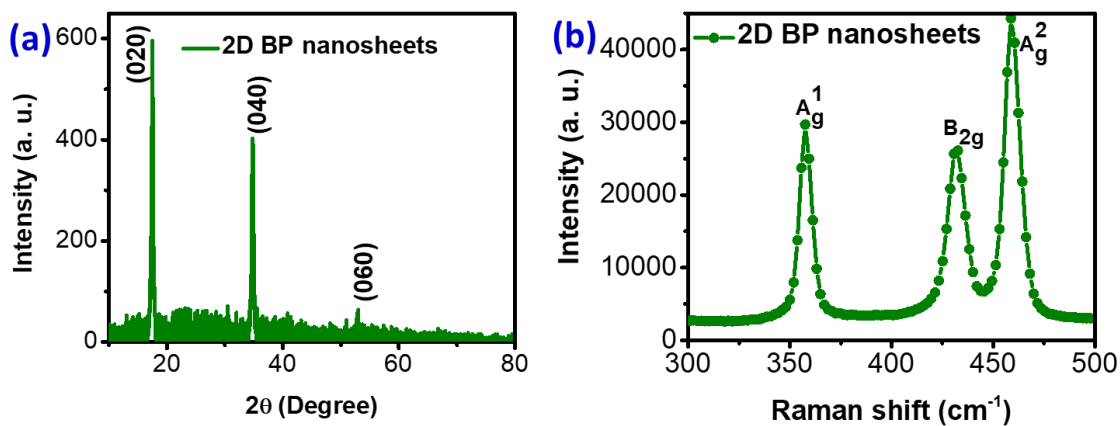


Figure 3 Basic characterization of BP nanosheets: (a) Powder XRD of BP nanosheets; the observed peaks correspond to Orthorhombic phase of BP. (b) Raman spectrum showing the expected signature peaks of BP.

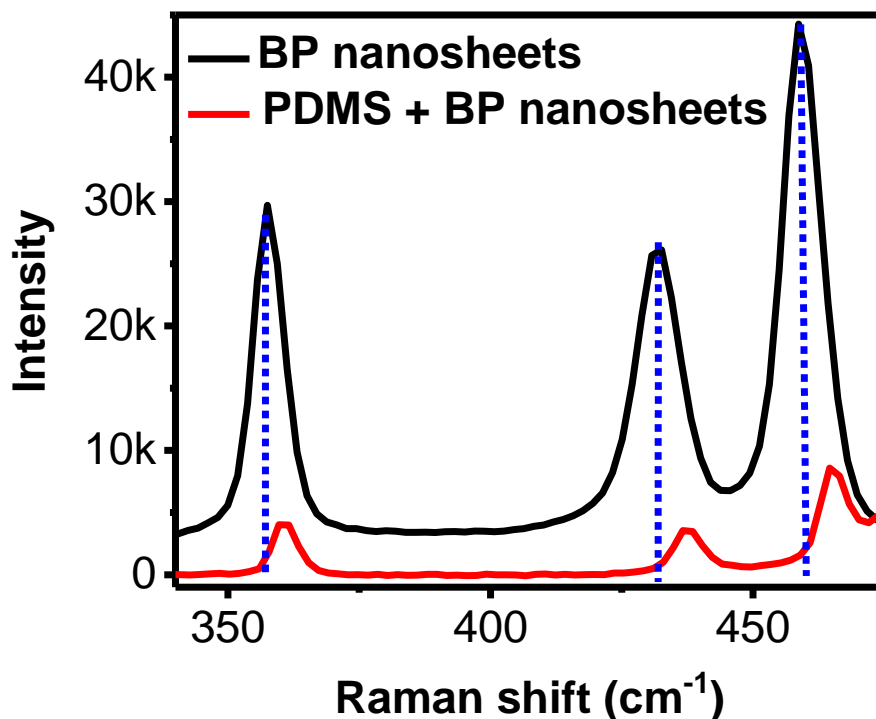


Figure 4 Comparison of the Raman spectra of BP nanosheets and PDMS-BP nanosheets composite showing that all the Raman modes in the case of the composite are shifted to higher wavenumbers with reference to the BP nanosheets.

2.5 Nanogenerator device architecture and performance

A home built periodic vertical impact force setup, and an oscilloscope has been used for the device measurements (Figure 5). To demonstrate the nanogenerator performance of the PDMS-BP nanosheets composite, we fabricated the device, as shown in Figure 6(a). Here, the PDMS-BP composite film of dimensions $2 \times 2 \text{ cm}^2$ and $700 \mu\text{m}$ thickness was sandwiched between Au/Cr (Au layer thickness is 50 nm, and Cr layer thickness is 10 nm) coated PET substrate. The Au/Cr coated PET was compactly pressed on both sides leaving no room for any air gap, and under that condition, the device was wrapped with a highly adhesive Kapton tape to avoid any subsequent slippage of the interfaces. Two copper metal strips were used as metal contacts for the device. The total thickness of the Black phosphorus/PDMS device is 1.45 mm. Devices with different concentrations (wt.%) of BP nanosheets were explored for the nanogenerator performance (Table 1).

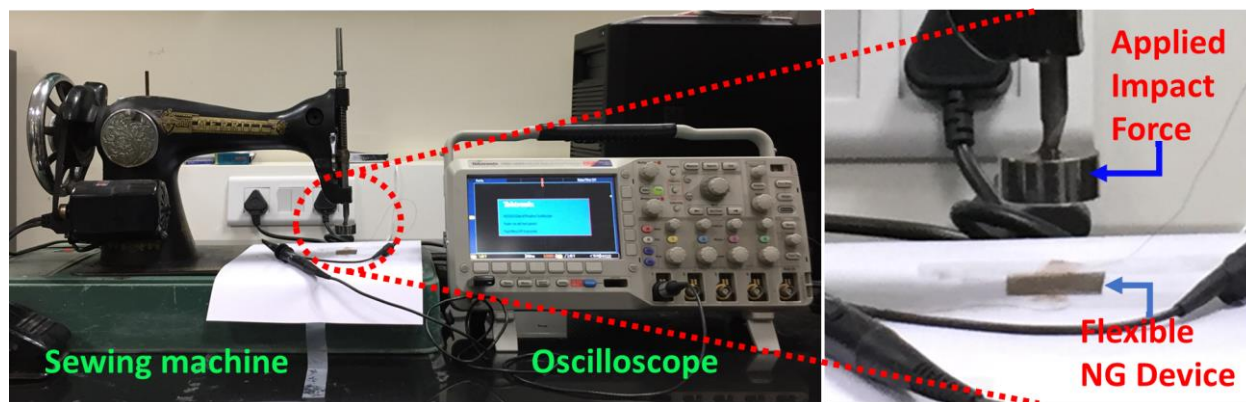


Figure 5 *Impact Force set-up: Sewing Machine Set up to get constant impact force of 40N and Oscilloscope to measure output performance. Inset shows the local modifications done on the sewing machine for obtaining a constant impact.*

In order to evaluate the mechanical generator performance, the devices were subjected to an impact force of 40 N at variable frequencies ranging from 10 Hz to 25 Hz. Figure 6(b) shows the open-circuit voltage obtained for the NG devices with varying concentration of BP at a constant frequency of 25 Hz. The output voltage of the NGs was seen to increase with the BP concentration, approaching saturation around 0.2 wt.% of BP and then declining at higher BP concentrations. Since the FLBP sheets are low dimensional systems, at enhanced concentrations these will start touching each other, causing shorting across the active layer (percolation thresholds are low). Thus, above a certain threshold value of concentration, such effects will start dominating, and rather sudden changes could be encountered as discussed in some previous publications³⁶⁻³⁹, wherein similar performance peaking effects were observed. Thus, in our view, the peaking would be a generic effect in such nanocomposites, although the thresholds would differ depending on the constitution of the nanomaterials.

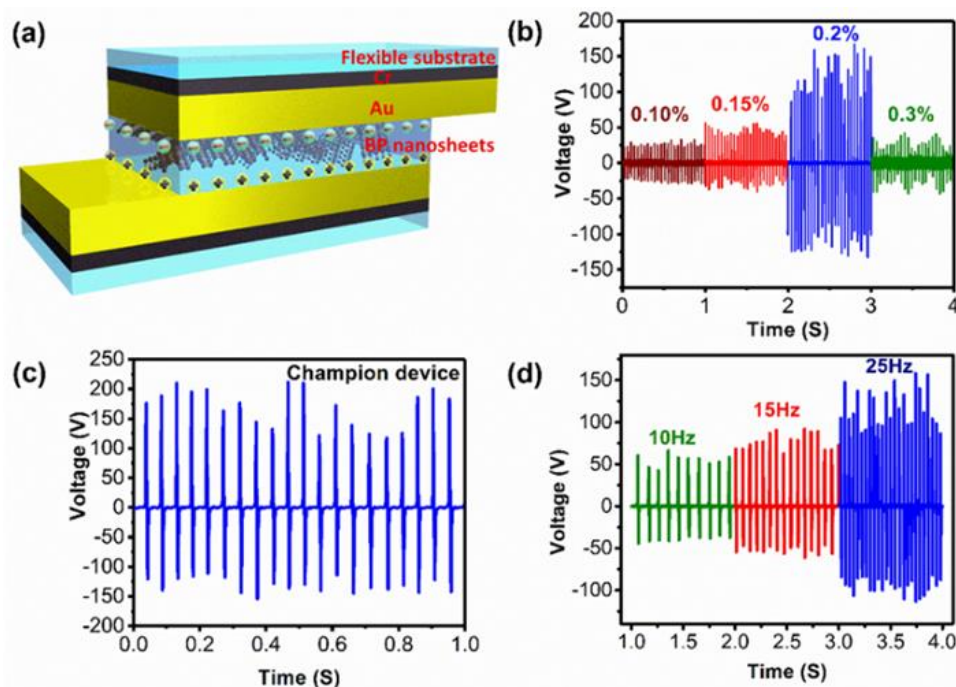


Figure 6 Nanogenerator Schematic and Output performance (a) Schematic of fabricated NG device (b) Optimization of Different concentrations (wt%) of BP in PDMS performed for maximum NG's output voltage (c) Output voltage of Champion device and (f) effect of variable frequencies on the output voltages

Table 1 Nanogenerator performance for devices with different concentration (wt.%) of BP nanosheets

Concentration (weight %) BP in PDMS	Peak to Peak Output Voltage (V)	Output Voltage across 20M Ω	Current density (mA/m 2)	Power Density (mW/m 2)
	A	B	C	D = B x C
0.10	61	19.5	6.1	119
0.20	350	109.3	12.8	1399
0.30	85	25.9	9.4	243

Our champion device showed a peak to peak voltage of 350 V from 0.2 wt.% device as can be seen in figure 6(c). Figure 6(d) reveals the frequency-dependent data of the same device, which shows an increasing trend in the voltage values with frequency. Also, the current density and the output power density values of 12.8 mA/m 2 and 1400 mW/m 2 , respectively, were found to be very high as well at an optimized impedance of 20 M Ω (Figure 7(a) and (b)) There have been four previous interesting and innovative reports involving the use of phosphorene for mechanical

energy harvesting, although most of them are in low energy delivering device architectures intended for certain specific application goals. Cary Pint and co-workers demonstrated an ultralow frequency electrochemical-mechanical strain energy harvester using 2D BP nanosheets, which yielded 0.42 mW/m^2 ($0.2 \text{ } \mu\text{J/cm}^2$) in bending mode and 0.09 mW/m^2 ($0.8 \text{ } \mu\text{J/cm}^2$) in pressing mode. Pooi See Lee and coworkers³² developed and tested cellulose nanofibril–phosphorene hybrid based flexible and transparent paper for triboelectric nanogenerator function and realized an open circuit voltage of 5.2 V and current density of $1.8 \text{ } \mu\text{A/cm}^2$. In a subsequent study, Z. L. Wang and coworkers³³ developed tribotronic dual-gate logic devices based on MoS₂ and BP and showed their operation at low powering as low as even 1 nW. However, our device design involves a few-layer BP (FLBP) polymer composite and is specifically aimed at high powering capabilities.

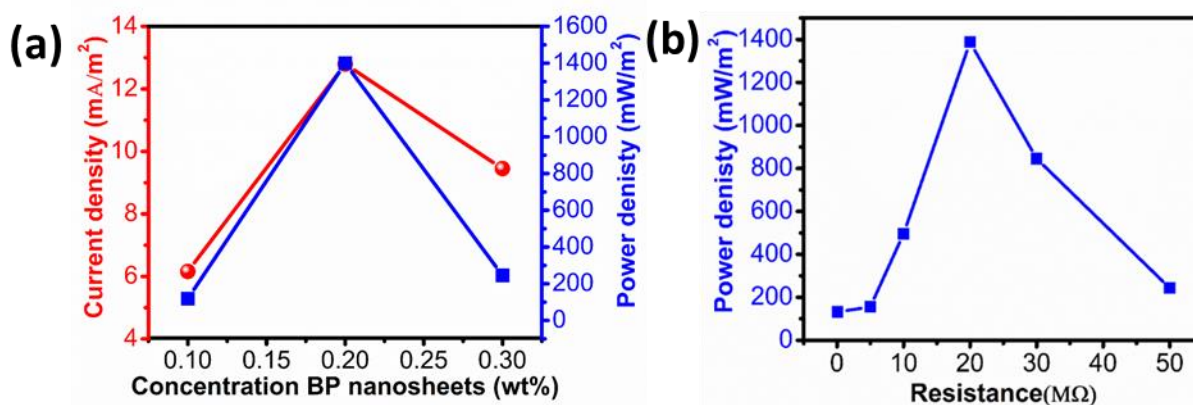


Figure 7 (a) Maximum current density and power density of flexible NG device with different concentrations (wt%) (b) Power density with variable resistance from PDMS-BP NG.

To check the cyclic stability, one of the 0.2 wt.% devices were subjected to a continuous impact of 40 N for 20 minutes at a frequency of 25 Hz. The peak to peak output voltage of about 200 V was consistently observed for over 24,000 cycles of impact application, confirming the excellent reliability and robustness of PDMS-BP nanosheets device (Figure 8(a)). The mechanical flexibility and robustness of our device can be ascribed to its simple design of top-bottom architecture as compared to other complex architectures. It is important to note that a PDMS based device without the inclusion of BP only yielded a peak-to-peak output of only about 5V (Figure 8(b)) implying that BP inclusion is the one which mainly renders the strong signal due to its internal multi-interface configuration.

The polarity reversal test was also performed to confirm that the piezoelectric response emanates only from the PDMS-BP nanosheets composite, as shown in Figure 9(a) and (b). Finally, in Figure 9, we show the change in capacitance as a function of time for samples with different concentrations of Black Phosphorus in PDMS. Again, we observed the highest change in capacitance in the 0.2 wt.% case and exhibits a similar trend in output voltages as those observed for the wt.% dependent measurements. We found that dC/dt in the case of 0.3 weight percentage dropped from the maximum dC/dt (0.2% case).

$$I = dQ/dt = C dV/dt + V dC/dt$$

Where I is short circuit current and Q is the stored charges in the capacitor. The second term is imperative for the triboelectric effect because it depends on the gap between two dielectric materials or triboelectric layers. Figure 10 shows the change in capacitance w.r.t time studied for different concentrations of Black Phosphorus in PDMS. We observed the highest change in capacitance in 0.2% (wt%) concentration case. It results in the same trend with a change in output voltage for different concentrations.

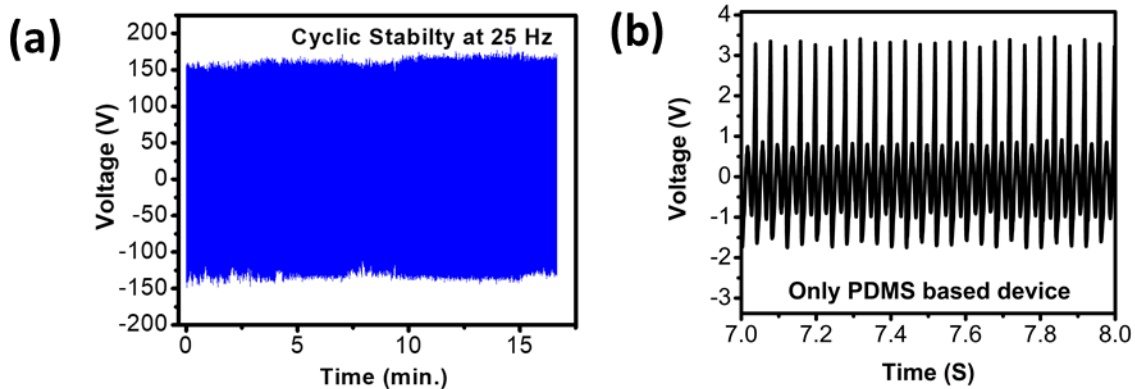


Figure 8 Cyclic stability of Nanogenerator: (a) The peak to the peak output voltage of about 200 V was consistently observed for over 30,000 cycles of impact application, confirming the excellent reliability and robustness of PDMS-BP nanosheets device. (b) Peak to peak output voltage is around 5 V from only PDMS based NG device (i.e. without BP) which is fabricated in the same configuration as composite

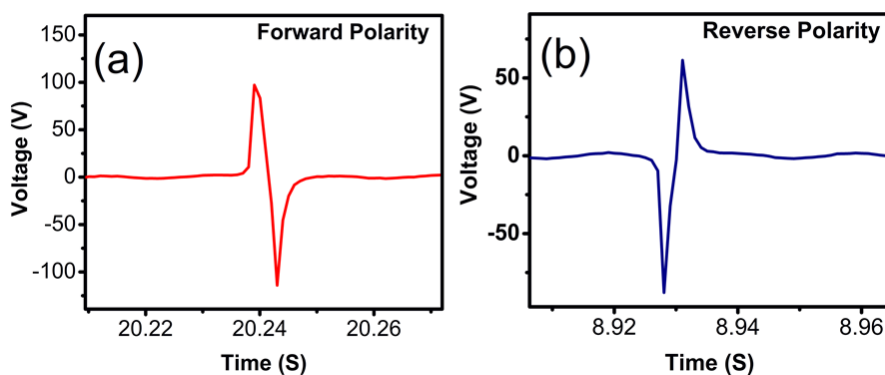


Figure 9 (a) Polarity switchability Test by Forward connections, (b) Voltage signal is reversed by the reverse connection, which shows polarization switchable behaviour of BP-PDMS Nanogenerator.

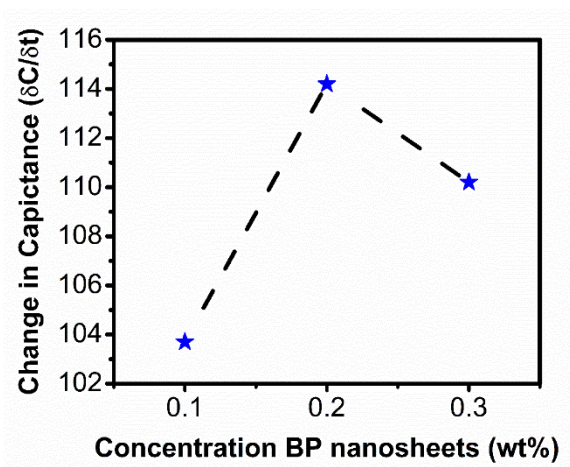


Figure 10 Measurement of change in capacitance time gradient with the different weight ratio of Black Phosphorus in PDMS .

We also tested the performance of the same device in the bending (flex) mode operation, as shown in Figure 11 (a). The corresponding peak to peak voltage and current density values of 65 V and 68.75 mA/cm², respectively, are found to be lower than those observed in vertical pressing mode measurements (Figure 11 (b)). The distinct technical difference between the vertical mode impact and the folding operation is that in the former the distance between embedded phosphorene sheets varies with impact and release, while in the latter the sheets undergo flexing but the inter-sheet separation is not significantly modified. This result has a bearing on the fact

that the observed effects have a close connection with the density of interfaces and the corresponding polarization interactions.

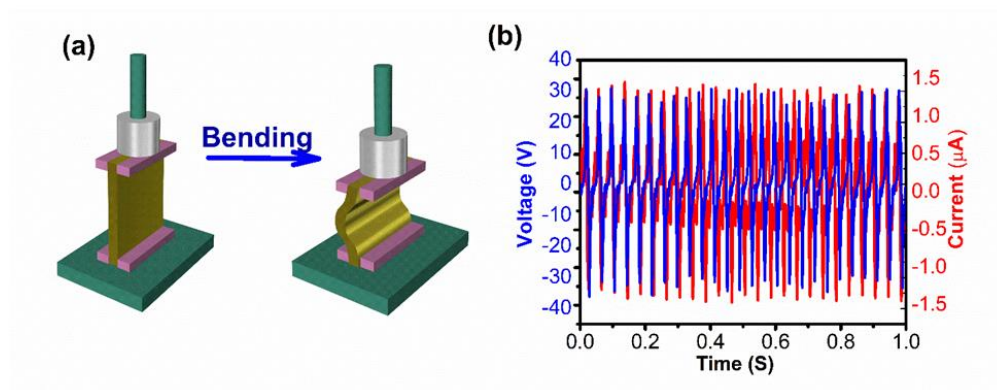


Figure 11 (a) Schematic diagram of the relax stage to bending stage of vertical PDMS-BP nanosheets device, (b) open-circuit voltage and short circuit current from the relax-bending mechanism.

To understand the piezo- and triboelectric contributions to the output performance of the devices, we performed two additional measurements. First, we measured the voltages and currents for only the BP nanosheets, and in the second we measured the nanogenerator performance for the PDMS-BP nanosheets with only single electrode applied to the film.⁴⁰ The BP-only device reflects a much weaker performance, highlighting the key significance of the embedded architecture (Figure 12). The device with a single electrode shows a peak-to-peak voltage of only about 40 V (Figure 13(a)). This signifies that the major contribution to our device performance is by synergistic internal mechanisms that operate in unison as discussed later.

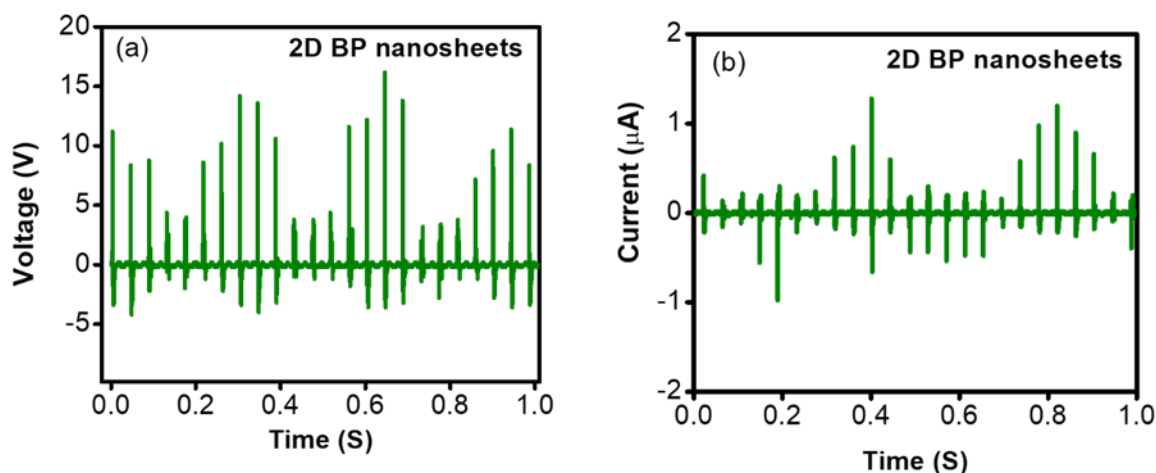


Figure 12 Performance of only BP nanosheets based NG: a) Open circuit voltage, b) Current using $10\text{ M}\Omega$ load resistance.

Finally, we tested the time-stability of our device as well, especially in view of the fact that BP nanosheets are suggested to be intrinsically a rather unstable material at ambient conditions. However, since in our case, it is embedded in the highly stable PDMS matrix, we expected that the device would have high environmental stability. This was indeed found to be the case, as shown by the result depicted in Figure 13(b), wherein stability over at least a period of three months is clearly reflected.

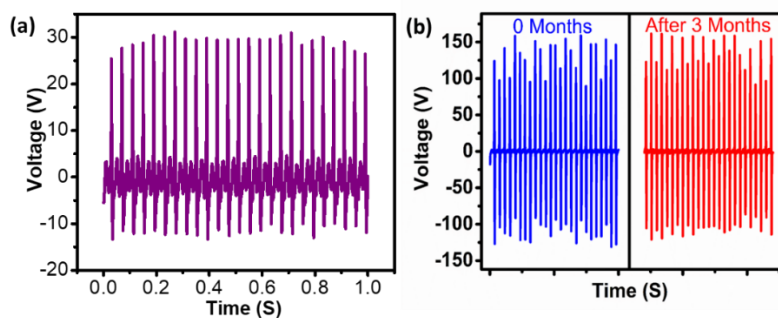


Figure 13 (a) Single electrode measurement to counter the argument about the possible triboelectric contribution by friction between electrode and PDMS-BP nanosheets composite film. (b) To check the stability of PDMS-BP nanosheets composite based NGs, we tested the output voltage of the same device after 3 months; which shows that NG device is completely friendly with the environment, thanks to the PDMS protection of BP.

2.6 Piezoresponse force microscopy (PFM) studies

We performed piezoresponse force microscopy (PFM) studies on the BP nanosheets themselves, which are found to render the observed strong mechanical energy harvesting effect in the polymer embedded composite. It is known that the analysis of PFM data is not entirely straightforward, and the appearance of the so-called butterfly loops could be deceptive due to space charge effects.⁴¹ Nonetheless, it does provide a useful window for analysis, especially of the inverse piezoelectric effect. Figure 14 (a) presents the topographic image of the BP nanosheets and Figures 14(b) and 14(c) show the amplitude loop and image at a bias voltage of ± 8 V, respectively. The 180° difference in the phase angle hysteresis loop and its phase image for the BP nanosheets shown in Figures 14(d) and 14(e), respectively, indicate that the polarization can indeed be switched in BP nanosheets by an applied external electric field. The piezoresponse loop is presented in Figure 14(f). The piezoresponse of the film was detected as the first-harmonic component of the deflection of the tip, $d = d_0 + A \cos(\omega t + \phi)$, where ϕ is the phase of the piezoelectric signal, d_0 is an initial deflection, A the amplitude, t is the time, and ω is the frequency. The photodetector signal amplitude was demodulated with a lock-in amplifier, and the values of the inverse piezoelectric coefficient were obtained. The absolute value of the inverse piezoelectric coefficient, thus estimated, is about 20 pm/V.

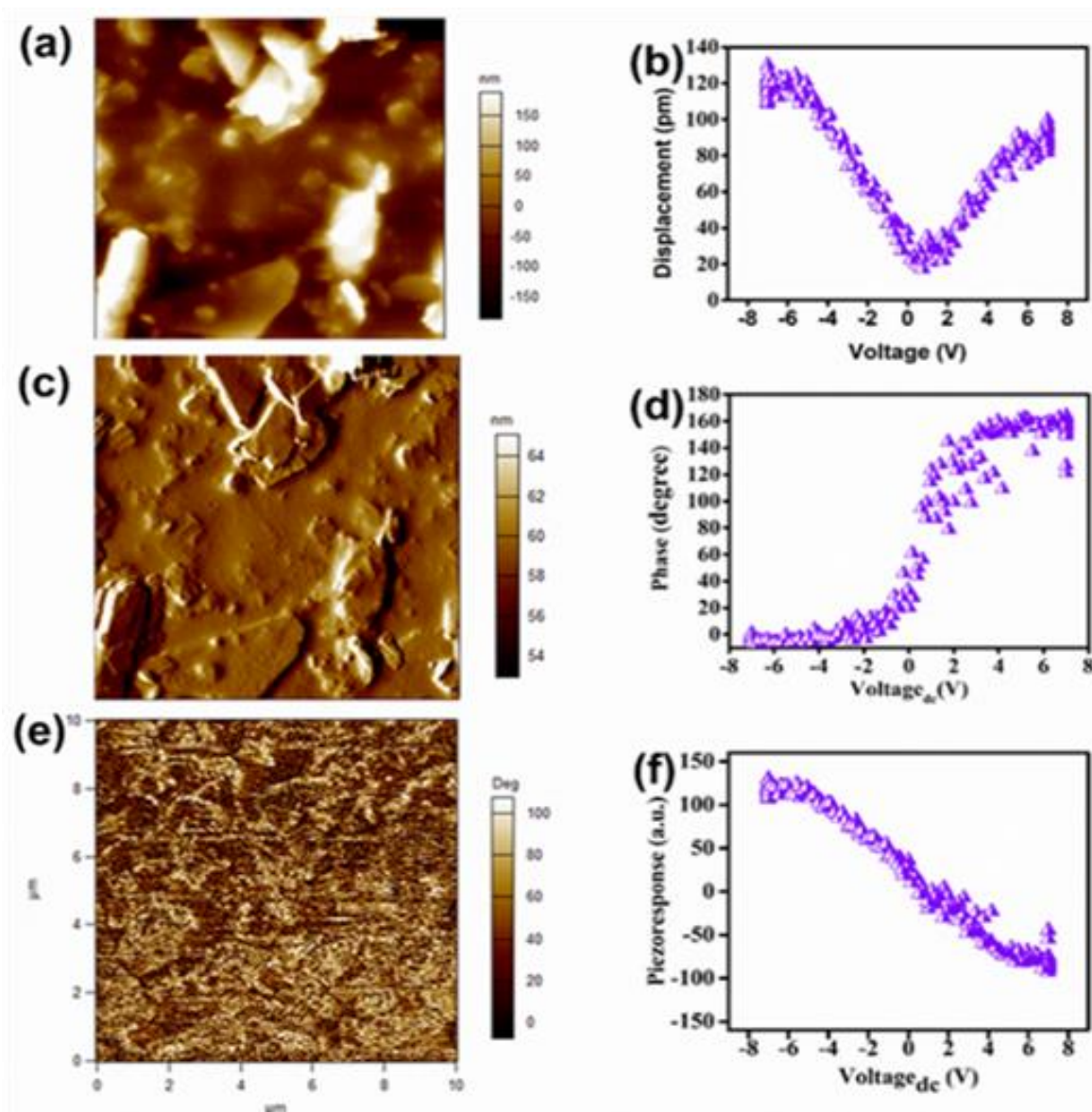


Figure 14 Piezoelectricity force measurement (PFM) images of BP nanosheets. (a) topography of BP nanosheets, (b) Amplitude so-called “butterfly” loop, (c) amplitude topography of BP nanosheets, (e) Phase topography on applying -8 to 8 V biased voltage, (d) Phase hysteresis loop and (f) Piezoresponse hysteresis loop

2.7 Computational Density functional theory (DFT) calculations

To gain some preliminary microscopic understanding of the observed mechanical response, we carried out first-principles density functional calculations. We performed density functional

theory calculations within the projector augmented wave formalism⁴² with a plane-wave cutoff of 400 eV as implemented in Vienna Ab initio Simulation Package (VASP).^{43,44} The exchange-correlation was described with the Perdew-Burke-Ernzerhof form of generalized gradient approximation.⁴⁵ The monolayer phosphorene was modelled using a 2x2 supercell. The periodic images were separated by a vacuum of 15 Å. The reciprocal space integrations were carried out using $11 \times 8 \times 1$ Monkhorst-Pack k -points, and the full structural optimizations were carried until the energy and force components are below a threshold of 10^{-6} eV and 5×10^{-3} eV/Å, respectively. Here, among the two strain fields in action in the experiment, we modelled only the compressive strain, whereas did not consider the bending strain field. We particularly investigated the change in the intralayer and interlayer charge distribution due to the strain induced by the impact force. While phosphorene has a centrosymmetric $Pmna$ structure, under a compressive vertical strain gradient, the crystal structure becomes non-centrosymmetric with $Pma2$ space group (Figure 15(a)). The vertical strain leads to a reduction in the distance between the two half-layers, which results in a reduction in the bond lengths of the top half-layer (Figure 15(b)). Thus, we observe a redistribution of intra-layer electron charge density, which is evident from the calculated plane-averaged electrostatic potential along the direction of the applied vertical strain (Figure 15(c) and 16 (a and b)). Further, the difference in the electrostatic potential between two half-layer increases with increasing vertical strain. Thus, a distinct potential energy surface developed at the two half-layers due to the non-uniform vertical compression leads to a net intra-layer dipole. Further, in the case of few-layer phosphorene, the vertical strain should also manifest in an inter-layer polarization due to a differential electronic charge distribution originating from the differential distortion of the individual phosphorene layers. We calculated the low-energy electron charge densities for the compressed phosphorene, and compared it with the unstrained counterpart, which shows the existence of a charge density gradient along with the applied force (Figure 15(d) and 16 (c)). Thus, we anticipate that a combined effect of compressive and bending strain fields on few-layer phosphorene will lower the crystal symmetry, and result in an out-of-plane electric polarization with both intralayer and interlayer contributions.

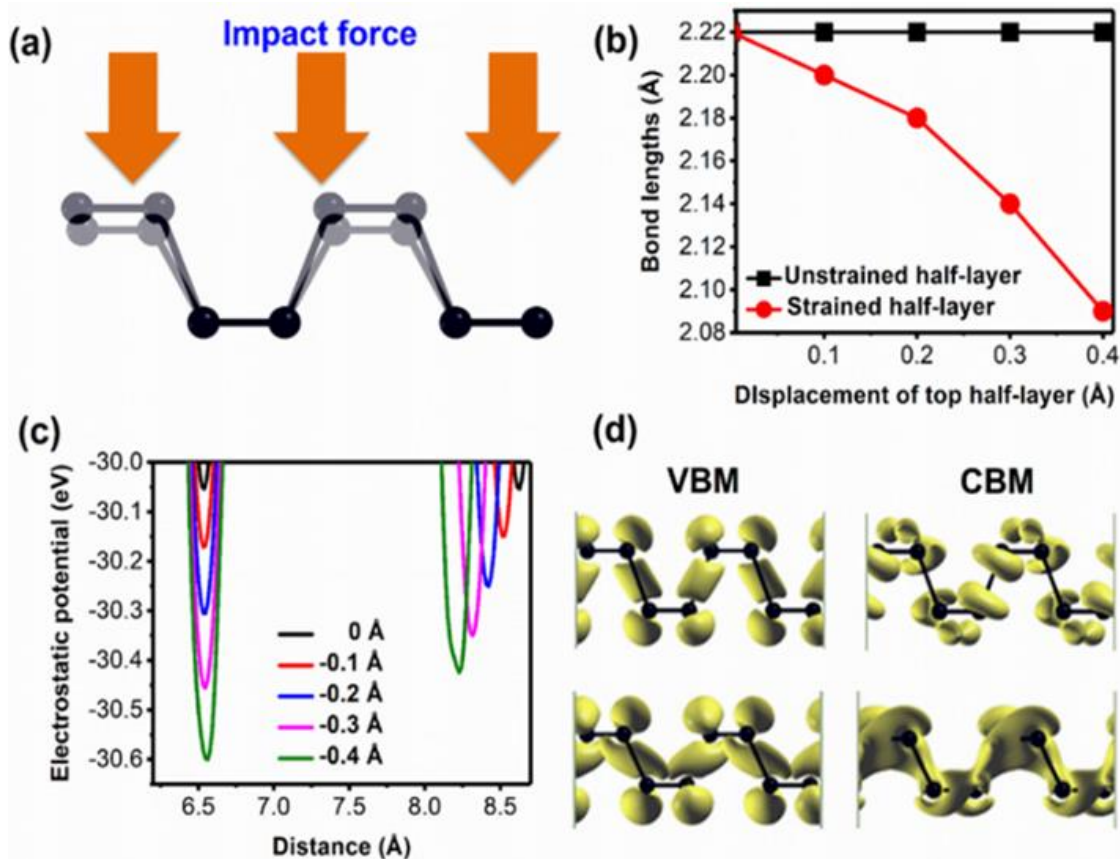


Figure 15 First-principles density functional calculations: (a) A non-uniform strain on phosphorene results in a noncentrosymmetric structure ($Pmna$ to $Pma2$), (b) Under increasing strain, the in-plane bonds of top half-layer are compressed. Black (square) points refer to the bond lengths along the unrelaxed bottom half-layer while the red (circle) points indicate the altered bond lengths within the top half-layer, (c) The intralayer electrostatic potential changes with increasing strain, calculated plane-averaged electrostatic potential along the direction of strain and (d) Interlayer polarization in few-layer phosphorene: Band decomposed charge densities of the low-energy states for the unstrained (top row) and strained (bottom row) phosphorene (value: $0.01 e/\text{\AA}^3$). A charge density gradient develops along the direction of applied force.

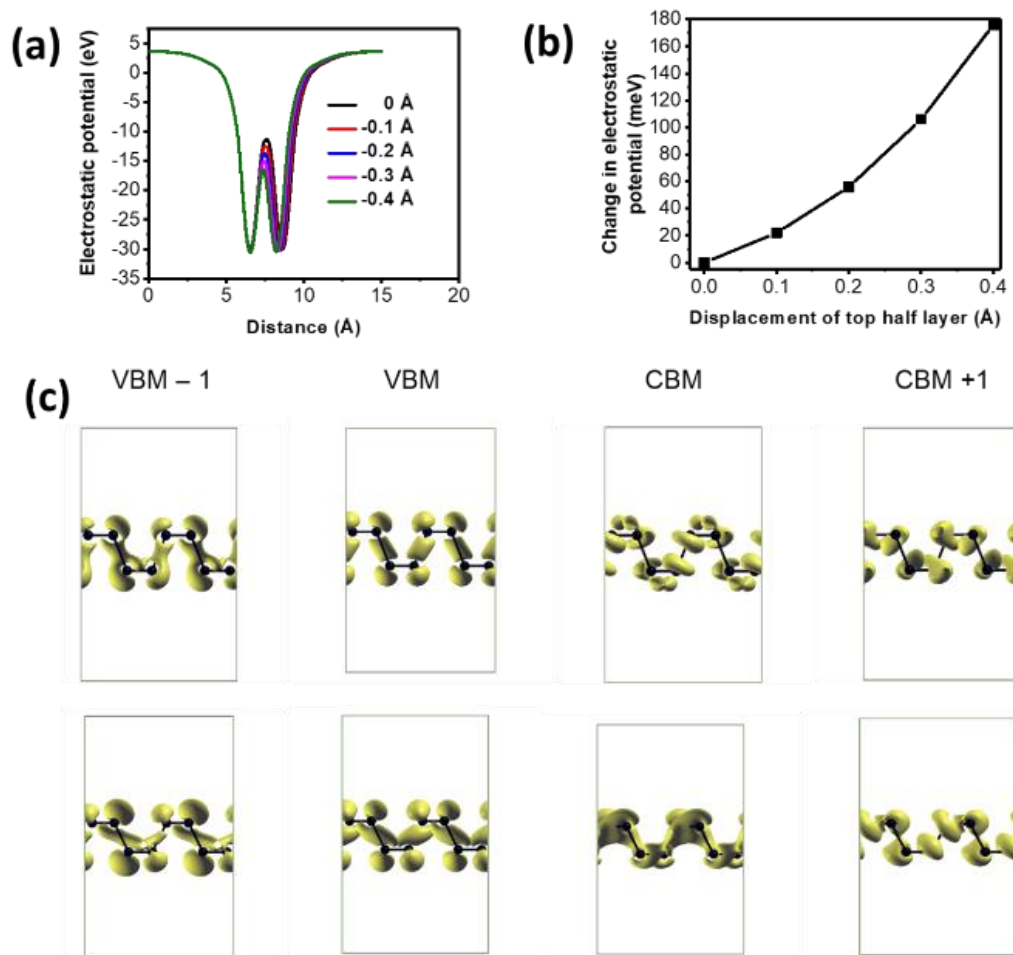


Figure 16 The intralayer electrostatic potential changes with increasing strain. (a) Calculated plane-averaged electrostatic potential along the direction of strain, (b) A difference in the potential energy emerges for the two half-layers for an increasing compressive strain and (c) Interlayer polarization in few-layer black phosphorus: Band decomposed charge densities of the low-energy states for the unstrained (top row) and strained (bottom row) phosphorene (value: $0.01 e/\text{\AA}^3$). A charge density gradient develops along the direction of applied force. Here, VBM and CBM refer valence band maximum and conduction band minimum.

2.8 Device applications

Given the high powering capability of our device configuration, we also tested the effective energy harvesting performance of this device for three different application domains.^{46, 47} In the first case,

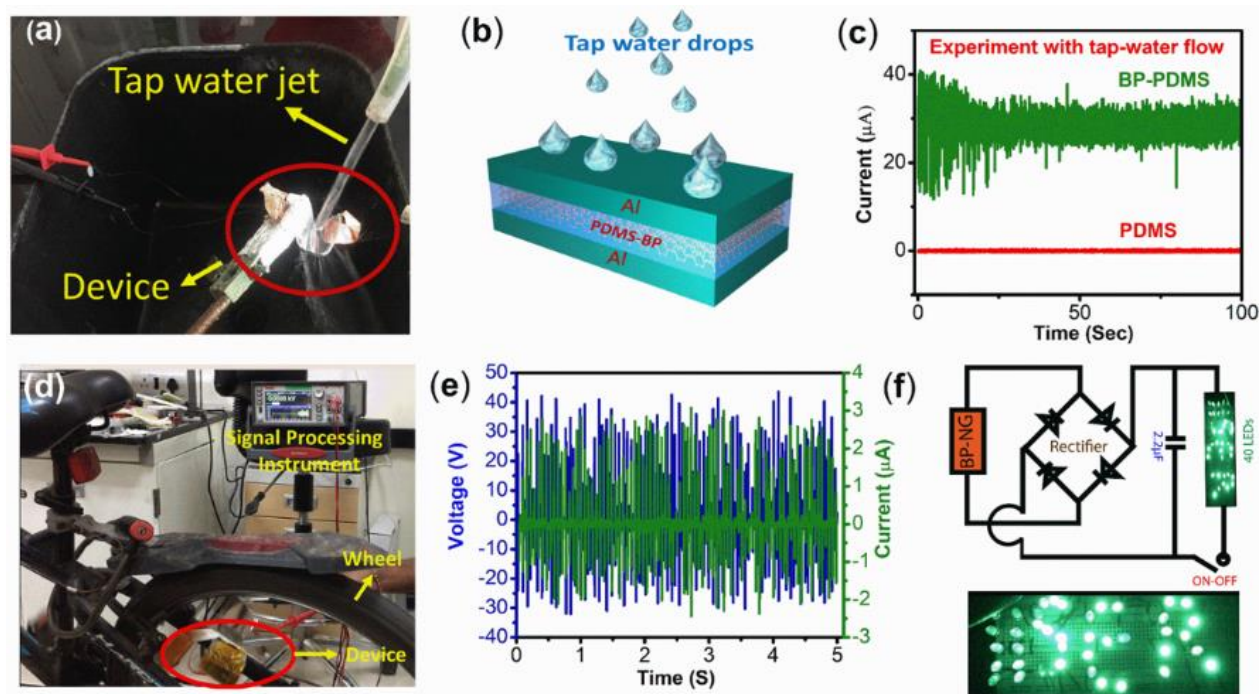


Figure 17 Energy harvesting application of PDMS-BP nanosheets device: (a) Demonstration of mechanical energy harvester for tap water flow, (b) schematic of PDMS-BP nanosheets NG for tap water flow, (c) Short circuit current resulting from the experiment, (d) Demonstration of energy harvesting from two-wheeler wheel motion, (e) Open circuit voltage and short-circuit current from wheel motion, and (f) Schematic diagram of the rectifying circuit to store current and application of glowing 41 LEDs.

we examined the possibility of efficient energy harvesting from water flow or water-impact systems, which could encompass situations from an everyday shower, to flowing water from taps or turbulent flows in canals to natural waterfalls or raindrops. For the new application, we took 7 cm² BP-PDMS film and sandwiched in between two aluminium electrodes. We put the whole device below the tap water flow (flow rate 7.5 litres/min) at an angle of about 45 degrees and performed the current and voltage measurements via Keithley DMM 7510 multimeter. Very interestingly, we found (Figure 17(a, b, c)) that our BP-PDMS large area device rendered a nearly stable mean high current of about 30-40 µA at a low voltage of about 0.5 V. Thus, in this

mode the same device operated as low voltage high current device, due to numerous mini impacts of water mass. Importantly, in this case, there is also an interesting element of sliding friction (tribo) effect between the impinging and sliding liquid droplets and the device surface. It is important to note that without the presence of BP sheets, the voltage from only the PDMS device was extremely low. Thus the external tribotronic effect synergistically integrates with the internal device performance and renders a new dimension to the generated power.

For the second application, we considered the potential of our PDMS-BP device for harvesting energy from vehicular wheel movement. We coupled this device with a bicycle and used the fluttering motion of a laterally stationed device against the spokes of the wheel to harvest motion energy in a pulsed mode ((Figure 17(d, e). To protect the soft matter of the device from erosion due to strike by the spoke, a thin stainless steel foil was installed on the device. As seen, we generated a high-frequency peak-to-peak voltage output of about 65 V and a current density of 68.75 mA/cm². Interestingly, the external friction of the device surface protected by a thin stainless steel sheet must induce charge separation (spray) which appears to synergistically cooperate with the other internal multi-mechanisms of the device. Again, the external tribotronic effect adds an interesting element as the device parameters reflect higher voltage and lower current densities than the one obtained from the water flow experiments.

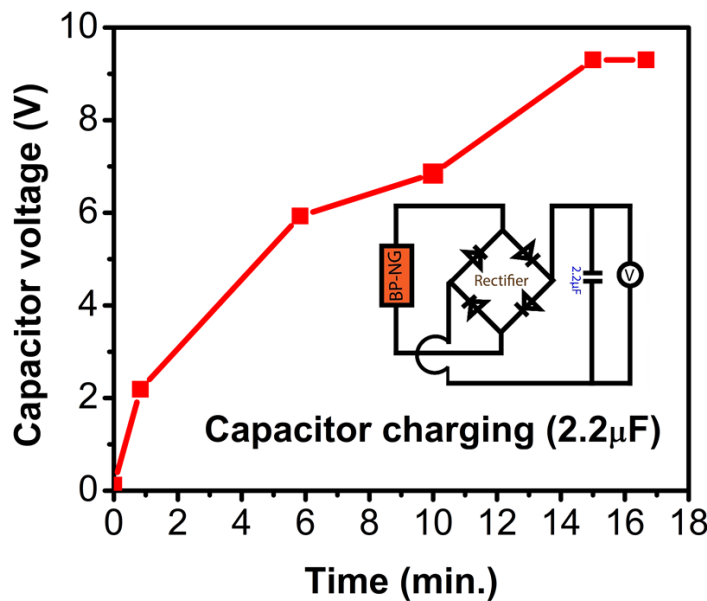


Figure 17 The Power generated from NG stored in 2.2 μF capacitors using a full-wave rectifier Voltage across the capacitor that reached up to 9.30 Volt in 17 minutes.

Finally, in the third application, the power generated from the 0.2 wt.% of PDMS-BP nanosheets device was stored using a full-wave bridge rectifier as shown by the equivalent circuit in Figure 17 (f). The PDMS-BP nanosheets nanogenerator was connected through a full-wave bridge rectifier consisting of four diodes, which converts the generated voltage to direct current (DC) as shown in Figure 18. The output voltage across a 2.2 μF capacitor reached up to 9.30 V in 17 minutes, which establishes a good charging rate in a simple and economical design.¹⁵ Also, under the force of 40 N and a frequency of 25 Hz applied continuously for a period of 10 seconds, we found a set of 40 LEDs could light up in one shot through this charging capacitor.

2.9 Analyses of experimental results

It is now useful to put the different results into perspective based on the available information about black phosphorous or few-layer BP. First, BP is a layered system which is centrosymmetric.⁴⁸ Hence, it is not expected to render ferroelectricity or piezoelectricity in its stand-alone bulk configuration. As discussed in the introduction, however, the works of Michel and Verberck, Reed and co-workers, and Z. L. Wang and co-workers have demonstrated that monolayers or few odd-numbered layered configurations of 2D materials could exhibit piezoelectricity.^{8,29} In our case, the as-synthesized FLBP would statistically contain 50% of odd-numbered layers which would have strong piezoelectric effects. Another avenue for induction of piezoelectric response in an otherwise non-piezoelectric system is surface functionalization by way of selective atomic or molecular adsorption.^{29,49} In our case, the n-layered BP flakes are embedded in PDMS matrix, and the molecular interaction at the interface between BP and PDMS can serve the functionalization effect. It may be noted that in the Black phosphorus-PDMS nanocomposite Si-O bonds chemically interact with the phosphorus (as evidenced by the redshift in Raman spectra, Figure 4) rendering compactness, strain, and high density of FLBP in the PDMS matrix; while in case of cellulose used in the previous work,³² the interaction of the C-O bonds with black phosphorus does not change the configuration of the film since no shift in Raman spectra was observed. Finally, the Si-O bond of PDMS possesses higher dipole moment ($\sim 0.6 \text{ D}$)⁵⁰ than the C-O ($\sim 0.16 \text{ D}$)⁵¹ bond of the cellulose polymer chain which could lead to higher polarization in BP-PDMS nanocomposite film than the Cellulose-BP film. Thus the polymer used to form the active layer of the device does also make a difference in the performance.

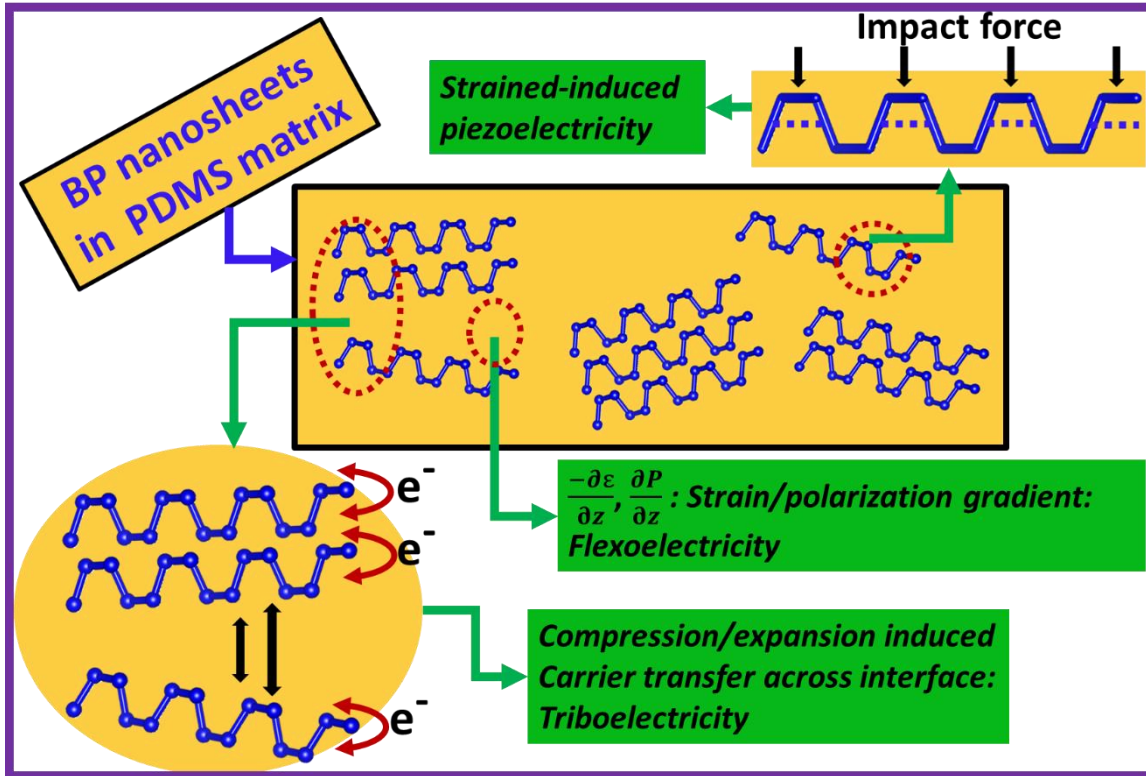


Figure 18 Schematic of multi-mechanism effect proposed by experimental analysis

Since an effective piezoelectric character was noted in the BP nanosheets in the PFM experiment, one could envision that compression of the PDMS-BP nanosheets composite against a fixed bottom plate in a transient mode would induce distortions generating electric dipole moments. Indeed, Fu and Cross have shown that by properly manipulating the phases in flexoelectric-type composites one could generate a direct piezo-response.⁵²

In our case, the origin of the observed high voltages may thus be traced to three key aspects of the architecture, namely the mechanically unique puckered 2D material (phosphorene) embedded in the dielectric matrix, the properties of the interfaces between the embedded 2D material (FLBP) and the dielectric, and the existence of high internal strain gradients.

Finally, two more points need to be stated. First, the strength of the effect in our case in the bending mode operation was noted to be lower than that in the impact based compaction and

release operation. This is exactly opposite to the behaviour noted by Cary Pint, and workers³⁴ stated earlier, suggesting a different mechanism and hence operational novelty of our device architecture. Second, by way of two application specific demonstrations (water impact and flutter modulation by spokes of wheels) of the high powering capability of our device, we introduce a new element

Table 2 Comparison of the performance of our device with recently reported black phosphorus-based devices.

Reference	Material/Device	Peak to Peak maximum Voltage (V)	Current Density (mA/m ²)	Power Density (mW/m ²)	Volume Power Density (kW/m ³)	Piezoelectric force microscopy (PFM) study
ACS Energy Lett. 2017, 2, 1797	Electrochemical Device using Sodiated BP	0.013	0.5	0.42	Not Discussed	No
Adv. Mater. Interfaces 2017, 4, 1700651	Cellulose-Phosphorene Hybrid Paper	7.2	0.18	0.11	Not Discussed	No
Adv. Mater. 2018, 30, 1705088	MoS ₂ /BP Turbotronic gate FET	--	--	--	Not Discussed	No
Our data	FLBP/PDMS Multi-Mechanism System	350	12.8	1400	2	Yes

of external triboelectric effect interacting synergistically with the internal device mechanisms to boost the powering performance significantly (Figure 19). Finally, we compare in Table 2 the performance of our device with other black phosphorous based devices.

2.10 Conclusions

A mechanical energy harvester with black phosphorus (BP) nanosheets uniformly dispersed in PDMS (Polydimethylsiloxane) is shown to exhibit an exceptionally high voltage output of maximum peak to peak voltage output of the order of ± 350 Volts (maximum current density of 12.8 mA/m^2) under an applied impact force of 40 Newton (N) at a frequency of 20 to 25 Hz. This corresponds to an areal power density of 1400 mW/m^2 and a volume power density of 2 kW/m^3 , with active material (BP) contribution of 0.35 W/g . The 2D BP nanosheets themselves exhibit a fairly high piezoelectric coefficient of $\sim 20 \text{ pm/V}$. The DFT calculations suggest the existence of strain-induced polarization via deformation-induced redistribution of intra-layer electron charge density. To our knowledge, this is the first demonstration of a very strong mechano-electronic response from a device based on few-layer black phosphorous, which can be used for real-life applications.

2.11 References

1. Yazyev, O. V.; Chen, Y. P., Polycrystalline graphene and other two-dimensional materials. *Nature Nanotechnology* **2014**, *9*, 755.
2. Wang, Q. H.; Kalantar-Zadeh, K.; Kis, A.; Coleman, J. N.; Strano, M. S., Electronics and optoelectronics of two-dimensional transition metal dichalcogenides. *Nature Nanotechnology* **2012**, *7*, 699.
3. Butler, S. Z.; Hollen, S. M.; Cao, L.; Cui, Y.; Gupta, J. A.; Gutiérrez, H. R.; Heinz, T. F.; Hong, S. S.; Huang, J.; Ismach, A. F.; Johnston-Halperin, E.; Kuno, M.; Plashnitsa, V. V.; Robinson, R. D.; Ruoff, R. S.; Salahuddin, S.; Shan, J.; Shi, L.; Spencer, M. G.; Terrones, M.; Windl, W.; Goldberger, J. E., Progress, Challenges, and Opportunities in Two-Dimensional Materials Beyond Graphene. *ACS Nano* **2013**, *7* (4), 2898-2926.
4. Jariwala, D.; Marks, T. J.; Hersam, M. C., Mixed-dimensional van der Waals heterostructures. *Nature Materials*, **2016**, *16*, 170.
5. Qi, J.; Lan, Y.-W.; Stieg, A. Z.; Chen, J.-H.; Zhong, Y.-L.; Li, L.-J.; Chen, C.-D.; Zhang, Y.; Wang, K. L., Piezoelectric effect in chemical vapour deposition-grown atomic-monolayer triangular molybdenum disulfide piezotronics. *Nature Communications* **2015**, *6*, 7430.

6. Lin, P.; Zhu, L.; Li, D.; Xu, L.; Pan, C.; Wang, Z., Piezo-Phototronic Effect for Enhanced Flexible MoS₂/WSe₂ van der Waals Photodiodes. *Advanced Functional Materials* **2018**, *28* (35), 1802849.
7. Carvalho, A.; Wang, M.; Zhu, X.; Rodin, A. S.; Su, H.; Castro Neto, A. H., Phosphorene: from theory to applications. *Nature Reviews Materials* **2016**, *1*, 16061.
8. Wu, W.; Wang, L.; Li, Y.; Zhang, F.; Lin, L.; Niu, S.; Chenet, D.; Zhang, X.; Hao, Y.; Heinz, T. F.; Hone, J.; Wang, Z. L., Piezoelectricity of single-atomic-layer MoS₂ for energy conversion and piezotronics. *Nature* **2014**, *514*, 470.
9. Xu, S.; Qin, Y.; Xu, C.; Wei, Y.; Yang, R.; Wang, Z. L., Self-powered nanowire devices. *Nature Nanotechnology* **2010**, *5*, 366.
10. Li, A.; Zi, Y.; Guo, H.; Wang, Z. L.; Fernández, F. M., Triboelectric nanogenerators for sensitive nano-coulomb molecular mass spectrometry. *Nature Nanotechnology* **2017**, *12*, 481.
11. Li, W.; Torres, D.; Díaz, R.; Wang, Z.; Wu, C.; Wang, C.; Lin Wang, Z.; Sepúlveda, N., Nanogenerator-based dual-functional and self-powered thin patch loudspeaker or microphone for flexible electronics. *Nature Communications* **2017**, *8*, 15310.
12. Wen, Z.; Yeh, M.-H.; Guo, H.; Wang, J.; Zi, Y.; Xu, W.; Deng, J.; Zhu, L.; Wang, X.; Hu, C.; Zhu, L.; Sun, X.; Wang, Z. L., Self-powered textile for wearable electronics by hybridizing fiber-shaped nanogenerators, solar cells, and supercapacitors. *Science Advances* **2016**, *2* (10), e1600097.
13. Xu, M.; Wang, P.; Wang, Y.-C.; Zhang, S. L.; Wang, A. C.; Zhang, C.; Wang, Z.; Pan, X.; Wang, Z. L., A Soft and Robust Spring Based Triboelectric Nanogenerator for Harvesting Arbitrary Directional Vibration Energy and Self-Powered Vibration Sensing. *Advanced Energy Materials* **2018**, *8* (9), 1702432.
14. Cha, S. N.; Seo, J.-S.; Kim, S. M.; Kim, H. J.; Park, Y. J.; Kim, S.-W.; Kim, J. M., Sound-Driven Piezoelectric Nanowire-Based Nanogenerators. *Advanced Materials* **2010**, *22* (42), 4726-4730.
15. Chun, J.; Ye, B. U.; Lee, J. W.; Choi, D.; Kang, C.-Y.; Kim, S.-W.; Wang, Z. L.; Baik, J. M., Boosted output performance of triboelectric nanogenerator via electric double layer effect. *Nature Communications* **2016**, *7*, 12985.
16. Liang, Q.; Zhang, Q.; Yan, X.; Liao, X.; Han, L.; Yi, F.; Ma, M.; Zhang, Y., Recyclable and Green Triboelectric Nanogenerator. *Advanced Materials* ,**2017**, *29* (5), 1604961.
17. Zeng, W.; Tao, X.-M.; Chen, S.; Shang, S.; Chan, H. L. W.; Choy, S. H., Highly durable all-fiber nanogenerator for mechanical energy harvesting. *Energy & Environmental Science* **2013**, *6* (9), 2631-2638.
18. Chen, S.; Tao, X.; Zeng, W.; Yang, B.; Shang, S., Quantifying Energy Harvested from Contact-Mode Hybrid Nanogenerators with Cascaded Piezoelectric and Triboelectric Units. *Advanced Energy Materials* **2017**, *7* (5), 1601569.
19. Wang, Z. L.; Chen, J.; Lin, L., Progress in triboelectric nanogenerators as a new energy technology and self-powered sensors. *Energy & Environmental Science* **2015**, *8* (8), 2250-2282.
20. Briscoe, J.; Dunn, S., Piezoelectric nanogenerators – a review of nanostructured piezoelectric energy harvesters. *Nano Energy* **2015**, *14*, 15-29.
21. Ghosh, S. K.; Mandal, D., Efficient natural piezoelectric nanogenerator: Electricity generation from fish swim bladder. *Nano Energy* **2016**, *28*, 356-365.
22. Kim, S.; Gupta, M. K.; Lee, K. Y.; Sohn, A.; Kim, T. Y.; Shin, K.-S.; Kim, D.; Kim, S. K.; Lee, K. H.; Shin, H.-J.; Kim, D.-W.; Kim, S.-W., Transparent Flexible Graphene Triboelectric Nanogenerators. *Advanced Materials* **2014**, *26* (23), 3918-3925.

23. Lee, J.-H.; Park, J. Y.; Cho, E. B.; Kim, T. Y.; Han, S. A.; Kim, T.-H.; Liu, Y.; Kim, S. K.; Roh, C. J.; Yoon, H.-J.; Ryu, H.; Seung, W.; Lee, J. S.; Lee, J.; Kim, S.-W., Reliable Piezoelectricity in Bilayer WSe₂ for Piezoelectric Nanogenerators. *Advanced Materials* **2017**, *29* (29), 1606667.
24. Duerloo, K.-A. N.; Ong, M. T.; Reed, E. J., Intrinsic Piezoelectricity in Two-Dimensional Materials. *The Journal of Physical Chemistry Letters* **2012**, *3* (19), 2871-2876.
25. Droth, M.; Burkard, G.; Pereira, V. M., Piezoelectricity in planar boron nitride via a geometric phase. *Physical Review B* **2016**, *94* (7), 075404.
26. Han, S. A.; Lee, K. H.; Kim, T.-H.; Seung, W.; Lee, S. K.; Choi, S.; Kumar, B.; Bhatia, R.; Shin, H.-J.; Lee, W.-J.; Kim, S.; Kim, H. S.; Choi, J.-Y.; Kim, S.-W., Hexagonal boron nitride assisted growth of stoichiometric Al₂O₃ dielectric on graphene for triboelectric nanogenerators. *Nano Energy* **2015**, *12*, 556-566.
27. K. H. Michel, B. V., Theory of phonon dispersions and piezoelectricity in multilayers of hexagonal boron-nitride. *physica status solidi (b)* **2011**, *248* (11), 2720-2723.
28. Ong, M. T.; Reed, E. J., Engineered Piezoelectricity in Graphene. *ACS Nano* **2012**, *6* (2), 1387-1394.
29. Noor-A-Alam, M.; Kim, H. J.; Shin, Y.-H., Dipolar polarization and piezoelectricity of a hexagonal boron nitride sheet decorated with hydrogen and fluorine. *Physical Chemistry Chemical Physics* **2014**, *16* (14), 6575-6582.
30. Churchill, H. O. H.; Jarillo-Herrero, P., Phosphorus joins the family. *Nature Nanotechnology* **2014**, *9*, 330.
31. Li, L.; Yu, Y.; Ye, G. J.; Ge, Q.; Ou, X.; Wu, H.; Feng, D.; Chen, X. H.; Zhang, Y., Black phosphorus field-effect transistors. *Nature Nanotechnology* **2014**, *9*, 372.
32. Cui, P.; Parida, K.; Lin, M.-F.; Xiong, J.; Cai, G.; Lee, P. S., Transparent, Flexible Cellulose Nanofibril–Phosphorene Hybrid Paper as Triboelectric Nanogenerator. *Advanced Materials Interfaces* **2017**, *4* (22), 1700651.
33. Gao, G.; Wan, B.; Liu, X.; Sun, Q.; Yang, X.; Wang, L.; Pan, C.; Wang, Z. L., Tunable Tribotronic Dual-Gate Logic Devices Based on 2D MoS₂ and Black Phosphorus. *Advanced Materials*, **2018**, *30* (13), 1705088.
34. Muralidharan, N.; Li, M.; Carter, R. E.; Galioto, N.; Pint, C. L., Ultralow Frequency Electrochemical–Mechanical Strain Energy Harvester Using 2D Black Phosphorus Nanosheets. *ACS Energy Letters* **2017**, *2* (8), 1797-1803.
35. Yasaei, P.; Kumar, B.; Foroozan, T.; Wang, C.; Asadi, M.; Tuschel, D.; Indacochea, J. E.; Klie, R. F.; Salehi-Khojin, A., High-Quality Black Phosphorus Atomic Layers by Liquid-Phase Exfoliation. *Advanced Materials* **2015**, *27* (11), 1887-1892.
36. Ding, R.; Liu, H.; Zhang, X.; Xiao, J.; Kishor, R.; Sun, H.; Zhu, B.; Chen, G.; Gao, F.; Feng, X.; Chen, J.; Chen, X.; Sun, X.; Zheng, Y., Flexible Piezoelectric Nanocomposite Generators Based on Formamidinium Lead Halide Perovskite Nanoparticles. *Advanced Functional Materials* **2016**, *26* (42), 7708-7716.
37. Ding, R.; Zhang, X.; Chen, G.; Wang, H.; Kishor, R.; Xiao, J.; Gao, F.; Zeng, K.; Chen, X.; Sun, X. W.; Zheng, Y., High-performance piezoelectric nanogenerators composed of formamidinium lead halide perovskite nanoparticles and poly(vinylidene fluoride). *Nano Energy* **2017**, *37*, 126-135.
38. Lee, K. Y.; Kim, D.; Lee, J.-H.; Kim, T. Y.; Gupta, M. K.; Kim, S.-W., Unidirectional High-Power Generation via Stress-Induced Dipole Alignment from ZnSnO₃ Nanocubes/Polymer Hybrid Piezoelectric Nanogenerator. *Advanced Functional Materials* **2014**, *24* (1), 37-43.

39. Zhang, G.; Liao, Q.; Zhang, Z.; Liang, Q.; Zhao, Y.; Zheng, X.; Zhang, Y., Novel Piezoelectric Paper-Based Flexible Nanogenerators Composed of BaTiO₃ Nanoparticles and Bacterial Cellulose. *Advanced Science* **2016**, *3* (2), 1500257.
40. Wang, S.; Zi, Y.; Zhou, Y. S.; Li, S.; Fan, F.; Lin, L.; Wang, Z. L., Molecular surface functionalization to enhance the power output of triboelectric nanogenerators. *Journal of Materials Chemistry A* **2016**, *4* (10), 3728-3734.
41. Laurenti, M.; Stassi, S.; Lorenzoni, M.; Fontana, M.; Canavese, G.; Cauda, V.; Pirri, C. F., Evaluation of the piezoelectric properties and voltage generation of flexible zinc oxide thin films. *Nanotechnology* **2015**, *26* (21), 215704.
42. Giustino, F., Electron-phonon interactions from first principles. *Reviews of Modern Physics* **2017**, *89* (1), 015003.
43. Kresse, G.; Hafner, J., Ab initio molecular dynamics for liquid metals. *Physical Review B* **1993**, *47* (1), 558-561.
44. Ayala, P.; Arenal, R.; Loiseau, A.; Rubio, A.; Pichler, T., The physical and chemical properties of heteronanotubes. *Reviews of Modern Physics* **2010**, *82* (2), 1843-1885.
45. Perdew, J. P.; Burke, K.; Ernzerhof, M., Generalized Gradient Approximation Made Simple. *Physical Review Letters* **1996**, *77* (18), 3865-3868.
46. Jeong, C. K.; Cho, S. B.; Han, J. H.; Park, D. Y.; Yang, S.; Park, K.-I.; Ryu, J.; Sohn, H.; Chung, Y.-C.; Lee, K. J., Flexible highly-effective energy harvester via crystallographic and computational control of nanointerfacial morphotropic piezoelectric thin film. *Nano Research* **2017**, *10* (2), 437-455.
47. Wang, H. S.; Jeong, C. K.; Seo, M.-H.; Joe, D. J.; Han, J. H.; Yoon, J.-B.; Lee, K. J., Performance-enhanced triboelectric nanogenerator enabled by wafer-scale nanogrates of multistep pattern downscaling. *Nano Energy* **2017**, *35*, 415-423.
48. Brown, A.; Rundqvist, S., Refinement of the crystal structure of black phosphorus. *Acta Crystallographica* **1965**, *19* (4), 684-685.
49. Yin, H.; Zheng, G.-P.; Gao, J.; Wang, Y.; Ma, Y., Enhanced piezoelectricity of monolayer phosphorene oxides: a theoretical study. *Physical Chemistry Chemical Physics* **2017**, *19* (40), 27508-27515.
50. Mark, J. E., Dipole Moments of Dimethylsiloxane Chains. *The Journal of Chemical Physics* **1968**, *49* (3), 1398-1402.
51. Harrison, J. F., Relationship between the Charge Distribution and Dipole Moment Functions of CO and the Related Molecules CS, SiO, and SiS. *The Journal of Physical Chemistry A* **2006**, *110* (37), 10848-10857.
52. Fu, J. Y.; Cross, L. E., Separate control of direct and converse piezoelectric effects in flexoelectric piezoelectric composites. *Applied Physics Letters* **2007**, *91* (16), 162903.

Chapter 3

Seed Power: Natural seed and electrospun PVDF nanofiber-based triboelectric nanogenerators with high output power density

Abstract

Triboelectric nanogenerators (TENGs) based on natural seeds and electrospun PVDF fibers are reported. The nanofibers are specifically used to enhance the triboelectric effects. A mustard (flax) seed-based TENG renders an impressively high electrical output with an average open-circuit voltage of 84 V (126 V) and maximum power density 334 mW/m² (324 mW/m²) under an impact force of 40 N at 25 Hz. Basil seeds are relatively weaker in power delivery. By comparing the seed crust properties and TENG performances, we analyze the powering capability in terms of the cellulose content in the crust, dielectric constant and surface morphological features.

The following paper has been published based on the work documented in this chapter. **Singh, S. K.**; Kumar, P.; Magdum, R.; Khandelwal, U.; Deswal, S.; More, Y.; Muduli, S.; Boomishankar, R.; Pandit, S.; Ogale, S., Seed Power: Natural Seed and Electrospun Poly(vinyl difluoride) (PVDF) Nanofiber Based Triboelectric Nanogenerators with High Output Power Density. ACS Applied Bio Materials 2019, 2 (8), 3164-3170. Copyright permission has been obtained for the complete article from the American Chemical Society.

3.1 Introduction

Nanogenerators (NGs) and Triboelectric Nanogenerators (TENGs) have acquired prominence in recent years as low, medium and even high power mechanical energy harvesting devices. While the term NG is generally used for energy harvesting realized via polarization changes such as those involved in piezoelectric or flexoelectric effects, the triboelectric or friction-based harvester designs involving separation of charges are now separately identified as TENGs. Over the past decade, the performance features of these devices have dramatically improved with many real-life application demonstrations, thanks to the immense pioneering research contributions by Z. L. Wang and coworkers¹⁻⁴ as well as several other research groups.⁵⁻⁸ One of the highlights of research on NGs and TENGs is the novelty and diversity of materials and device architectures which emphasize the interplay of the bulk, surface and interface polarization and charge transfer effects in multiple schemes.⁹⁻¹² In most cases, however, inorganic and organic laboratory materials are employed as active materials in these devices. While nature offers a plethora of complex functional molecular assemblies which have interesting responses to electrostatic perturbations, only a few of these have been examined for possible use as active materials in NG, and TENG designs.¹³⁻¹⁵ For example, Dong Sung Kim and co-workers harvested energy from the natural lotus leaf-based TENG, employing contact electrification of discrete liquid-solid interface exploiting the natural super-hydrophobic lotus leaf surface, resulting in the maximum output power of $\approx 1.5 \text{ mW/m}^2$.¹⁴ Xia Cao and co-workers fabricated a TENG device utilizing natural leaves, displaying maximum output power density of $\approx 45 \text{ mW/m}^2$.¹⁵

It is a common experience that when mustard seeds are shaken in a plastic container, they begin to climb up along the walls and dance due to electrostatic charging. This clearly implies that the surface of mustard seed can facilitate easy charge transfer in a triboelectric (friction) situation.^{9, 16, 17} This observation inspired us to test different seeds as active materials in a TENG device design, and as shown in this chapter, we indeed obtained some exciting results in terms of the generated power, with a potential for realistic applications. Importantly, the seed surfaces are also quite tough and robust for mild impacts of a soft material used to extract the charges. Hence such devices promise good cycle life.

We employed three natural seeds (mustard, basil, flax) as promising triboelectric materials, operating in the contact separation mode of TENG.^{2, 18, 19} All these seeds are quite abundant and cheap, and therefore can be utilized for environment-friendly TENG construction. Our specifically designed mustard seed-based triboelectric nanogenerator (S-TENG) showed an impressive maximum output power density of 334 mW/m² which, to the best of our knowledge, is the highest *vis a vis* most natural product based NGs and TENGs.¹³⁻¹⁵ Our detailed analysis of the molecular constitution of seed crust suggests that the powering capability of S-TENGs relates to the carbohydrate content in the crust.

3.2 Experimental:

3.2.1 Materials

Brown mustard seeds are purchased from the Indian market. Dimethylformamide (DMF) (99.8% purity) and Poly (vinylidene difluoride) melt viscosity 20000-25000 poise are purchased from Sigma Aldrich. The spacer is purchased from 3M Tape. The aluminium sheet is purchased from physics equipments.

3.2.2 Synthesis of PVDF electrospun nanofibers mat

For the synthesis of electrospun nanofibers, 1 gram of PVDF pellets was stirred for 4hrs in 10 ml of DMF at 60 °C. The resulting transparent polymer solution was taken in 10ml syringe and subjected to electrospinning (ESPIN-Nano set up) at electric field pf 10 KV and a flow rate 0.7ml/hr. The electrospun nanofibers were directly collected on aluminium sheet of 0.05 mm thickness.

3.2.3 Extraction of glucosinolates and isothiocyanates

Mustard seed coat and core were manually separated. 200 mg of whole mustard seeds or seed coat or seed core were crushed in 80% aqueous methanol (vol/vol) using a ball mill. Samples were centrifuged for 10 min. at 10000 rpm and room temperature. Supernatants were incubated overnight at -20 °C for the precipitation of lipid contaminants, and then they were centrifuged for 10 min. at 10000 rpm and 4 °C. Clear supernatants were stored at -20 °C until the further use and were used as extracts for the identification and estimation of various glucosinolate and isothiocyanate contents.

3.2.4 Characterization of triboelectric layers

Structural analyses of all seeds were done using Fourier transform infrared spectroscopy (FTIR). Scanning electron microscopy images (SEM) of all seed's cover were obtained using Zeiss Ultra Plus FESEM.

3.2.5 LCMS analysis of glucosinolates and isothiocyanates

Mustard seed extracts were analyzed on UPLC-coupled X500R QTOF HRMS (Sciex, Framingham, MA, U.S.A) for qualitative and quantitative analysis of glucosinolates and isothiocyanates. 10 μ l of extract was injected in to LC and compounds were separated on Gemini C18 reverse phase column 50mm long, 4.6 mm wide with 5 μ M particle size and 110 $^{\circ}$ A pore size (Phenomenex, Torrance, CA, USA) by water (A): methanol (B) solvent gradient, at 0 min with 100 % (A)/ 0 % (B); 0-3 min 90 % (A)/ 10 % (B); 3-4 min 50 % (A)/50 % (B), 4-8 min 5 % (A)/ 95 % (B) held for 1 min and again back to 100 % (A)/ 0 % (B) in 2 min with flow rate 500 μ l min⁻¹.

MS data were acquired on ESI positive ion mode with IDA experiment using TOF mass range 100 to 1000 Da, declustering potential 80V, collision energy (CE) 40V, CE spread 20V and MSMS mass range 50 to 1000Da. Acquired data were analyzed using Analytics of SCIEX OS software (Sciex, Framingham, MA, U.S.A).

3.2.6 Carbohydrate estimation

Carbohydrates of mustard, basil and flax seeds and mustard seed coat and core were estimated using the Anthrone method. Determination of Starch and Cellulose contents were estimated with anthrone.²⁰ 3 mL acetic/nitric reagent was added to 1g tissue and mixed. The mixture was incubated at 100 $^{\circ}$ C in a water bath, for 30 min. The cooled mixture was centrifuged for 20 min, the supernatant was discarded, and the pellet was washed with distilled water. Pellet was incubated in 10 mL of 67% sulphuric acid for 1 h. This mixture was 10-folds diluted using the distilled water. 10 mL anthrone reagent was added to 1 mL of this mixture. The mixture was incubated at 100 $^{\circ}$ C in a water bath, for 10 min. The absorbance of the cooled mixtures was measured at 620 nm wavelength. Carbohydrate concentration was measured using the cellulose standard curve.

3.2.7 Fabrication of seed-based nanogenerator

At first, the adhesive paste was applied on an ITO coated PET. After this, immediately 2-gram mustard seeds were fixed in the viscous adhesive liquid and dried for 10 minutes. A 1mm thickness double-sided adhesive (3M tape) was placed at the corners of mustard seed coated substrate as a boundary spacer. For the second layer of triboelectric nanogenerator, electrospun nanofibers of PVDF were deposited on aluminium sheet. The second layer was put on top of the adhesive spacer (on the mustard layer), which maintains the gap between the two triboelectric layers. After this, the whole device was sealed with Kapton adhesive tape. The basil and flex seed-based devices were fabricated using a similar procedure. The active area of devices in all the instances was fixed at $3 \times 3 \text{ cm}^2$.

3.2.8 Output performance of Nanogenerator

Keithley multimeter (DMM 7510) was used to measure the open-circuit voltage at $10 \text{ M}\Omega$ input impedance operating on 40N impact force and with 25 Hz frequency. For the impact force and frequency source, a home-built modified sewing machine setup was used, and the force was measured force using a PASPORT Sensor. Short circuit current was also measured on Keithley multimeter (DMM 7510) with variable load resistances at $1 \text{ M}\Omega$, $10 \text{ M}\Omega$, $20 \text{ M}\Omega$ and $30 \text{ M}\Omega$.

3.2.9 Polarisation and dielectric measurements

Polarisation-voltage hysteresis loops and dielectric constants were measured on the PDMS composite films (as the binder for seeds) of different seeds using the Sawyer-Tower circuit. The films were sandwiched between two aluminium adhesive foils which served as the top and the bottom electrodes. All the measurements were performed on an aixACCT TF-2000E model hysteresis loop analyzer.

3.3 Results and discussion

The top surface of the active material (seeds in the present case) plays a pivotal role in the surface electrostatics and frictional charge separation. The image of Figure 1 (b) depicts the SEM image of the mustard seed surface. It displays polygon-grid-like (length scale of about 80-100 μm) surface morphology on a coarse scale, along with additional hierarchical submicron scale

undulations (Inset of figure 1(b)). Such hierarchically rough morphology of the surface is clearly helpful in the effectiveness of the process.

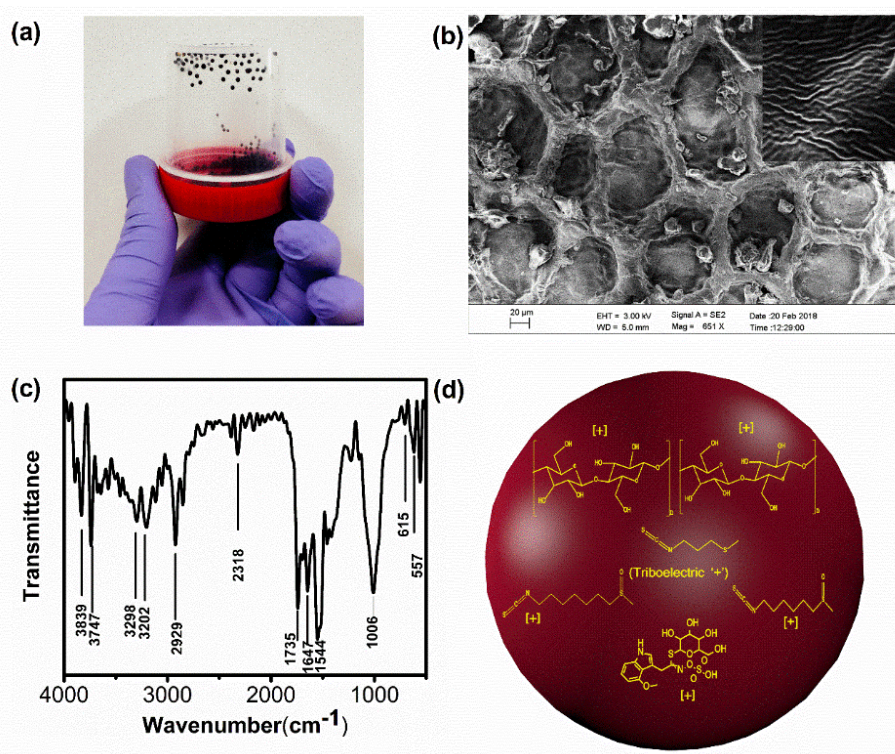


Figure 1 Characterization of mustard seeds (a) Friction-charged mustard seeds in polypropylene box, (b) FESEM image of surface curvature of mustard seed cover (inset shows hierarchical submicron scale undulations), (c) FTIR spectra of mustard seed cover which shows all corresponding signal to $-OH$, $-NH$, $-C=O$, $-NCS$ groups, and (d) Schematic shows the triboelectrically active molecules present on the mustard skin/crust.

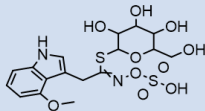
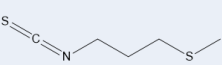
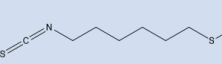
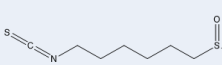
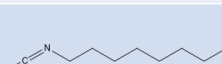
A detailed Fourier-transform infrared spectroscopy (FTIR) analysis of mustard seed skin indicates several peaks that correspond to the amine ($-NH$), hydroxyl ($-OH$), carbonyl ($-C=O$) and isothiocyanate ($-N=C=S$) groups, as shown in figure 1(c) and Table 1. Interestingly, all these functional groups are triboelectric positive in the triboelectric series.^{11, 21} Information about the molecules present on the surface of the mustard seed which has these functional groups were also identified by Liquid chromatography-mass spectrometry (UPLC-QTOF HRMS) and they are presented in figure 1(d). These molecules, namely 4-Methoxyglucobrassicin, 3-(Methylthio)propyl isothiocyanate, 6-methylthiohexyl isothiocyanate, 1-Isothiocyanato-6-(methylsulfonyl)hexane and 7-methyl sulfinyl heptyl isothiocyanate are noted to be in abundance in the mustard

skin, as shown in Table 2. These molecules are indeed rich with hydroxyl, amine, isothiocyanate, and thiols functional groups and therefore effective in triboelectric action.

Table 1 Analysis of functional group present on the mustard surface through FTIR

FTIR of Mustard		
wavenumber	Group	Compound Name
3839	-OH	Cellulose, Glucoisocyanate
3747	-OH	Cellulose, Glucoisocyanate
3298	-NH	Proteins
3202	-NH	Proteins
2929	-CH	Cellulose, Proteins
2318	-NCS	Glucoisocyanate
1735	-CO	Glucoisocyanate

Table 2 Analysis of glucoisocyanate on the mustard seed surface

Molecule name	Chemical structure	Triboelectric group	Mustard seed shell
4-Methoxyglucobrassicin		-OH	Present
3-(Methylthio)propyl isothiocyanate		-NCS	Present
6-methylthiohexyl isothiocyanate		-NCS	Present
1-Isothiocyanato-6-(methylsulfinyl)hexane		- NCS, -C=O	Present
7-methylsulfinylheptyl isothiocyanate		-NCS, -C=o	Present

The starch and cellulose also represent additional constituents of the seed crust representing their major carbohydrate content. Starch is present in seeds as a nourishment source for embryo and cellulose as a cell wall material. Interestingly, cellulose and starch are piezoelectric

polymers, which exhibit piezoelectric charge constants of 27–28 pC/N and 2 pC/N, respectively.^{18, 22} Both contain multiple -OH groups on glucose (as discussed earlier), which build intermolecular and intramolecular hydrogen bonding network on the mustard surface, which is responsible for the formation of spontaneous electric dipoles. Thus, piezoelectricity is generated by displacement of dipoles by external pressure or stress.^{23, 24} Electrostatic charging of starch and cellulose due to inter-particle and particle–wall collisions is so prominent that they are considered as high-risk materials with respect to the dust explosion in their processing industries.^{25, 26} Therefore, the coupling of both piezo and tribo-effects make mustard seeds as an excellent material for Triboelectric Nanogenerator application.²⁷

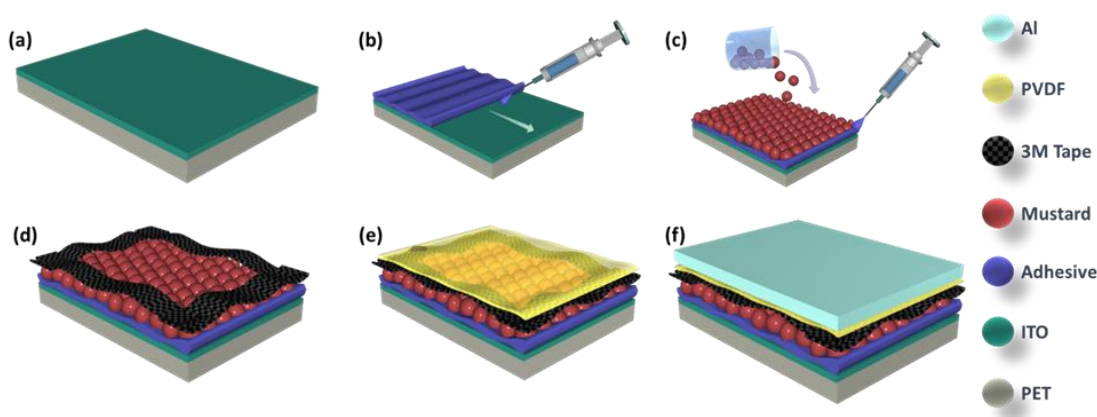


Figure 2 Fabrication of mustard seeds TENG (a) Step-1: Cleaning of ITO coated PET, (b) Step-2: Araldite adhesive coating on the conductive ITO surface, (c) Step-3: Spreading of mustard seeds on the adhesive layer, (d) Step-4: Positioning a separator (3M double-sided tape) on the border of mustard seed layer, (e) and (f) Step-5: Triboelectric layer PVDF nanofibers mat with aluminium electrode fixed on separator

The devices for the mustard seeds (and other seed types as well) were configured by using ITO coated PET as the bottom electrode (Figure 2). The seeds were glued to the electrode with the help of adhesive glue Aradalite. Spacers consisting of double-sided tape (1mm) were bordered on the periphery of the assembled layer of the seeds. Electrospun nanofibres of polyvinylidene fluoride (PVDF) on Al served as the top soft electrode of the device. The electrospun nanofibers offer a natural advantage of about 100 nm scale surface undulations (morphological modulation) which help enhance the frictional effects. When PVDF and the seed crust come into contact, the

seed surface transfers electrons to PVDF due to the higher electron affinity of the PVDF nanofibers as per the triboelectric series.²⁸⁻³⁰

The devices with mustard seeds (or other seeds) facing the nanofibre mat operate in the contact-separation mode. The fabricated devices were sealed with a Kapton tape (Figure 3). A homemade modified sewing machine was used to supply the measured mechanical force with the impact force of 40 N and movement frequency of 25 Hz.³¹ The maximum voltage obtained under open circuit condition is referred to as V_{OC} and the maximum current that can be extracted under the short circuit condition (zero load resistance) is referred to as I_{SC} .

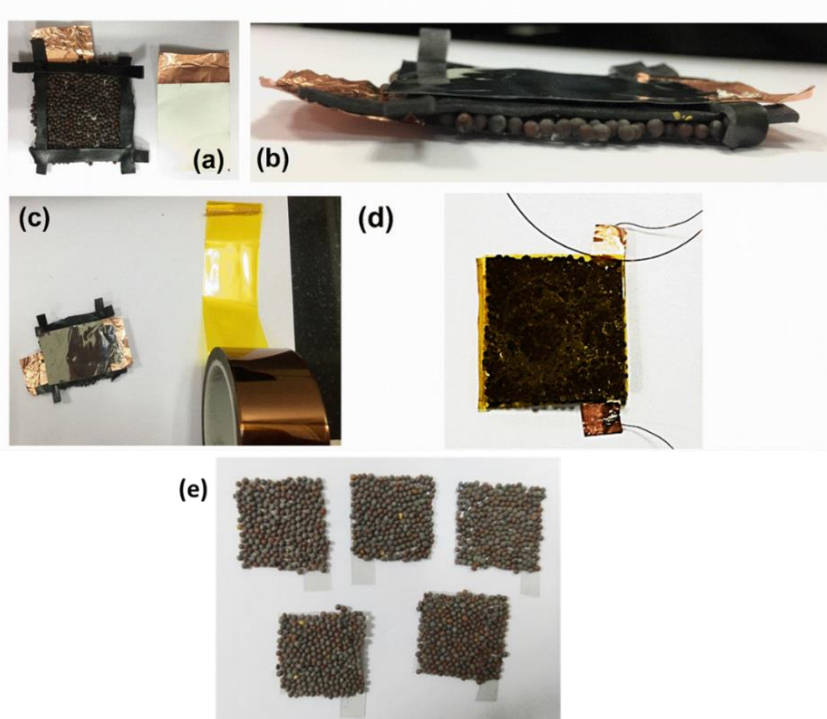


Figure 3 Photographs of S-TENG Device: (a) mustard seeds with separator and PVDF two triboelectric layers (b) contact mode of S-TENG (cross-section view) (c) fabricated S-TENG with sealing Kapton tape (d) Photograph of 3 x 3 cm² mustard S-TENG (e) digital photographic images of the distribution of mustard seeds on electrodes

The voltage and current values under different loads (R_L) reflect the real extractable power ($P = V \times I$). These voltages (across R_L) and currents (in series) measurements were done with Keithley 2450 and 7510 units. Since the voltage and current values vary slightly for each

successive pulse, their average values over 50 impact cycles are stated in the discussions of the powering output. The working mechanism of the S-TENG in the normal mode, compressive mode, and release mode operations is displayed in the graphics in Figure 4(a), 4(b) and 4(c).

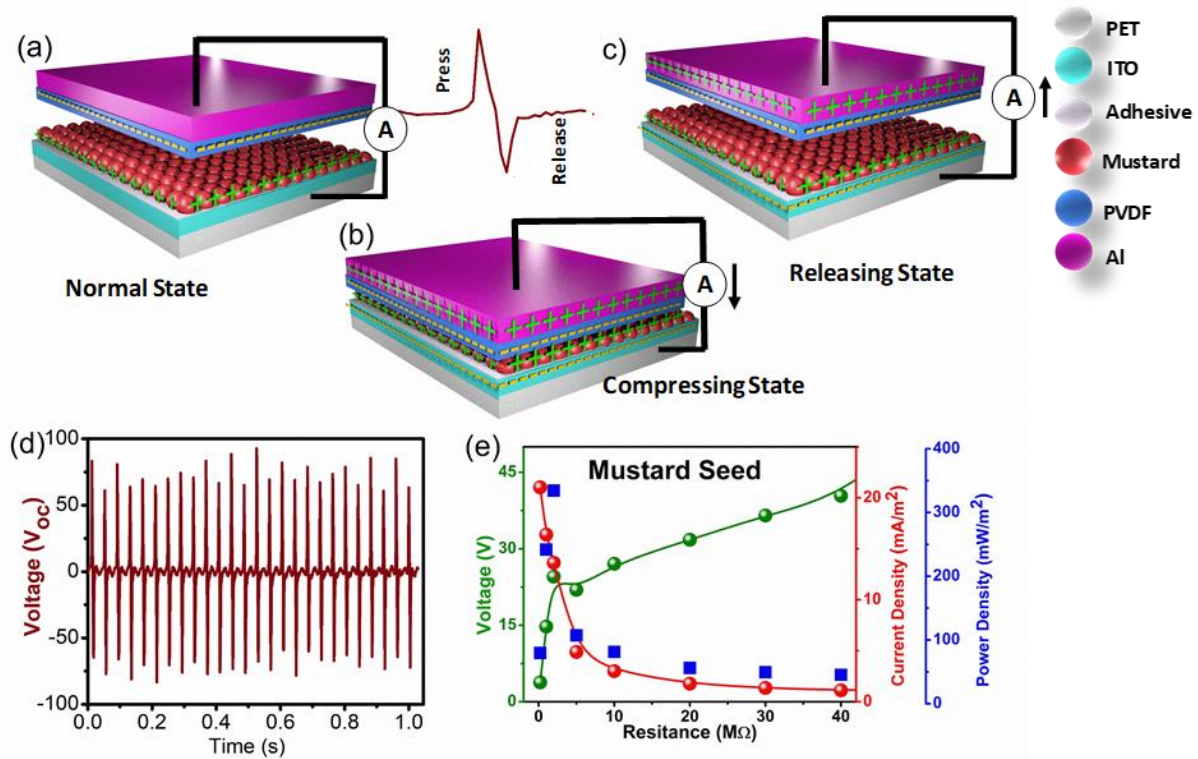


Figure 4 Mechanism of vertical contact mode of Mustard S-TENG (a) Normal state of TENG device, (b) Compression mode of TENG, when current flows from the top electrode to the bottom electrode, giving output voltage, (c) Release state of TENG, current direction gets reversed from the bottom electrode to top electrode, (d) Open circuit voltage of mustard S-TENG, (e) Voltage, current density and power density of mustard S-TENG with range of resistors.

When the two active triboelectric materials come into contact (proximity) with each other under compression state, triboelectric positive (Negative) charges will be induced on the mustard seeds (PVDF surface) through charge transfer and an electric potential difference is created between the top and the bottom electrodes. This drives the electron flow from the bottom electrode to the top electrode, thereby generating a positive signal. When the external impact is released, the two triboelectric materials start to separate from each other, leading to a drop in the electric potential and reverse flow of electrons, thereby producing a negative signal. Repeated contact and separation thus develops an alternating output voltage and current.^{32, 33} The output performance

of S-TENG was further examined as a function of several parameters like load resistance, device contact area, mechanical frequency, and also different seed types.

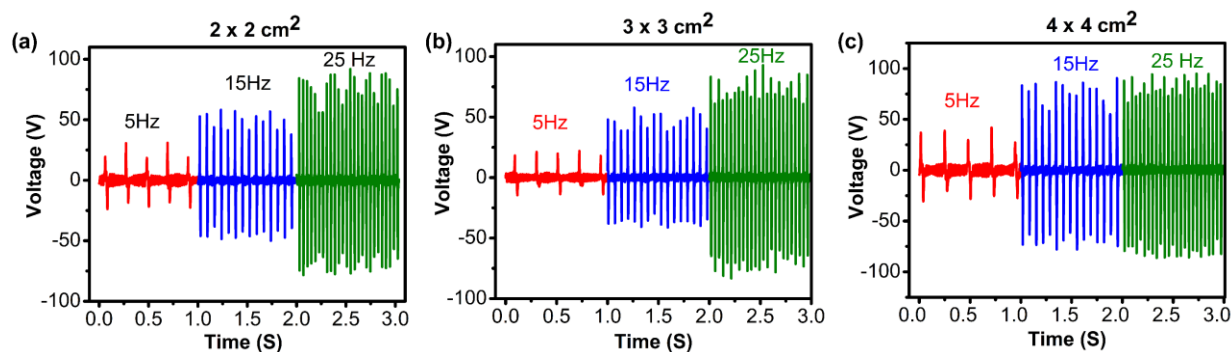


Figure 5 (a), (b) & (c) effect of frequency of impact on open-circuit voltage of $2 \times 2 \text{ cm}^2$, $3 \times 3 \text{ cm}^2$ and $4 \times 4 \text{ cm}^2$ area wise mustard S-TENG devices respectively. The force realized @ 5Hz was 15N @ 15Hz it was 30N and @ 25Hz it was 40N.

For all devices (different seeds), the voltage, current and power density measurements were performed on $3 \times 3 \text{ cm}^2$ area device at 40N force with 25 Hz frequency. An exceptionally high VOC of about 92V (average 84V) was noted for the case of mustard seed device, as shown in Figure 4(d). As seen from the graph of current density and output voltage as a function of load resistance shown in Figure 4(e), a maximum extractable power density 334 mW m^{-2} was obtained for a load resistance of $1 \text{ M}\Omega$ resistance. In the investigation of the effect of area of the device and applied frequency, we found that there was no significant change in the output voltage with the change of the area from 4 cm^2 to 16 cm^2 , but the voltage was noted to increase linearly with frequency (Figure 5). The output performance of the mustard-S-TENG also revealed interesting changes with different bottom electrode materials, in view of the differences in the work functions that drive the separation of charges. Hence, different electrode materials were checked in the interest of realizing better performance. As shown in Figure 6(a), amongst the mustard S-TENGs made using ITO, Cu and Al, the one with both the top and bottom electrodes of aluminium exhibited a better average output peak voltage and current. The output performances of S-TENGs using different seed types (flax and basil) assembled with ITO as the bottom electrode was further investigated (Figure 6(b)). Interestingly, the Flax seeds manifested the average peak voltage of 126 V and maximum power density 324 mW m^{-2} . We further analyzed the basis for the differences in the S-TENG output performance for different seed types

using FTIR analysis. Figure 6(c) compares the FTIR data of the crusts of the basil, mustard and flax seeds.

The stretching band of OH groups of molecular carbohydrate networks dominate in the case of flax seeds. We further analyzed the basis for the differences in the S-TENG output performance for different seed types using FTIR analysis. Figure 6(c) compares the FTIR data of the crusts of the basil, mustard and flax seeds. The stretching band of OH groups of molecular carbohydrate networks dominates in the case of flax seeds, as reflected by the extra broadening of hydroxyl group contribution due to inter and intra-molecular hydrogen bonding among carbohydrate which differs distinctly from the mustard and basil seeds. Flax seeds unveil the highest carbohydrate level as compared to the mustard and basil (Figure 6(d)). On the other hand, the dielectric constant and surface charge polarization values (Figure 6 (e) and (f)) for the mustard seeds are found to be higher than those for the basil and flax seeds. Morphologies in the three cases are also distinctly different as seen from the SEM images given in Figure 7, the mustard seed morphology being intrinsically rougher. Thus, while the output voltage appears to be commensurate with the carbohydrate content, the power output is seen to be also governed by the other two parameters, namely surface morphology and dielectric constant.

In order to also examine the reproducibility of the output performance of S-TENG, ten mustard-based S-TENG devices were tested, and the data are shown in Figure 8(a). This confirms the consistency in the average output voltage. Cycles of compression and release for over 750 cycles on S-TENG were also performed, and it was found that the output performance of S-TENG is quite stable (Figure 8(b)). On the other hand, the performance of basil, mustard and flax seeds based TENG have been analyzed at variable resistance to optimize maximum power transfer (Figure 9(a), (b) and (c)). Having tested the performance of TENGs based in the three seed types we also compared these

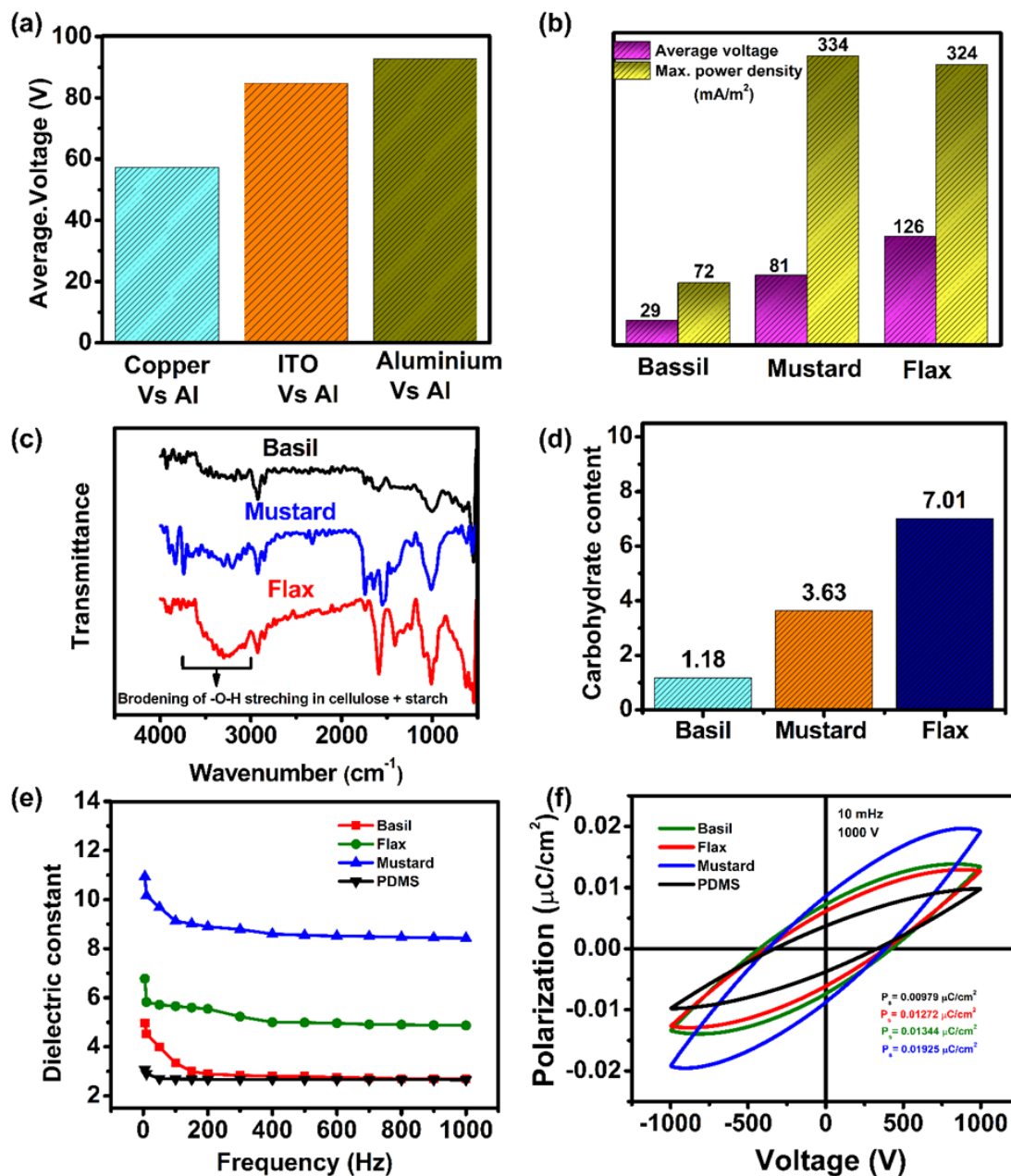


Figure 6 Effect of different electrodes on mustard S-TENG and study with different seeds types: (a) Comparison of the effect of electrode materials: mustard S-TENG on Copper, ITO and Aluminum electrodes, (b) Performance comparison between basil, mustard and flax seed types in S-TENG, (c) FTIR of basil, mustard and flax seeds showing native cellulose associated -O-H stretching modes, (d) Study of carbohydrate content in basil, mustard and flax seeds (mg per 1 gram of sample) (e) Frequency dependence of dielectric constant values of different seeds, and (f) Polarisation- Voltage hysteresis of different seeds.

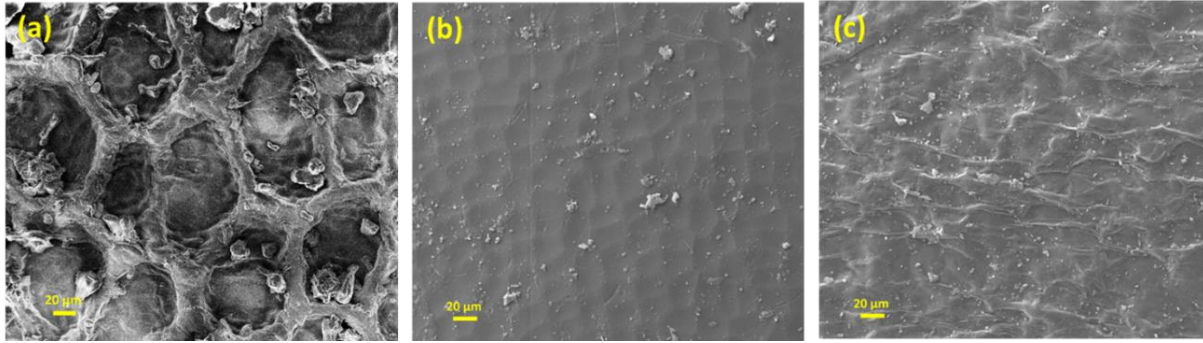


Figure 7 (a), (b) & (c) Scanning electron microscopy (SEM) images of mustard, flax and basil respectively.

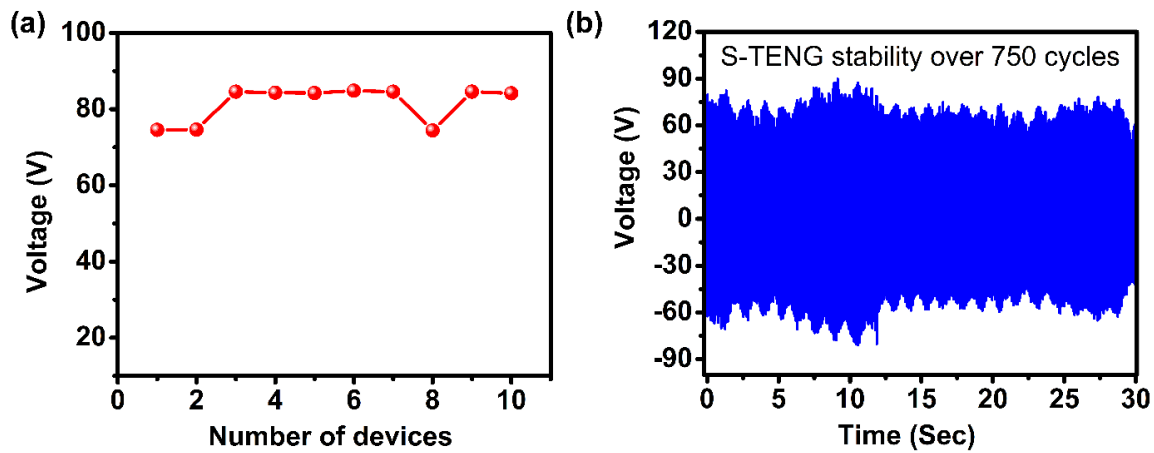


Figure 8 (a) The average output voltage of ten fabricated mustard devices (b) Cycles of compression and release for over 750 cycles on S-TENG

results with some other naturally derived triboelectric mechanical harvesters, and this comparison is presented in Table 3. Our S-TENGs clearly exhibits an impressive power density.

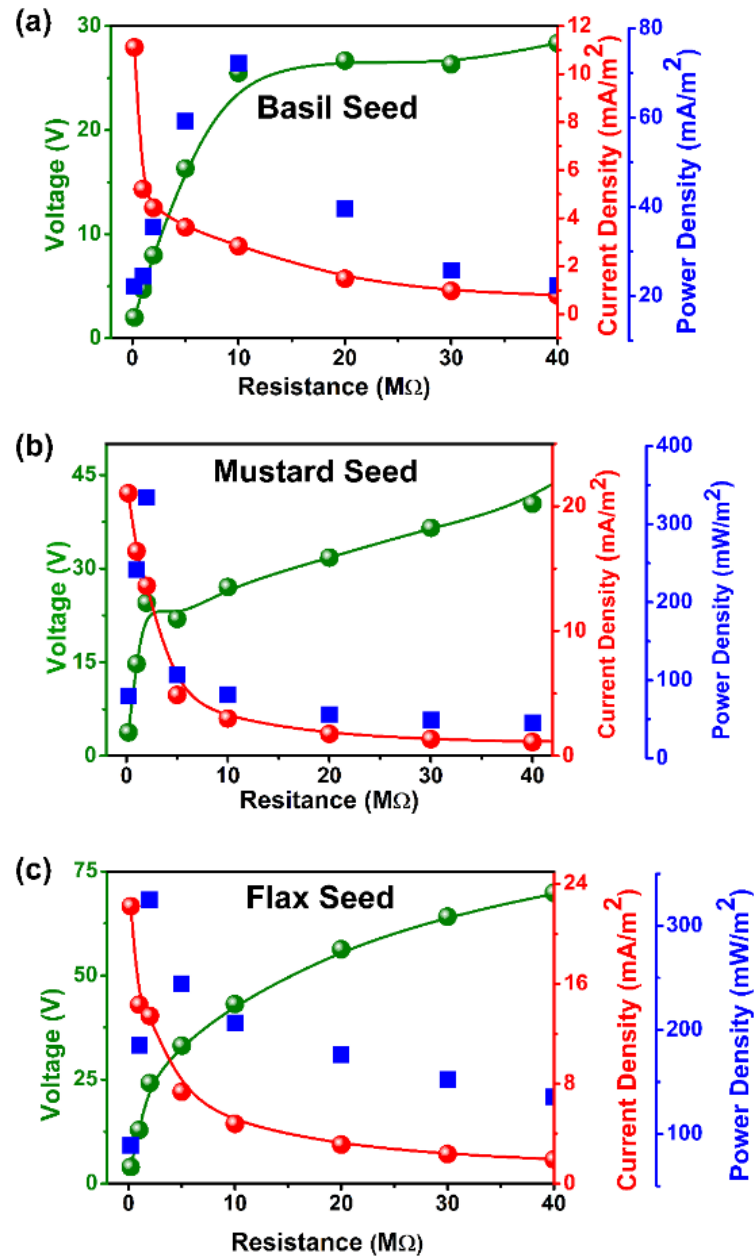


Figure 9 (a), (b) & (c) Study of voltage, current density and power density of different seeds basil, mustard and flax, respectively

Table 3 Comparison table of output performance reported in the literature based on some naturally derived triboelectric mechanical energy harvesters.

Nanogenerator	Voltage(V)	Power Density	Reference
A Leaf-Molded Transparent Triboelectric Nanogenerator	56 Volt (maximum)	-	Nano Energy 2017, 32, 180-186
A robust triboelectric nanogenerator inspired by the natural lotus leaf	1.6 Volt (maximum)	1.5 mW/m ²	Nano Energy 2017, 36, 250-259
Natural Leaf Made Triboelectric Nanogenerator for Harvesting Environmental Mechanical Energy	240 V (maximum)	45 mW/m ²	Advanced Energy Materials 2018, 8 (12), 1703133
Mustard Seed based Nanogenerator (this work)	92 Volt maximum 81 V average	334 mW/m ²	This report

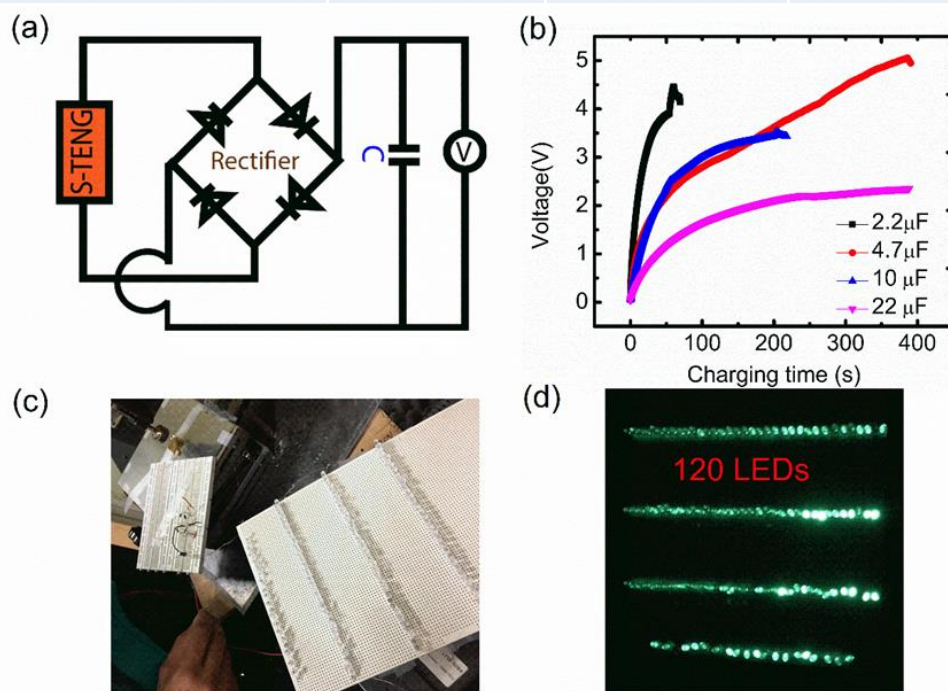


Figure 10 Application of mustard S-TENG. (a) The equivalent circuit diagram for storing the harvested energy in a capacitor from S-TENG, (b) Voltage profile of different capacitors 2.2 μF , 4.7 μF , 10 μF and 22 μF using S-TENG, (c) Experimental set up to light up 120 LEDs, (d) Demonstration of flash-lighting of 120 LEDs with mustard S-TENG

Finally, we demonstrated the practical application of our designed S-TENG by storing the harvested energy in a capacitor. The corresponding equivalent circuit diagram and the charging curves of different capacitors are introduced in Figure 10(a) and 10(b). As seen in Figure 10(b), the voltage across the $2.2\mu\text{F}$ capacitor reaches 4.5V in 60 seconds, while a $4.7\mu\text{F}$ capacitor could be charged to 5.0V in 400 seconds. Among all the tested capacitors, $22\mu\text{F}$ capacitor collected the highest amount of charge while $10\mu\text{F}$ stored the maximum energy in 60 seconds. As a demonstration, Figures 10(c) and 10(d) show an experimental setup to instantaneously flash-power (not a continuous powering) 120 LEDs with the harvested energy stored in the capacitor attached to a bridge circuit. The LEDs were connected across the capacitor in parallel.

The corresponding transferred charges in different capacitors with their respective stored electrical energy were further examined (Figure 11(a) and 11(b)). Transferred charge and the stored energy from S-TENG in 60 seconds is calculated by Q (charge) = C (Capacitance) \times V (Voltage) across Capacitor and E (Storage energy) = $\frac{1}{2} CV^2$. The stored electrical energy by mustard-S-TENG could thus be easily utilized to power smart devices.

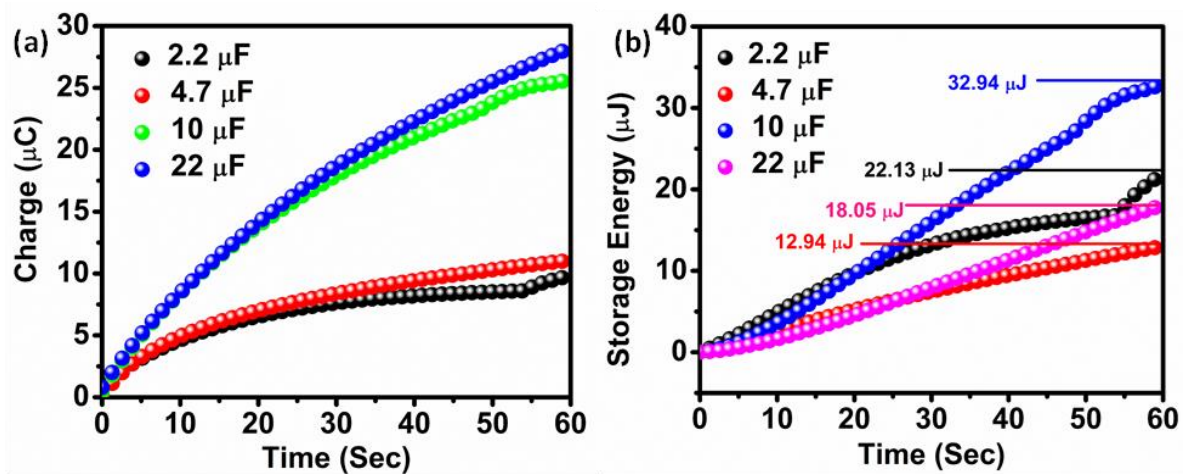


Figure 11 (a) Transferred charge and (b) storage energy into different capacitors in 60 seconds from mustard S-TENG

4. Conclusions:

In conclusion, we have explored a simple TENG device design based on natural seeds in an attempt to move towards a greener approach to mechanical energy harvesting. The design involves a counter-electrode in the form of electrospun PVDF nanofibers, which are triboelectrically negative. While mustard seeds, known for their frictional charging, are examined in more details to elucidate the device features, two other seed types, namely basil and flax, are also examined. The mustard (flax) seed-based TENG is shown to render a very impressive power density of 334 mW/m^2 (324 mW/m^2). The high powering capability of the mustard-based S-TENG is clearly established via flash-lighting (not continuous lighting) of 120 LEDs following 60 seconds charging of the device. The TENG performance of different seed types was noted to collectively depend on the cellulose content in the crust, dielectric constant and surface morphological features.

5. References

1. Wang, Z. L.; Chen, J.; Lin, L., Progress in triboelectric nanogenerators as new energy technology and self-powered sensors. *Energy & Environmental Science* **2015**, *8* (8), 2250-2282.
2. Wu, C.; Wang, A. C.; Ding, W.; Guo, H.; Wang, Z. L., Triboelectric Nanogenerator: A Foundation of the Energy for the New Era. *Advanced Energy Materials* **2019**, *9* (1), 1802906.
3. Wang, Y.; Yang, Y.; Wang, Z. L., Triboelectric nanogenerators as flexible power sources. *npj Flexible Electronics* **2017**, *1* (1), 10.
4. Zi, Y.; Wang, Z. L., Nanogenerators: An emerging technology towards nanoenergy. *APL Materials*, **2017**, *5* (7), 074103.
5. Khan, U.; Kim, S.-W., Triboelectric Nanogenerators for Blue Energy Harvesting. *ACS Nano* **2016**, *10* (7), 6429-6432.
6. Zhang, X.-S.; Han, M.-D.; Meng, B.; Zhang, H.-X., High-performance triboelectric nanogenerators based on large-scale mass-fabrication technologies. *Nano Energy* **2015**, *11*, 304-322.

7. Ghaffarinejad, A.; Hasani, J. Y.; Hinchet, R.; Lu, Y.; Zhang, H.; Karami, A.; Galayko, D.; Kim, S.-W.; Basset, P., A conditioning circuit with exponential enhancement of output energy for triboelectric nanogenerator. *Nano Energy* **2018**, *51*, 173-184.
8. Choi, Y. S.; Jing, Q.; Datta, A.; Boughey, C.; Kar-Narayan, S., A triboelectric generator based on self-poled Nylon-11 nanowires fabricated by gas-flow assisted template wetting. *Energy & Environmental Science* **2017**, *10* (10), 2180-2189.
9. Xu, C.; Zhang, B.; Wang, A. C.; Zou, H.; Liu, G.; Ding, W.; Wu, C.; Ma, M.; Feng, P.; Lin, Z.; Wang, Z. L., Contact-Electrification between Two Identical Materials: Curvature Effect. *ACS Nano* **2019**, *13* (2), 2034-2041.
10. Xu, C.; Zi, Y.; Wang, A. C.; Zou, H.; Dai, Y.; He, X.; Wang, P.; Wang, Y.-C.; Feng, P.; Li, D.; Wang, Z. L., On the Electron-Transfer Mechanism in the Contact-Electrification Effect. *Advanced Materials*, **2018**, *30* (15), 1706790.
11. Wang, S.; Zi, Y.; Zhou, Y. S.; Li, S.; Fan, F.; Lin, L.; Wang, Z. L., Molecular surface functionalization to enhance the power output of triboelectric nanogenerators. *Journal of Materials Chemistry A* **2016**, *4* (10), 3728-3734.
12. Yin, X.; Liu, D.; Zhou, L.; Li, X.; Zhang, C.; Cheng, P.; Guo, H.; Song, W.; Wang, J.; Wang, Z. L., Structure and Dimension Effects on the Performance of Layered Triboelectric Nanogenerators in Contact-Separation Mode. *ACS Nano* **2019**, *13* (1), 698-705.
13. Sun, J.-G.; Yang, T. N.; Kuo, I. S.; Wu, J.-M.; Wang, C.-Y.; Chen, L.-J., A leaf-molded transparent triboelectric nanogenerator for smart multifunctional applications. *Nano Energy* **2017**, *32*, 180-186.
14. Choi, D.; Kim, D. W.; Yoo, D.; Cha, K. J.; La, M.; Kim, D. S., Spontaneous occurrence of liquid-solid contact electrification in nature: Toward a robust triboelectric nanogenerator inspired by the natural lotus leaf. *Nano Energy* **2017**, *36*, 250-259.
15. Jie, Y.; Jia, X.; Zou, J.; Chen, Y.; Wang, N.; Wang, Z. L.; Cao, X., Natural Leaf Made Triboelectric Nanogenerator for Harvesting Environmental Mechanical Energy. *Advanced Energy Materials* **2018**, *8* (12), 1703133.
16. Harmond, J. E., -; Brandenburg, N. R., -; Booster, D. E.; Station, O. S. C. A. E.; Meeting, A. S. o. A. E. *Seed cleaning by electrostatic separation*; [St. Joseph, Mich. : American Society of Agricultural Engineers: 2007-07-13.

17. Davies, D. K., Charge generation on dielectric surfaces. *Journal of Physics D: Applied Physics* **1969**, 2 (11), 1533-1537.
18. Zheng, Q.; Zou, Y.; Zhang, Y.; Liu, Z.; Shi, B.; Wang, X.; Jin, Y.; Ouyang, H.; Li, Z.; Wang, Z. L., Biodegradable triboelectric nanogenerator as a life-time designed implantable power source. *Science Advances* **2016**, 2 (3), e1501478.
19. Fang, H.; Li, Q.; He, W.; Li, J.; Xue, Q.; Xu, C.; Zhang, L.; Ren, T.; Dong, G.; Chan, H. L. W.; Dai, J.; Yan, Q., A high-performance triboelectric nanogenerator for self-powered non-volatile ferroelectric transistor memory. *Nanoscale* **2015**, 7 (41), 17306-17311.
20. Viles, F. J.; Silverman, L., Determination of Starch and Cellulose with Anthrone. *Analytical Chemistry*, **1949**, 21 (8), 950-953.
21. Font, R.; del Río, M.; Fernández-Martínez, J. M.; de Haro-Bailón, A., Use of Near-Infrared Spectroscopy for Screening the Individual and Total Glucosinolate Contents in Indian Mustard Seed (*Brassica juncea* L. Czern. & Coss.). *Journal of Agricultural and Food Chemistry* **2004**, 52 (11), 3563-3569.
22. Gindl, W.; Emsenhuber, G.; Plackner, J.; Konnerth, J.; Keckes, J., Converse Piezoelectric Effect in Cellulose I Revealed by Wide-Angle X-ray Diffraction. *Biomacromolecules* **2010**, 11 (5), 1281-1285.
23. Alam, M. M.; Mandal, D., Native Cellulose Microfiber-Based Hybrid Piezoelectric Generator for Mechanical Energy Harvesting Utility. *ACS Applied Materials & Interfaces* **2016**, 8 (3), 1555-1558.
24. Fukada, E., Piezoelectricity of Wood. *Journal of the Physical Society of Japan* **1955**, 10 (2), 149-154.
25. Yan, X.-Q.; Yu, J.-L., Dust explosion incidents in China. *Process Safety Progress* **2012**, 31 (2), 187-189.
26. Di Benedetto, A.; Russo, P., Thermo-kinetic modelling of dust explosions. *Journal of Loss Prevention in the Process Industries* **2007**, 20 (4), 303-309.
27. Chae, I.; Jeong, C. K.; Ounaies, Z.; Kim, S. H., Review on Electromechanical Coupling Properties of Biomaterials. *ACS Applied Bio Materials* **2018**, 1 (4), 936-953.
28. Wang, Z. L., Triboelectric Nanogenerators as New Energy Technology for Self-Powered Systems and as Active Mechanical and Chemical Sensors. *ACS Nano* **2013**, 7 (11), 9533-9557.

29. Zheng, Y.; Cheng, L.; Yuan, M.; Wang, Z.; Zhang, L.; Qin, Y.; Jing, T., An electrospun nanowire-based triboelectric nanogenerator and its application in a fully self-powered UV detector. *Nanoscale* **2014**, *6* (14), 7842-7846.
30. Wen, R.; Guo, J.; Yu, A.; Zhang, K.; Kou, J.; Zhu, Y.; Zhang, Y.; Li, B.-W.; Zhai, J., Remarkably enhanced triboelectric nanogenerator based on flexible and transparent monolayer titania nanocomposite. *Nano Energy* **2018**, *50*, 140-147.
31. Chaturvedi, S.; Singh, S. K.; Shyam, P.; Shirolkar, M. M.; Krishna, S.; Boomishankar, R.; Ogale, S., Nanoscale LuFeO₃: shape dependent ortho/hexa-phase constitution and nanogenerator application. *Nanoscale* **2018**, *10* (45), 21406-21413.
32. Wang, Z. L., On Maxwell's displacement current for energy and sensors: the origin of nanogenerators. *Materials Today* **2017**, *20* (2), 74-82.
33. Wang, Z. L., Triboelectric nanogenerators as new energy technology and self-powered sensors – Principles, problems and perspectives. *Faraday Discussions* **2014**, *176* (0), 447-458.

Chapter 4

A neutral 1D-coordination polymer $[\text{Rb}(\text{}^i\text{Pr}_2\text{N})]_n$ exhibiting ferroelectric to paraelectric phase transition and mechanical energy harvesting application

Abstract

A new example of diisopropylimido Rubidium complex in a one-dimensional coordination chain structure of formula $[\text{Rb}(\text{}^i\text{Pr}_2\text{N})]_n$ was synthesized and shown to crystallize in non-centrosymmetric crystal symmetry. P-E hysteresis loop measurements gave a good ferroelectric response with a remnant polarization value of $2.7 \mu\text{C}/\text{cm}^2$. Differential scanning calorimetry and dielectric measurement studies revealed the presence of ferroelectric to paraelectric transition at 423 K which is unprecedented among metal-organic ferroelectrics. A representative mechanical energy harvesting device was fabricated by the inclusion (20 weight %) of the compound in the poly(vinyl)alcohol (PVA) matrix which resulted in a sizable open-circuit voltage of 20 V.

Declaration: This is the original work and has not yet been published anywhere.

4.1 Introduction

Ever since the discovery of ferroelectricity in Rochelle salt and KH_2PO_4 in the 1920s,^{1,2} ferroelectrics have become a burgeoning class of functional materials as they find a wide range of applications in ferroelectric random access memories, capacitors, sensors, actuators, electromechanical transducers, photovoltaics and in mechanical energy harvesting devices.³⁻⁵ While the most studied inorganic oxides dominated the commercial market, molecular ferroelectrics were studied to a lesser extent owing to their low polarization values.^{6,7} However, the growing environmental concerns escalated the interest in molecular ferroelectrics as they are lightweight, possess structural tunability, are easily processable and environment-friendly in contrary to the inorganic cousins which involve cumbersome synthesis, high processing temperatures, possess no mechanical flexibility and are highly toxic due to the presence of heavy metal ions such as lead into their composition.⁸⁻¹² In an effort to develop efficient and robust molecular ferroelectric materials, the ionic salt of diisopropyl ammonium bromide was found to exhibit a remarkably high curie temperature value of 426 K and large spontaneous polarization of $23 \mu\text{C}/\text{cm}^2$ which is on par with those observed for certain inorganic oxide materials.¹³

Since then, numerous examples of molecular and ionic salts of organic, hybrid organic-inorganic and charge-separated metal-organic ferroelectric materials containing organoammonium cations have been explored for their polarization properties.¹⁴⁻¹⁶ Spurred by the numerous examples of organic and hybrid organic-inorganic ferroelectric materials based on the diisopropyl ammonium cation,^{17,18} we were interested in utilizing this moiety to synthesize metal-organic assemblies with polar symmetry. Over the years, several groups including that of ours have been interested in the generation of imido complexes of the main group and transition metal ions by the deprotonation of the corresponding amino precursors.¹⁹⁻²¹ The imido anions are isoelectronic to common oxo ions and are known to exhibit rich coordination chemistry. Thus, we set out to explore the deprotonation chemistry of the diisopropylamine in the presence of certain soft Lewis acidic metal ions and generate metal-organic assemblies with non-centrosymmetric structures. Herein, we show the formation of a one-dimensional coordination polymer of a diisopropylimido rubidium complex $[(^i\text{Pr}_2\text{N})\text{Rb}]_n$ (**1**) that crystallizes in the polar space group $P2_1$. Ferroelectric measurements on this

compound gave a remnant polarization of $2.7 \mu\text{C}/\text{cm}^2$. This compound also shows a ferroelectric-paraelectric transition at 423 K which is unprecedented for metal-organic ferroelectric materials, especially for a neutral coordination compound. This compound was further fabricated into a flexible composite thin film in the presence of poly(vinyl)alcohol (PVA) and was tested for mechanical energy harvesting application. An output voltage of 20 V has been recorded under the constant force of 40 N and at an operating frequency of 25 Hz for a representative device composed of 20 weight % of 1 in the PVA matrix. To the best of our knowledge, this is the first report on the formation of a ferroelectric neutral coordination assembly for the diisopropyl anion that has been tested as a potential nanogenerator.

4.2 Experimental Section

General Remarks

Diisopropylamine, hydrogen bromide and rubidium bromide were purchased from Sigma-Aldrich and used without further purification. Poly (vinyl alcohol) was purchased from Alfa Aesar and used as received. NMR spectra were recorded on a Bruker 400 MHz spectrometer (^1H NMR: 400.13 MHz; $^{13}\text{C}\{^1\text{H}\}$ NMR: 100.62 MHz) at room temperature using SiMe_4 (^1H , ^{13}C). Powder X-ray diffraction (PXRD) data were measured on a Bruker D8 Advance diffractometer on the composite films. The PXRD scans were collected in the 2θ range of 5– 50 at 0.3 s per deg. Thermal analysis data was acquired from a PerkinElmer STA6000 thermogravimetric analyzer. Differential Scanning Calorimetry data was obtained from Netzsch FTA JUPITER F1. The melting point was analyzed using an electrothermal melting point apparatus and was uncorrected. Zeiss Ultra Plus FESEM at 5-10 kV was used for SEM imaging.

4.2.1 Synthesis of 1: Diisopropylammonium bromide was obtained by treating diisopropylamine with hydrobromic acid in aqueous solution. The resulting salt was recrystallised from methanol as reported in the literature.¹³ The obtained diisopropyl ammonium bromide salt (1.821 g, 10 mmol) was then reacted with rubidium bromide (1.654 g, 10 mmol) in an equimolar ratio in methanol affording single crystals of 1 after one week. Yield 87%. M.P. 220-240 °C. ^1H NMR (400 MHz, CDCl_3 , ppm) δ 2.95-2.88 (m, 2H), 1.15-1.14 (d, 12H). ^{13}C NMR (101 MHz, CDCl_3 , ppm) δ 47.93, 18.76.

4.2.2 Preparation of 1-PVA composite films:

20 mg of **1** was dispersed into an aqueous solution containing 100 mg of PVA in a vial. The resulting mixture was heated to 70 °C until it converted into a homogeneous solution. This solution was then drop casted onto Al wrapped PET (bottom electrode) and finally cured at 70 °C to achieve a 20 wt. % transparent film of the composite. The composite was then sandwiched between two electrodes by placing ITO coated PET on the composite which served as the top electrode.

4.2.3 Crystallography

Reflections for **1** were acquired on a Bruker Smart Apex Duo diffractometer at various temperatures using Mo K α radiation ($\lambda = 0.71073$ Å). Crystal structures were solved using the direct method and then refined by full-matrix least-squares against F² using SHELXL-2014/7 built in the Apex 3 program.²² All of the nonhydrogen atoms were refined anisotropically while the hydrogen atoms were constrained in geometric positions to their parent atoms.²³

4.2.4 Dielectric, Ferroelectric, and Piezoelectric Measurements.

The dielectric data for **1** was measured using the Novocontrol Dielectric Spectrometer. The powder sample of **1** was compacted in the form of circular discs and aluminium adhesive foils were applied as top and bottom electrodes to the compacted discs for the dielectric measurements. The ferroelectric hysteresis loop was recorded on the compacted pellets of **1** by using a Sawyer-Tower circuit setup. Aluminium adhesive foils were assimilated as the top and bottom electrodes. The polarization measurements were performed by using an aixACCT TF-2000E model hysteresis loop analyzer. Leakage currents were measured dynamically for varied voltage steps in the course of hysteresis loop measurements.

For evaluating the mechanical energy-harvesting performance of the thin-film device of **1**, a home-built vertical impact force setup operating in a periodic compression and release function coupled with an oscilloscope was used. The fabricated devices were subjected to an impact force of 40 N with a tapping frequency of 25 Hz on an active area of 2×2 cm². The output voltage measurement was recorded on a Keithley DMM7510 7.5 multimeter.

4.3 Results and Discussions

Compound **1** was isolated as single crystals from the methanolic solution by the reaction of diisopropyl ammonium bromide with rubidium bromide. The molecular structure of the compound was determined by single-crystal X-ray diffraction analysis at 100 K (Table 1). It was found to crystallize in the polar space group $P2_1$ (Point group: C_2) which belongs to one of the 10 polar point groups that are suitable for ferroelectricity.

Table 1 Details of Crystallographic data collection of **1**

Compound	1 (100 K)	1 (298 K)
Chemical formula	C ₆ H ₁₄ N Rb	C ₆ H ₁₄ N Rb
Formula weight	185.65	185.65
Temperature	100(2)K	298(2) K
Crystal system	Monoclinic	Monoclinic
Space group	$P2_1$	$P2_1$
a(Å): α (°)	7.7436(18); 90	7.8607(14); 90
b(Å): β (°)	8.0057(18); 116.299(8)	8.1070(15); 116.277(6)
c (Å): γ (°)	7.8255(19); 90	7.8941(17); 90
V(Å ³); Z	434.91(18); 2	451.08(15); 2
P(calc.) g cm ⁻³	1.418	1.367
μ (Mo K α)mm ⁻¹	5.609	5.408
2 θ _{max} (°)	56	56
R (int)	0.0950	0.1051
Completeness to θ	100.0	99.7
Data/param.	2180/ 78	2220/77
GOF	1.036	1.075
R1[F>4 σ (F)]	0.0520	0.0657
wR2 (all data)	0.0797	0.1423
max. peak/hole (e.Å ⁻³)	0.561/ -0.839	0.684/-0.843

The asymmetric unit of compound **1** comprises of one rubidium atom bonded to the N atom of one diisopropyl unit. Each imido nitrogen atom is bonded to two Rb atoms and each Rb is connected to two ligand N imido sites giving rise to a one-dimensional *zig-zag* chain structure that runs along the polar b-axis. The packing structure of **1** shows that the 1D-chains in the adjacent layers are superimposing on top of each other. The two unique Rb-N distances in **1** are found to be 3.308 (6) and 3.311 (6) Å and are comparable to those found in earlier reported imido-Rb complexes (Figure 1a and 1b).²⁴

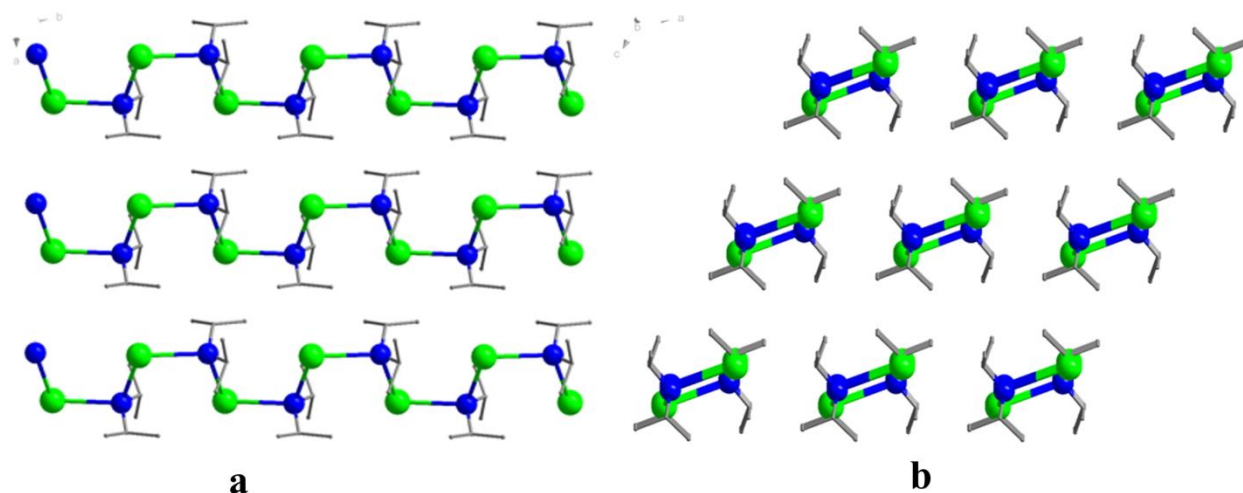


Figure 1 Packing diagram of **1** along (a) *c* axis and (b) *b* axis

The bulk phase purity of the compound was established by performing Powder X-ray Diffraction Analysis (PXRD) at room temperature. The well-matched patterned peaks of the bulk sample with the simulated peak profiles from the single-crystal X-ray diffraction data confirms the phase purity of obtained material (Figure 2a). Moreover, the compound was seen to exhibit thermal stability up to 520 K as revealed by thermogravimetric analysis (Figure 2b). As the ferroelectric compounds undergo temperature promoted transitions, we recorded differential scanning calorimetry data of **1** to analyse the presence of any phase transition. As seen in Figure 2c, **1** undergoes a reversible phase transition at 423 K.

The macroscopic polarization reversal was carried out by performing Polarization vs Electric field (P-E) measurements utilizing the Sawyer-Tower Circuit. For the measurements, the powder sample of **1** was compressed in the form of a pellet and the aluminium adhesive tapes acting as the top and the bottom electrodes. The P-E measurements displayed a rectangular hysteresis loop at an operating frequency of 0.01 Hz with a remnant polarization value of $2.7 \mu\text{C}/\text{cm}^2$ at a relatively low coercive field of 0.26 kV/cm. These values are comparable well with several recently reported hybrid ferroelectric compounds.²⁵⁻²⁸ The leakage current density plot of **1** measured along the P-E loop gave peaks associated with the coercive fields with low-leakage currents (of the order of 10^{-6} A), which supports the ferroelectric nature of the obtained loop (Figure 2d). To further probe the ferroelectric nature of **1**, a point charge model based polarization calculation was performed. For

these calculations, the unit cell of **1** is selected and an assumption is made that the positive charge and the negative charges of the molecules are located on the Rb and N atom, respectively. The shift in atomic coordinates between the positive and negative dipoles per unit cell volume of the crystal as given in Equation 1 gives rise to the polarization of the system. The computed P_s value of $5.9 \mu\text{C}/\text{cm}^2$ is closely comparable with the experimentally observed polarization of $2.7 \mu\text{C}/\text{cm}^2$ obtained from the Sawyer-Tower circuit measurements. The reduction in the experimental P_s value in comparison with the calculated P_s based on the point charge model can be attributed to the polycrystalline nature of the studied sample (in the form of the compacted disc) where the polar domains are randomly oriented resulting in a slightly reduced polarization value.

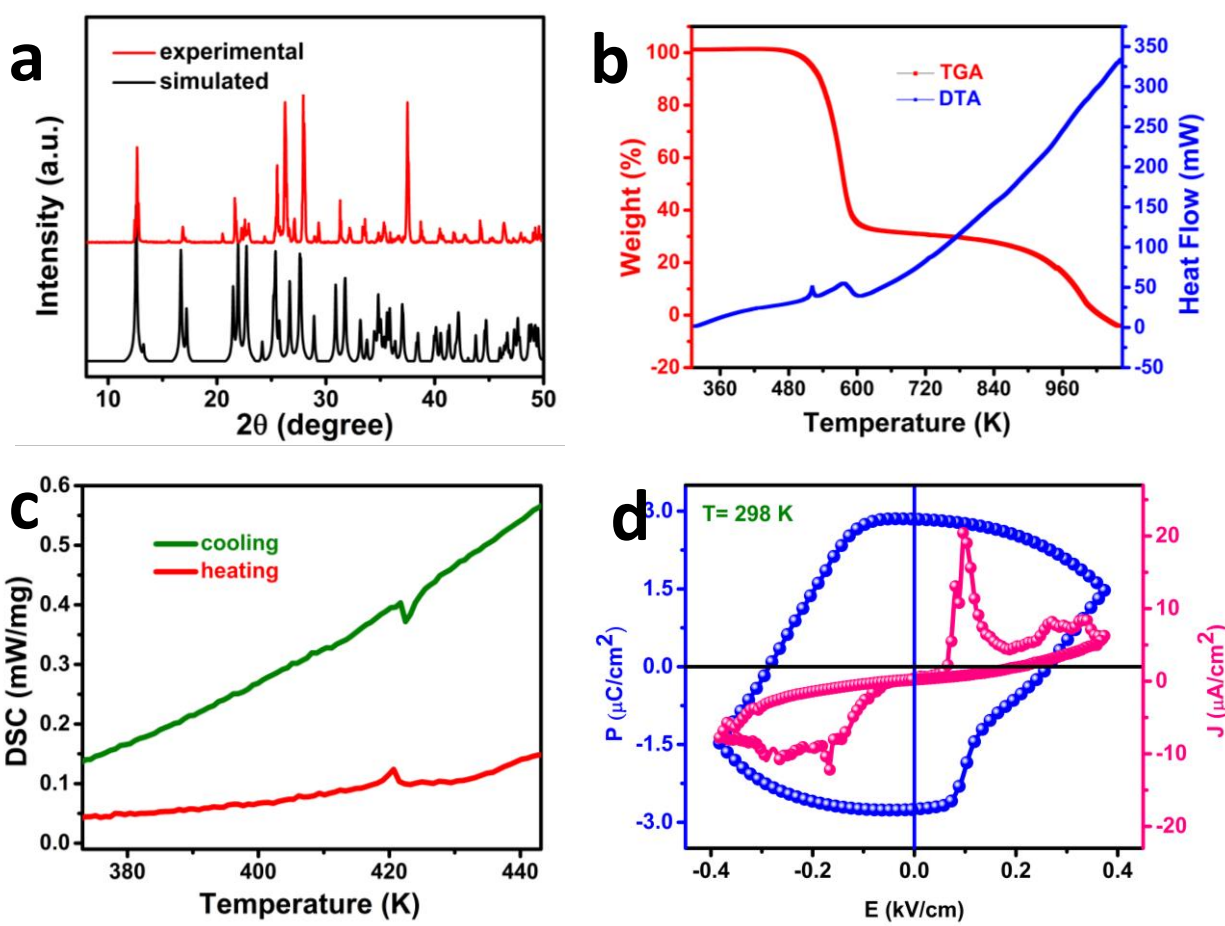


Figure 2 (a) PXRD data (b) TGA-DTA (c) DSC data and (d) Ferroelectric hysteresis loop along with its corresponding leakage current density plot of **1**.

Table 2 Atom coordinates selected for the polarization calculations

Atoms	Centroid Coordinates
Rb	(0.5, 0.446, 0.5)
N	(0.5, 0.345, 0.5)

$$\mathbf{P} = \lim 1/V \sum q_i \mathbf{r}_i \quad \dots\dots\dots (1)$$

$$\begin{aligned}
 &= [(\mathbf{q}_e(\text{Rb})\mathbf{r}(\text{Rb}) + \mathbf{q}_e(\text{N})\mathbf{r}(\text{N}))]/V \\
 &= [(\mathbf{q}_e \times \mathbf{0.446}) + (-\mathbf{q}_e \times \mathbf{0.345})] \times 2 \times \mathbf{b}_1 / V \\
 &= [0.101 \times 1.6 \times 10^{-19} \times 2 \times 8.0057 \times 10^{-10} \text{ Cm}] / (434.91 \times 10^{-30} \text{ m}^3) \\
 &= 0.0594 \text{ Cm}^{-2}
 \end{aligned}$$

$$\mathbf{P} = 5.9 \mu\text{Ccm}^{-2}$$

Where values of r are the coordinates of the centroid of the Rb and N atoms in the unit cell, q_e is the charge on the electron, b_1 is the cell-length along the b-axis, V is the unit-cell volume.

The real part of the dielectric permittivity was measured on the compressed disc of **1** as a function of temperature and frequency. As seen in Figure 3a, the temperature-dependent dielectric constant displayed the presence of anomaly peak centred at 423 K which is in good agreement with the heat-anomaly peaks from the DSC data. This indicates the presence of a structural phase transition in **1** at this temperature from the ferroelectric to paraelectric phase. However, the structural details pertaining to the paraelectric phase could not be extracted from single-crystal X-ray data as the crystals melt into a viscous state at the goniometer tip. This is suggestive of the existence of some sort of liquid crystalline state in the paraelectric phase (which needs further exploration). The maximum ϵ' value was found to be 150 (423) at 1 Hz, as observed from the frequency-dependent dielectric constant measurements (Figure 3b). Also, the noticeable increase in the dielectric constant value with a decrease in the frequency stems from the contribution of all four polarization mechanisms.

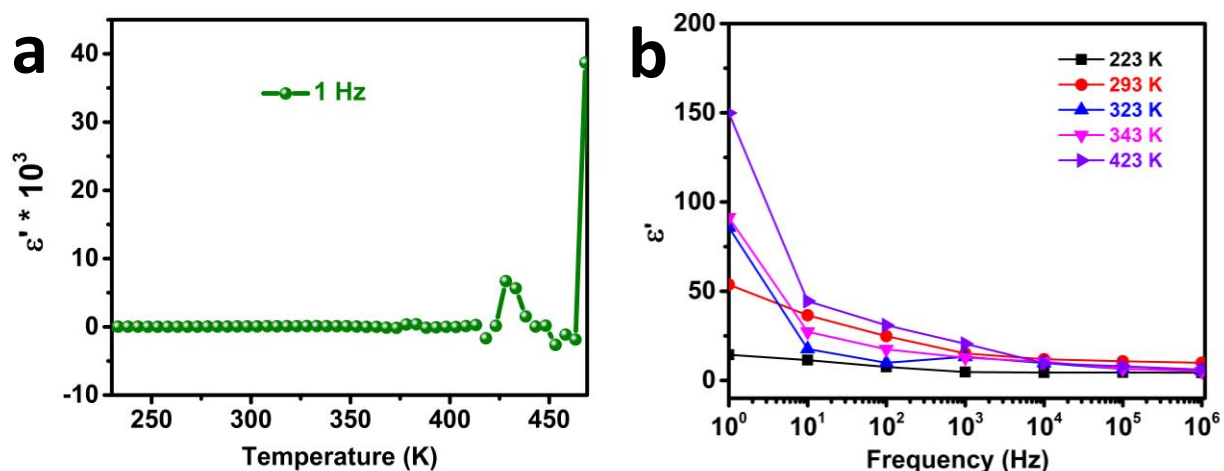


Figure 3 Real part of the complex dielectric constant (a) as a function of temperature measured at 1 Hz. (b) as a function of frequency measured at different temperatures.

The potential of the 1D coordination polymer of **1** as flexible energy harvester was further probed by fabricating mechanical energy harvesting device in the presence of a suitable polymer. Appropriate quantity of **1** was dispersed into an aqueous solution containing polyvinyl alcohol (MW- 85000-124000) to prepare a composite solution of 20 wt. % in the composition. The resulting mixture was then heated at 70°C to obtain a homogeneous solution of the composite.

The prepared solution was then drop cast onto an Al wrapped PET film and cured at 70°C to yield a transparent film of **1**-PVA (Figure 4a). ITO coated PET was then placed on top of the composite film as the top electrode. The device connections were established by soldering the copper wires onto the copper tapes placed on the top and bottom electrodes. Finally, the whole device was thoroughly covered with the Kapton tape to attain electrical isolation and to increase the device mechanical robustness.

The formulated composite demonstrated excellent mechanical flexibility as presented in Figure 4b. The SEM image displays a fibrous network of compound **1** dispersed homogeneously throughout the composite film (Figure 4c). This indicated that the 1D-chain structure of **1** is retained within the polymer composite framework. Moreover, the powder diffraction data

determines the formation of a crystalline composite film where 1D crystallites of **1** are oriented along multiple directions (Figure 4d).

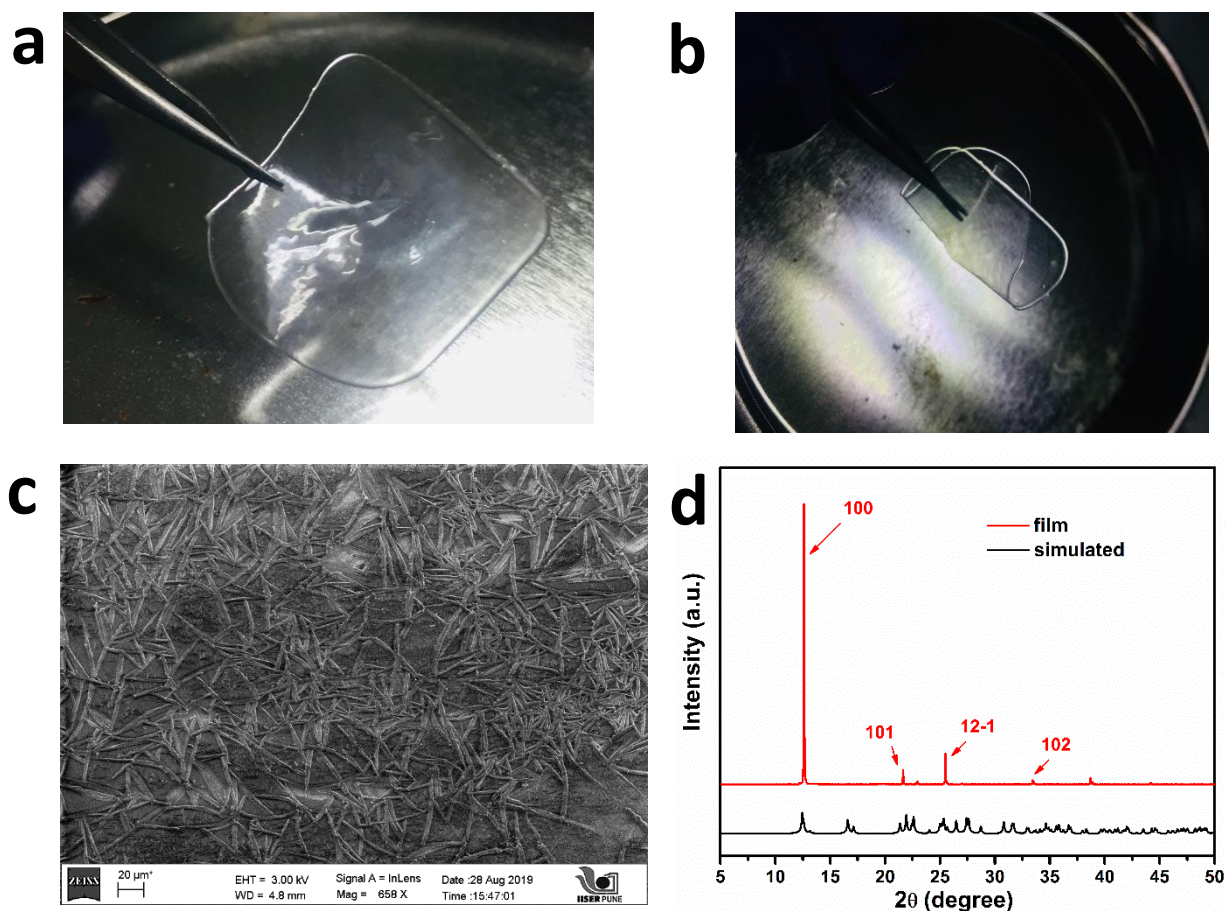


Figure 4 (a) Photograph of the as-prepared transparent composite film of **1** (b) Flexible film exhibiting rolling operation (c) SEM image displaying the homogeneous distribution of the compound in the polymer (d) PXRD data on the as-prepared composite film.

The preliminary output performance of the device was evaluated by subjecting it to a force of 40 N with a frequency of 25 Hz. The active area of the device was $2 \times 2 \text{ cm}^2$. An output voltage of 20 V was obtained from the as-fabricated device (Figure 5). The obtained voltage for the **1**-PVA device with 15 wt.% of **1** is comparable to those recorded for the known examples of the polymer composites of organic-inorganic hybrids.^{29,30} Different wt.% composites devices of **1** along with their device performance are checked for Nanogenerator performance.

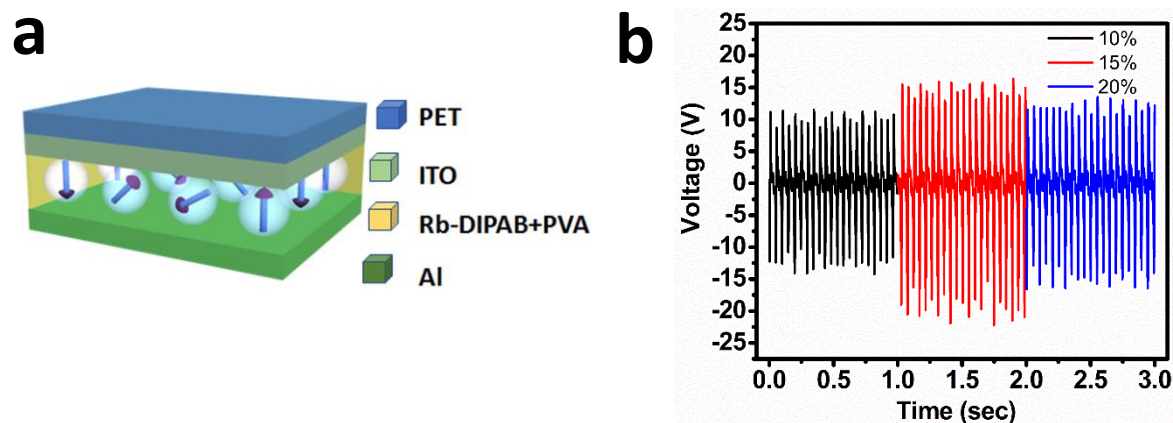


Figure 5 (a) Schematic diagram depicting the fabrication of the device (b) Output voltage measurement performed on different wt.% of 1-PVA.

4.4 Conclusion

In conclusion, we have explored a newly designed neutral one-dimensional coordination polymer for diisopropylimido anion and Rb cation and explored their ferroelectric behaviour and mechanical energy harvesting activity. The compound was found to crystallize in polar point group and the compressed pellet of it exhibited a remnant polarization value of $2.7 \mu\text{C}/\text{cm}^2$. Moreover, its applicability towards energy harvesting device was probed by the preparation of a flexible device by the inclusion of **1** into a PVA polymer composite. A preliminary device testing showed an output voltage of 20 V at an impact force of 40 N at 25 Hz. We are now working forward towards evaluating the device performance with varying concentrations, frequencies and area and deeply analysing them. Also, a practical demonstration of the 1D neutral coordination polymer towards LED lightning and capacitor charging will be explored as well.

4.5 References

1. Valasek, J., Piezo-Electric and Allied Phenomena in Rochelle Salt. *Phys. Rev.* **1921**, *17*, 475-481.
2. Lines, M. E.; Glass, A. M. Principles and Applications of Ferroelectrics and Related Materials; Clarendon Press: Oxford, U.K., 1977.
3. Scott, J. F. Applications of Modern Ferroelectrics. *Science* **2007**, *315*, 954–959.
4. Ye, Z.-G., Handbook of Advanced Dielectric, Piezoelectric and Ferroelectric Materials: Synthesis, Properties and Applications; Elsevier, 2008.

5. Ishiwara, H. Ferroelectric Random Access Memories. *J.Nanosci. Nanotechnol.* **2012**, *12*, 7619–7627.
6. Damjanovic, D., Ferroelectric, dielectric and piezoelectric properties of ferroelectric thin films and ceramics. *Reports on Progress in Physics* **1998**, *61*, 1267-1324.
7. Haertling, G. H., Ferroelectric Ceramics: History and Technology. *J. Am. Ceram. Soc.* **1999**, *82*, 797-818.
8. Scott, J. F. Applications of Modern Ferroelectrics. *Science* **2007**, *315*, 954–959.
9. Scott, J. F.; Paz de Araujo, C. A., Ferroelectric Memories. *Science* **1989**, *246*, 1400-1405.
10. Tayi, A. S.; Shveyd, A. K.; Sue, A. C. H.; Szarko, J. M.; Rolczynski, B. S.; Cao, D.; Kennedy, T. J.; Sarjeant, A. A.; Stern, C. L.; Paxton, W. F.; Wu, W.; Dey, S. K.; Fahrenbach, A. C.; Guest, J. R.; Mohseni, H.; Chen, L. X.; Wang, K. L.; Stoddart, J. F.; Stupp, S. I., Room-temperature ferroelectricity in supramolecular networks of charge-transfer complexes. *Nature* **2012**, *488*, 485-489.
11. Horiuchi, S.; Tokunaga, Y.; Giovannetti, G.; Picozzi, S.; Itoh, H.; Shimano, R.; Kumai, R.; Tokura, Y., Above-room-temperature ferroelectricity in a single-component molecular crystal. *Nature* **2010**, *463*, 789-792.
12. Xu, G.-C.; Zhang, W.; Ma, X.-M.; Chen, Y.-H.; Zhang, L.; Cai, H.-L.; Wang, Z.-M.; Xiong, R.-G.; Gao, S., Coexistence of Magnetic and Electric Orderings in the Metal–Formate Frameworks of [NH₄] [M(HCOO)₃]. *J. Am. Chem. Soc.* **2011**, *133*, 14948-14951.
13. Fu, D.-W.; Cai, H.-L.; Liu, Y.; Ye, Q.; Zhang, W.; Zhang, Y.; Chen, X.-Y.; Giovannetti, G.; Capone, M.; Li, J.; Xiong, R.-G., Diisopropylammonium Bromide Is a High-Temperature Molecular Ferroelectric Crystal. *Science* **2013**, *339*, 425-428.
14. Samantaray, R.; Clark, R. J.; Choi, E. S.; Zhou, H.; Dalal, N. S., M_{3-x}(NH₄)_xCrO₈ (M = Na, K, Rb, Cs): A New Family of Cr⁵⁺-Based Magnetic Ferroelectrics. *J. Am. Chem. Soc.* **2011**, *133*, 3792-3795.
15. Stroppa, A.; Barone, P.; Jain, P.; Perez-Mato, J. M.; Picozzi, S., Hybrid Improper Ferroelectricity in a Multiferroic and Magnetoelectric Metal-Organic Framework. *Adv. Mater.* **2013**, *25*, 2284-2290.
16. Tian, Y.; Shen, S.; Cong, J.; Yan, L.; Wang, S.; Sun, Y., Observation of Resonant Quantum Magnetoelectric Effect in a Multiferroic Metal-Organic Framework. *J. Am. Chem. Soc.* **2016**, *138*, 782-785.

17. Jiang, C.; Zhong, N.; Luo, C.; Lin, H.; Zhang, Y.; Peng, H.; Duan, C.-G., (Diisopropylammonium)₂MnBr₄: a multifunctional ferroelectric with efficient green-emission and excellent gas sensing properties. *Chem. Commun.* **2017**, 53, 5954-5957.
18. Fu, D. W.; Zhang, W.; Cai, H. L.; Ge, J. Z.; Zhang, Y.; Xiong, R. G., Diisopropylammonium Chloride: A Ferroelectric Organic Salt with a High Phase Transition Temperature and Practical Utilization Level of Spontaneous Polarization. *Adv. Mater.* **2011**, 23, 5658-5662.
19. Steiner, A.; Zacchini, S.; Richards, P. I., From neutral iminophosphoranes to multianionic phosphazenes. The coordination chemistry of imino–aza-P(V) ligands. *Coord. Chem. Rev.* **2002**, 227, 193-216.
20. Boomishankar, R.; Srivastava, A. K., Functional metal-organic molecules and materials derived from rigid and flexible P-N scaffolds. *Phosphorus, Sulfur, and Silicon and the Related Elements* **2016**, 191, 618-623.
21. Gupta, A. K.; Reddy, S. A. D.; Boomishankar, R., Facile Formation of Stable Tris(imido)phosphate Trianions as Their Tri- and Hexanuclear Pd(II) Complexes in Protic Solvents. *Inorg. Chem.* **2013**, 52, 7608-7614.
22. Sheldrick, G. M. A short history of SHELX. *Acta Crystallogr., Sect. A: Found. Crystallogr.* **2008**, 64, 112–122.
23. Spek, A. Structure validation in chemical crystallography. *Acta Crystallogr., Sect. D: Biol. Crystallogr.* **2009**, 65, 148–155.
24. Meinholz, M. M.; Stalke, D., Monoanionic N,P,S-Janus Head Tripods in s-Block Metal Coordination. *Eur. J. Inorg. Chem.* **2011**, 2011, 4578-4584.
25. Ye, H.-Y.; Ge, J.-Z.; Tang, Y.-Y.; Li, P.-F.; Zhang, Y.; You, Y.-M.; Xiong, R.-G. Molecular Ferroelectric with Most Equivalent Polarization Directions Induced by the Plastic Phase Transition. *J. Am. Chem. Soc.* **2016**, 138, 13175–13178.
26. Pan, Q.; Liu, Z. B.; Zhang, H. Y.; Zhang, W. Y.; Tang, Y. Y.; You, Y. M.; Li, P. F.; Liao, W. Q.; Shi, P. P.; Ma, R. W.; Wei, R. Y.; Xiong, R. G. A Molecular Polycrystalline Ferroelectric with Record-High Phase Transition Temperature. *Adv. Mater.* **2017**, 29, 1700831.
27. You, Y.-M.; Tang, Y.-Y.; Li, P.-F.; Zhang, H.-Y.; Zhang, W.-Y.; Zhang, Y.; Ye, H.-Y.; Nakamura, T.; Xiong, R.-G. Quinuclidinium salt ferroelectric thin-film with duodecupole rotational polarization-directions. *Nat. Commun.* **2017**, 8, 14934.

28. Zhang, W.-Y.; Tang, Y.-Y.; Li, P.-F.; Shi, P.-P.; Liao, W.-Q.; Fu, D.-W.; Ye, H.-Y.; Zhang, Y.; Xiong, R.-G. Precise Molecular Design of High- T_c 3D Organic–Inorganic Perovskite Ferroelectric: [MeHdabco]RbI₃ (MeHdabco = N-Methyl-1,4-diazoniabicyclo [2.2.2] octane). *J. Am. Chem. Soc.* **2017**, *139*, 10897–10902.
29. Ding, R.; Liu, H.; Zhang, X.; Xiao, J.; Kishor, R.; Sun, H.; Zhu, B.; Chen, G.; Gao, F.; Feng, X.; Chen, J.; Chen, X.; Sun, X.; Zheng, Y., Flexible Piezoelectric Nanocomposite Generators Based on Formamidinium Lead Halide Perovskite Nanoparticles. *Adv. Funct. Mater.* **2016**, *26*, 7708-7716.
30. Pandey, R.; Sb, G.; Grover, S.; Singh, S. K.; Kadam, A.; Ogale, S.; Waghmare, U. V.; Rao, V. R.; Kabra, D., Microscopic Origin of Piezoelectricity in Lead-Free Halide Perovskite: Application in Nanogenerator Design. *ACS Energy Lett.* **2019**, *4*, 1004-1011.

Chapter 5

Mechanical energy harvesting using different materials of emergent interest

Abstract

In this chapter, we present results on several specially engineered materials for NG and TENG applications.

One such study involved the use of a multi-ferroic LuFeO_3 in nanoparticle and nanofibers forms with differing hexagonal (h) phase and orthorhombic (o) phase contributions. Lutetium orthoferrite (LuFeO_3) is an oxide material of emerging interest in the field of multiferroicity. By fabricating flexible piezoelectric nanogenerator devices based on LuFeO_3 nanoparticles (NPs) and nanofibers, and their composite with PDMS we obtained open-circuit voltage of ~ 3.4 V and 6.4V, respectively, depending on the phase constitution.

In another study, we fabricated triboelectric nanogenerators (TENGs) with MoS_2 , hBN, and MoS_2 -hBN nanocomposite. The output voltage of TENG is related to the corresponding work function. A triboelectric nanogenerator device containing biphasic MoS_2 -hBN composite film as an electron acceptor was seen to exhibit more than two-fold (six-fold) enhancement in peak-to-peak output voltage as compared to the pristine MoS_2 (hBN) film, which correlates well with work function analyses based on electric force microscopy (EFM).

Finally, we also prepared a triboelectric nanogenerator (TENG) based touch-sensing device comprising of bulk MAX film and microfiber paper which showed a very high peak-to-peak open-circuit output voltage of ~ 80 V for applied force of about 15N.

Note: The author's contribution is all these three studies was to fabricate, test and analyse the NG and TENG devices, while the credit for the choice of materials systems, synthesis of their specific forms, and the materials characterization and analysis goes to Dr. Smita Chaturvedi (LuFeO_3), Ms. Swati Parmar (MoS_2 /h-BN) and Dr. Abhijit Biswas (MAX).

The following paper has been published based on the work documented in this chapter.

Chaturvedi, S.; **Singh, S. K.**; Shyam, P.; Shirolkar, M. M.; Krishna, S.; Boomishankar, R.; Ogale, S., Nanoscale LuFeO_3 : shape-dependent ortho/hexa-phase constitution and nanogenerator application. *Nanoscale* 2018, 10 (45), 21406-21413. (equal contribution) This chapter is reproduced from our above-mentioned article already published in *Nanoscale* after acknowledging Royal Society of Chemistry.

Parmar, S.; Biswas, A.; Kumar Singh, S.; Ray, B.; Parmar, S.; Gosavi, S.; Sathe, V.; Janay Choudhary, R.; Datar, S.; Ogale, S., Coexisting 1T/2H polymorphs, reentrant resistivity behavior, and charge distribution in MoS_2 -hBN 2D/2D composite thin films. *Physical Review Materials* 2019, 3 (7), 074007. This chapter is reproduced from our above mentioned article already published in *Nanoscale* after acknowledging American Physical Society.

5.1 Piezoelectric Nanogenerator based on LFO-PDMS composite film

Various types of PNGs based on non-centrosymmetric oxides such as ZnO, PZT, BaTiO₃, and BiFeO₃ have been reported for energy harvesting applications. Ferroelectric perovskites have attracted attention for NG applications because of the availability of some unique non-centrosymmetric structural forms, high polarization, and piezoelectric coefficient. Multiferroicity, which deals with the interesting condition of coupled ferroic (magnetic, electric, elastic) order parameters in a single material, has been the subject of intense scientific scrutiny for many years, in view of its great projected potential for multiple applications.¹⁻⁴ Since thin films are the vehicles for most modern device architectures, studies on multiferroic systems are primarily performed on substrate-supported film samples.⁵⁻¹¹ The substrate also naturally offers “interface strain” as an extra parameter to manipulate and possibly enhance the coupling of order parameters.^{10, 12} In nanomaterials, the surface-relaxation-induced strain field influences the emerging phenomena related to physical properties in interesting ways such as enhancement, the coupling of different orders etc., and thus serves as an interesting geometric parameter to control the physical properties via manipulation of nanomaterial size and shape.

Lutetium orthoferrite (LuFeO₃) is an oxide material of emerging interest in the field of multiferroicity. It has been studied by many groups in its hexagonal phase-stabilized in a thin film form¹³⁻²⁰ and in the orthorhombic (o) form.²¹⁻²⁴ Orthorhombic (o) and hexagonal (h) structures are significantly dissimilar in terms of the symmetry of the lattice as well as the symmetry of the environment of the individual cations (Lu and Fe).²⁵ This difference in structural symmetry contributes to interesting changes in the physical properties. The crystal structure of o-LFO is distorted perovskite-type and is described by the Pnma space group. In this structure, Fe³⁺-Fe³⁺ superexchange interaction is very strong, resulting in high Néel temperature (TN) ~ 620 K. The crystal structure of h-LFO, on the other hand, belongs to the polar P63cm space group. Recently, Song et al. have reported hexagonal–orthorhombic morphotropic phase coexistence in LuFeO₃ thin films. They have successfully grown a morphotropic phase mixture (MPM) of the h-LFO and o-LFO polymorphs in a single thin film by suitably altering the film-deposition conditions. Although the o- and h- phases are found to co-exist in both NP and NF, they stabilize in significantly differing proportions depending on the shape. Interestingly, the inclusion of nanoparticles and nanofibers of mixed-phase LuFeO₃ into PDMS renders impressive nanogenerator performance, consistent with the respective ferroelectric phase content. We obtained a maximum measured power density for NP ~0.38 mW/cm³ and for NF ~1.4 mW/cm³.

5.1.1 Materials Synthesis and Characterization

The details of materials synthesis and characterization are presented in the publication by Chaturvedi and Singh et al. .²⁶

Briefly, LFO NP was synthesized using a standard sol-gel route combined with post-synthesis annealing, and the corresponding particulate TEM images are shown in Figure 1(a) and (b). For the synthesis of LFO-NF, the electrospinning technique was used. A solution of 1.39 g of PVP and 6 ml of ethanol was stirred for 12 hours. Then the solution of 1.9268 g of $\text{Fe}(\text{NO}_3)_3 \cdot 9\text{H}_2\text{O}$, and 1.725 g of $\text{Lu}(\text{NO}_3)_3 \cdot x\text{H}_2\text{O}$ with 5 ml ethanol and 5 ml water was prepared. The two solutions thus made were mixed; stirred for 1 h and then the final solution was transferred to a syringe for electrospinning. Electrospinning was performed at 22 kV, and the flow rate was maintained at 0.2 ml h^{-1} . The collected fiber was dried at 373 K and kept for annealing at 1123 K. The corresponding TEM images of Figure 1(d) and (e) establishes the fiber nature of the material. The relative fractions of Hexa and ortho phases (Figure 1(c) and (f)) in NP and NF were found to be significantly different in the two cases.

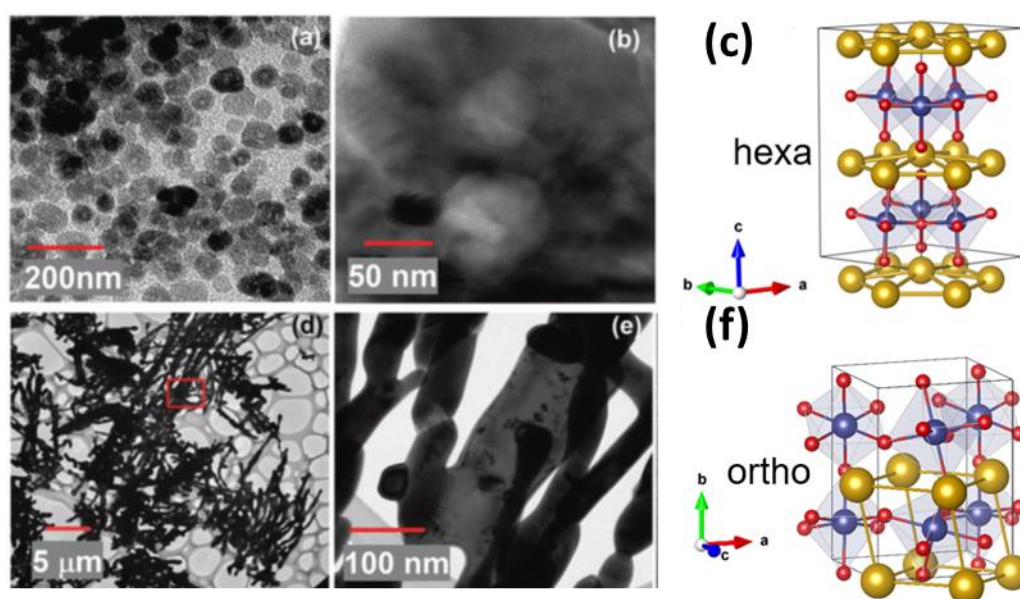


Figure 1 HRTEM images for nanoparticles (a and b), for nanofibers (d and e), Hexagonal and Orthorhombic phases of LuFeO_3 (c and f)

5.1.2 Ferroelectric and Nanogenerator Measurements

The PE loop measurements were done using an FE Test aixACCT TF analyzer 2000. These measurements were performed on the film (made by encapsulating the NP and NF in PDMS matrix) for applied voltage 4 kV and frequency of 25 Hz, over the range of -60 kV cm^{-1} to $+60 \text{ kV cm}^{-1}$ electric field. The nanogenerator device measurements were performed in an indigenous setup consisting of a sewing machine-generated mechanical force setup, a Tektronix MSO 2024 Mixed Signal Oscilloscope, and a Keithley DMM 7510 1/2 digital multimeter.

5.1.3 Nanogenerator device fabrication and performance

To demonstrate the nanogenerator performance of LFO NP and NF, we have fabricated the device using the PDMS (polydimethylsiloxane) matrix. Thus, 5% (w/v) of powder and PDMS solution were taken in a small beaker and mixed thoroughly to obtain a homogeneous solution. The solution was used to make films by the solvent casting method at 70 °C for 3 hours. The prepared film with a thickness of $\sim 700 \mu\text{m}$ was cut precisely into $2 \times 2 \text{ cm}^2$. The prepared film was sandwiched between two ITO (Indium Tin Oxide) coated PET (PolyEthylene Terephthalate) electrodes to create the best possible adhesion. The fabricated device was subjected to 40 N force at a frequency of 14 Hz, and the mechano-electric nanogenerator effect was tested by using a simple sewing machine setup.

5.1.4 Polarization and nanogenerator performance

We measured the polarization loops for the NP and NF films that were used for testing the nanogenerator device. The results of these measurements are shown in Figure 2. For the applied voltage of 4 kV and a frequency of 25 Hz, the ferroelectric loops were obtained without poling the films and are shown in Fig. 1(a). The maximum saturation polarization (P_s) for the LFO NP sample is $\sim 0.03 \mu\text{C cm}^{-2}$, while that for the LFO NF sample is $\sim 0.06 \mu\text{C/cm}^2$. This clearly indicates that the NF exhibits substantially higher polarization than that of NP. We also noticed that the loop for NF displays small jumps. These jumps are similar to those reported previously for ferroelastic hysteresis in $\text{KFe}(\text{MoO}_4)_2$ and are attributed to the elastic equivalent of Barkhausen pulses observed in ferroelectric switching.^{27, 28} One could speculate that inhomogeneous strains induced by embedded anisotropic nanomaterial in the present case may be the cause of observed jumps in the loop.²⁸ When the films for the nanogenerator performance were tested, we obtained an average output voltage of $\sim 3.4 \text{ V}$ for NP and $\sim 6.7 \text{ V}$ for NF. The maximum value of current density for the NP-based sample was $J_{\text{avg}} \sim 10.54 \mu\text{A cm}^{-3}$ at a load resistance of 100 k Ω and for the NF-based sample was $J_{\text{avg}} \sim 15.9 \mu\text{A cm}^{-3}$ at a load resistance of 20 M Ω . The maximum measured power density for NP was $\sim 0.38 \text{ mW cm}^{-3}$ and for NF was $\sim 1.4 \text{ mW cm}^{-3}$. It is noteworthy and intriguing that under the influence of electric as well as mechanical field, the response of NF-based nanogenerator is superior in terms of polarization, output voltage, current density and power density. As established by XRD, the NP (NF) of LFO consist of -o and -h phases in proportion of 75:25 (23: 77). The two phases -o and -h differ significantly in terms of symmetry of the lattice as well as the position of individual cations (Lu and Fe) with respect to each other, which makes a major difference in the ferroelectric behaviour of the material. The -h phase belonging to the polar group P63cm is reported to be contributing to the ferroelectric properties.^{14, 17, 19, 25, 29} recently, -o phase is also reported to display polarization by Chowdhury et al., albeit extremely weak. Before we conclude, it is important to mention that oxygen stoichiometry and defect chemistry are additional important parameters in the context of phase stability, in addition to the shape aspects

and related strain-induced chemical bonding and distortion effects. These have been reported and discussed in the literature through controlled experiments for manipulation of stoichiometry.³⁰⁻³²

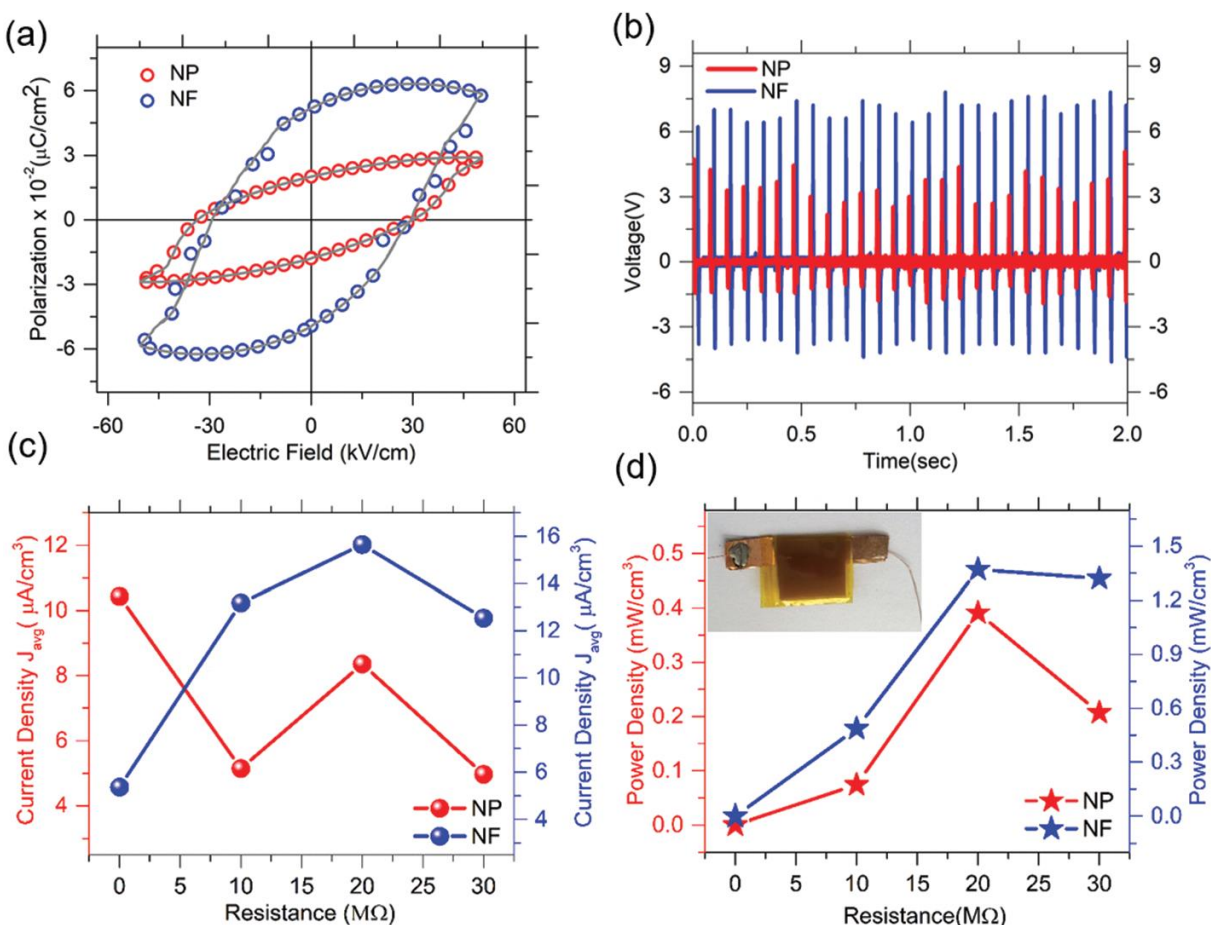


Figure 2 (a) Polarization as a function of the applied voltage for NP and NF, applied voltage 4 kV and applied frequency 25 Hz (grey curve is a guide to the eye), (b) voltage response of the nanogenerator devices made from NP and NF, (c) current density as a function of load resistance for the device of NP and NF, and (d) power density as a function of load resistance for the device of NP and NF. Inset of (d) showing the optical image of the device made for the nanogenerator application

In present work, both the nanostructures are in roughly the same size regime, and both have been annealed at high temperature under an oxidizing atmosphere to achieve the fullest oxidation. Hence we believe that oxygen vacancies should be minimal in such synthesized LFO, and as such, the related tolerance factor issues would not be very significant as the differentiating factor between their phase constitutions. However, further studies will be needed to resolve these issues in depth.

5.2 Triboelectric Nanogenerator based PLD grown MoS₂/h-BN thin films

Since the discovery of graphene, there has been a significant growth of interest and activity in the field of two dimensional (2D) materials in view of their unique set of physical properties driven by surface effects as well as quantum size effects which render a special nature to their electronic density of states.³³⁻³⁶ Among the list of numerous 2D materials of past and emergent interest, MoS₂ is the second most explored material after graphene and has been studied in various applications for over a decade.³⁷ As an n-type transition-metal dichalcogenides semiconductor, MoS₂ exhibits astonishingly diverse, tunable, and application-worthy physical, chemical, mechanical, and optical properties.³⁸⁻⁴⁵ One of the remarkable features of MoS₂ is that it shows multiple polymorphs, the primary polymorphs being 1T (trigonal phase), 1H and 2H (hexagonal phase), and 3R (rhombohedral phase). Importantly, it has been shown that MoS₂ exhibits phase change from semiconductor (2H) to metal (1T) and enhanced hydrogen evolution reaction (HER) activity due to significantly higher electrical conductivity, useful for device fabrications.^{46,47} It is also of great interest to explore the application potential of the films which could be more in the form of mosaics of nanoscale sheets (turbostratic configuration), rather than a single- or few-layer large area uniform coatings. Such a configuration renders a natural benefit of retaining and expressing the properties of few-layer forms of these 2D materials in a thin-film assembly. In this context, the pulsed laser deposition (PLD) technique allows great flexibility of stoichiometry, layer thickness, and growth temperature or ambient control, enabling the growth of different thin-film configurations, their heterostructures, or even superlattices.⁴⁸ Keeping this in mind, we have chosen hexagonal boron nitride (hBN), another prominent layered 2D material to grow nanocomposite films of MoS₂ and hBN, with a hope to induce and stabilize the multiphase in MoS₂ (1T and 2H phases in the present paper, which henceforth we will call biphasic), because of the specific PLD growth dynamics as well as strong interlayer coupling between MoS₂ and hBN. hBN is also intensely researched material due to its exotic optoelectronic properties, mechanical robustness, and thermal stability. It has been extensively studied for various device applications, e.g., field effect transistors, detectors, and photoelectric devices. It is an insulator with a large band gap of ~6 eV, an atomically flat surface without any dangling bonds, charge impurities, and, importantly, it is chemically inert.⁴⁹⁻⁵¹ In this work, relying on the specific strengths and advantages of the PLD technique, we have successfully stabilized biphasic 2D material by growing thin films of the 2D/2D MoS₂-hBN system using a single composite target.

5.2.1 Materials Synthesis and Characterization

The details of materials synthesis and characterization are presented in the publication by Swati parmar et al. .⁵²

We grew ~200-nm pristine MoS₂, hBN (Figure 3) and composite MoS₂-hBN thin films on c-Al₂O₃ (0001) and n-Si substrates by pulsed laser deposition or PLD technique (KrF laser, wavelength

248 nm). All the films were grown at a substrate temperature of 500 °C at a pulse repetition rate of 10 Hz using a laser energy density of 0.5 J/cm², in the presence of 5-mTorr argon pressure. Additionally, we also grew films on flexible Kapton substrates (grown at 400 °C while keeping the other growth conditions the same) for nanogenerator device fabrications.



Figure 3 Atomic structure of hBN and MoS₂

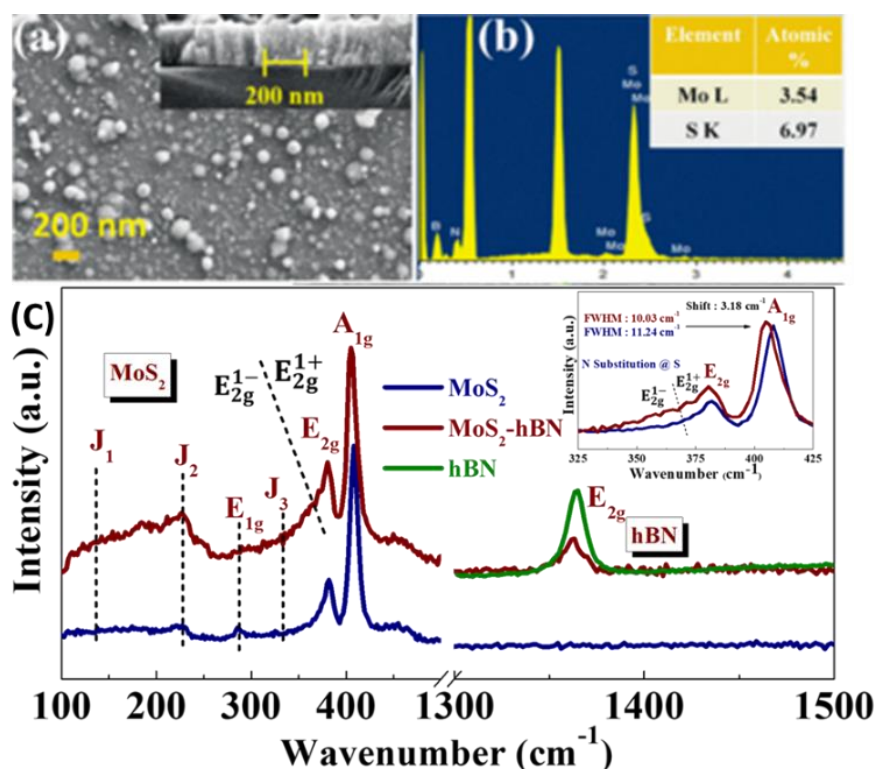


Figure 4 (a) Top and side view (inset) FESEM images of MoS₂-hBN film grown on c-Al₂O₃. Typical grain size is ~50 nm (inset). (b) EDAX analysis of MoS₂-hBN grown on c-Al₂O₃ film confirms a 2:1 compositional ratio of Mo and S in the film; as is well known the lighter (low-Z) element (B, N) stoichiometry is not truthfully revealed by EDAX. (c) Raman spectra of MoS₂, hBN, and MoS₂-hBN composite thin films grown on c-Al₂O₃ substrate, showing the presence of both 1T

and 2H phases of MoS₂. The left side of the x-axis break is for MoS₂ signatures (100 to 500 cm⁻¹), and the right side of the break is for hBN (1300 to 1500 cm⁻¹).

Figure 4(a) along with its inset present the FESEM data (top and side views) for the MoS₂-hBN film grown on a sapphire substrate which describes the features of MoS₂-hBN composite film and flaky features in the case of only MoS₂ film. Compositional analysis through EDAX, is shown in Fig. 4(b). Technically, through EDAX, it is difficult to obtain the reliable compositional ratio of B and N as these are low-Z elements. The biphasic nature was confirmed by Raman spectroscopy. The Raman spectra of MoS₂-hBN thin films were recorded with a 2.33-eV (532 nm) excitation energy laser (Figure 4(c)). The main E_{1g}, E_{2g}, and A_{1g} peaks were observed at 285.4, 381.9, and 408 cm⁻¹, which correspond to the vibration of atoms along in-plane (E_{1g}, E_{2g}) and out-of-plane (A_{1g}) directions, respectively.

5.2.2 TENG Results of MoS₂/h-BN thin films

We designed a TENG device, as shown in Figure 5(a). For this, we grew biphasic MoS₂-hBN (and also MoS₂ and hBN) films on a flexible Kapton substrate at 400 °C, by keeping all the other growth conditions the same in PLD. The lower growth temperature for Kapton substrate as compared to the 500 °C used for sapphire or silicon substrate was based on the consideration of the thermal stability of Kapton. The small difference noted was the lower tailing of the E_{2g} peak, suggested to be due to nitrogen doping of MoS₂. Interestingly the other signatures of the 1T phase (namely, J1, J2, and J3) are quite well defined in this case. The MoS₂-hBN on Kapton and a polypropylene sheet on top of it were sandwiched between two aluminium layers; copper wires were soldered to the electrodes from the top and bottom sides. The area of the sample was 5×10 mm. The mechanical input was applied by a vibrator at 50 Hz with a measured force of 10 N (Figure 5(b)). The output open-circuit voltage (no-load resistance) values obtained for hBN, MoS₂, and MoS₂-hBN are shown in Figure 5(c), while the same is shown on the expanded scale for clarity about the shape of the signals. It can be clearly seen that the open circuit voltages for hBN, MoS₂, and MoS₂-hBN have a ratio of 6: 3: 1.

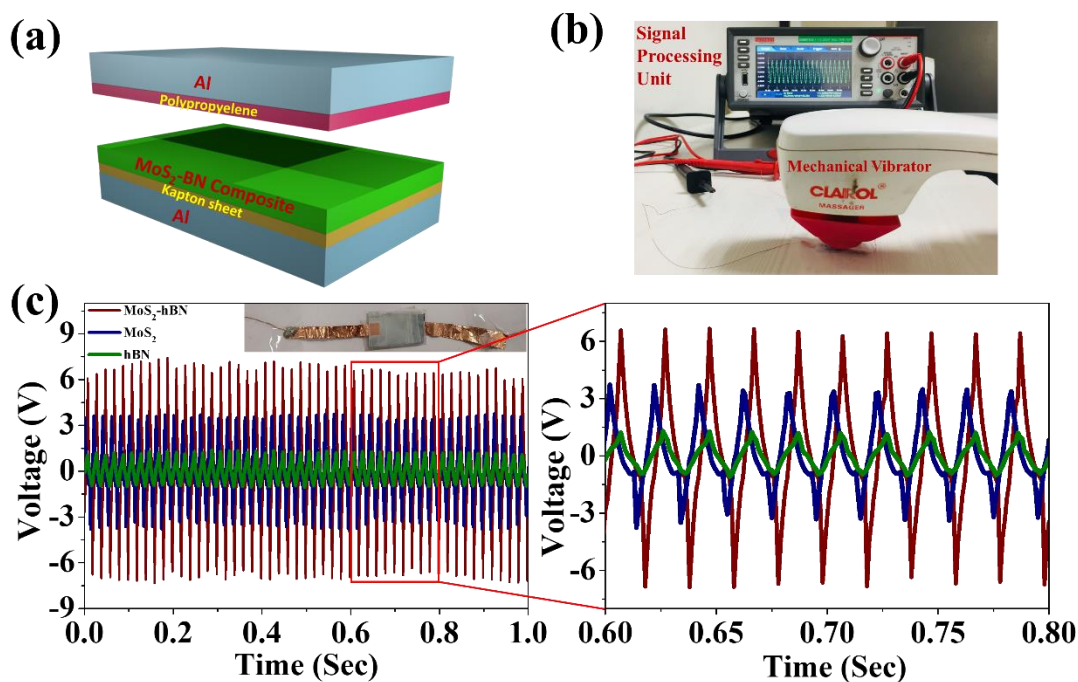


Figure 5(a) Schematic of the device architecture of TENG made of composite biphasic MoS₂-hBN composite thin films. (b) TENG performance measurement setup. (c) The continuous output voltage signal of TENG devices (MoS₂, hBN, and MoS₂-hBN) recorded at 50-Hz frequency.

Thus, there is a twofold increase of average peak-to-peak output voltage for the MoS₂-hBN (~14.7 V) case vis-à-vis pristine MoS₂ (~7.2 V). In contrast, the composite film shows a six-fold increase in average peak-to-peak output voltage with respect to pristine hBN (~2.3 V). This is consistent with the propensity of biphasic film for charging effects under field as reflected by the EFM data. We also estimated the powering capability of the devices based on the three cases by adding a load of 1M (Figure 6). Here again, the composite case shows a higher power delivery. Finally, but interestingly, the shape of the TENG voltage signal curves is peculiar and has been noted before only in the case of 2D materials.⁵³ We will undertake further studies to optimize and enhance the TENG performance in subsequent studies.

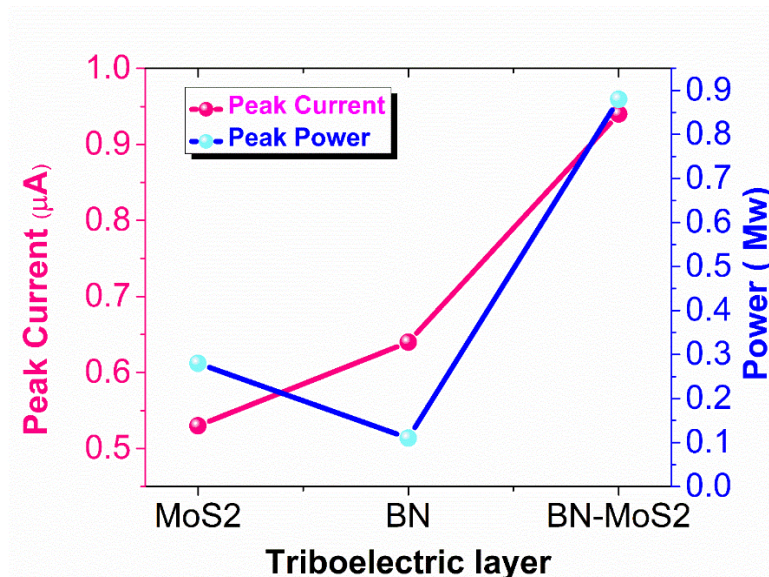


Figure 6 The peak current and power of MoS₂, hBN and MoS₂-hBN TENG devices obtained at 1 MΩ resistance.

5.3 Triboelectric Nano-generator based PLD grown Max thin film

Layered nanolaminate ternary carbides and nitrides are a unique class of materials due to the concurrent existence of both ceramic and metallic properties therein; an unusually interesting combination of application-worthy functionalities.⁵⁴⁻⁵⁷ These ternary materials are popularly known as MAX phases, ($M_{n+1}AX_n$, $n = 1, 2$ and 3 , M is an early transition metal, A is mostly group IIIA and IVA elements, and X is C or N). Until now more than hundred and fifty MAX phase compounds have been discovered, all showing exceptional functionalities. The discovery of MXene from MAX, an analogue of two-dimensional (2D) graphene has ushered in a new era of 2D functional carbides and nitrides.⁵⁸ 2D MXene (Ti_3C_2) can be exfoliated from MAX by selective etching of Al layer by using hydrofluoric (HF) acid or equivalent solution(s). MXenes show enormous promise for multiple application domains, e.g. transparent conductors, electrodes in batteries and supercapacitors, sensors, microwave absorbers, and nanogenerator devices. Surprisingly, in spite of unique physical properties, there are only a few reports on the growth of high-quality thin films of MAX and investigations of their various functional properties.^{52, 59} Therefore, we set out to examine the growth, properties and application-worthiness of MAX films themselves using the well-known stoichiometric-transfer technique of pulsed laser deposition (PLD), applied for various layered two-dimensional materials growth. MAX is found to be lying on the verge of the metal-semiconductor border. Moreover, these *p*-type MAX films also render impressive rectifying characteristics with *n*-Si, as well as impressive triboelectric sensing device performance, useful for biomechanical energy harvesting.

5.3.1 Materials Synthesis and Characterization

The details of materials synthesis and characterization are presented in the publication by Abhijit et al., which is under review.⁶⁰ The MAX films (Figure 7) were grown by PLD (KrF laser of wavelength 248 nm, pulse width 20 ns). The Ti_3AlC_2 target was synthesized by first ball-milling a mixture of Ti, Al and TiC powders (1:1.5:2 molar ratio) at 100 rpm for 24 h in Ar atmosphere and then heating the mixture in a covered alumina crucible in a furnace at 1400 °C for 2 h in Ar atmosphere, as per standard protocols.⁶¹ For the nanogenerator device fabrication, we also used flexible Kapton substrates and grew the films at 400 °C, by keeping all other growth conditions identical.

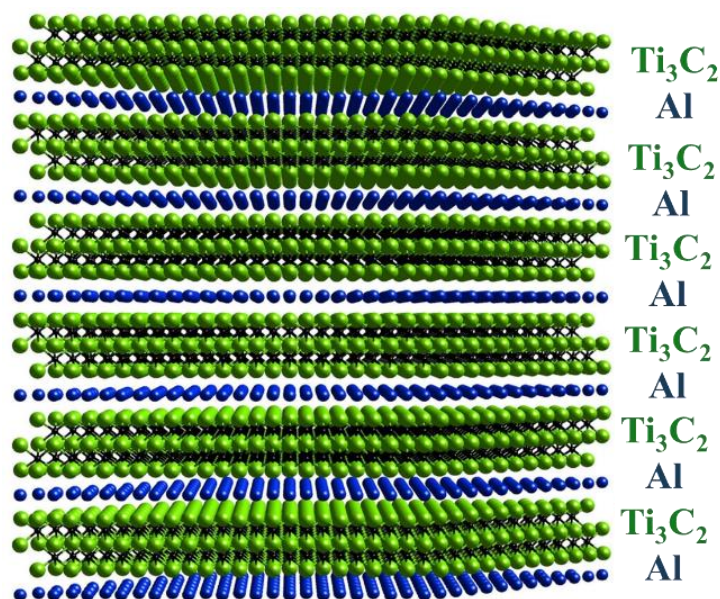


Figure 7 Layered structure of MAX

<http://hims.uva.nl/content/news/2017/11/uva-researchers-report-first-max-phase-catalysis.html?1550930518311>

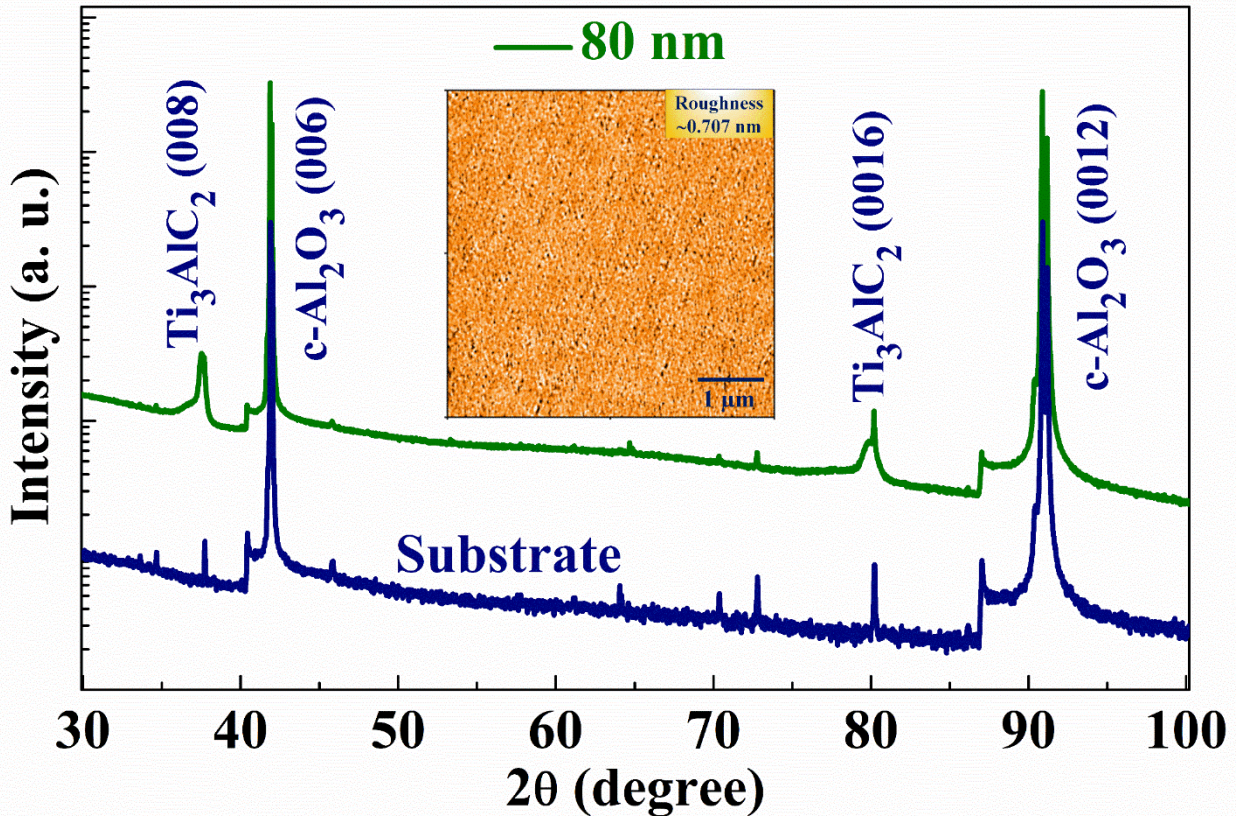


Figure 8 X-ray diffraction pattern of Ti_3AlC_2 (MAX) thin film (80nm) grown on $c-Al_2O_3$ (0001) substrate. Inset topographic imaged by atomic force microscopy of a MAX film (80 nm) showing atomically smooth surface with clear step-terrace structure and roughness of 0.70 nm.

X-ray diffraction (XRD) pattern (Figure 8) obtained from the PXRD set up confirms the formation of oriented MAX phase films. Throughout the θ - 2θ scan, we can only see the (0008) and (00016) diffraction peaks for the films, clearly implying oriented, if not firmly epitaxial, (000 l) out-of-plane texture. The surface topography revealed by atomic force microscopy (AFM) mimics the clear step-terrace pattern of the substrate for thin film, confirming the epitaxial growth and thereby the high crystalline quality of the films.

5.3.2 Fabrication and testing of MAX -TENG

Triboelectric nanogenerator (TENG) devices were fabricated using MAX films. A contact mode TENG architecture was adopted for the design of the touch sensor. To maintain the gap between the top and bottom layer, four 3M double side tapes (1 mm thick) were also used, and were attached at the edges. Total active device area was $1.5 \times 1.5 \text{ cm}^2$. The electrical outputs were measured using a Keithley DMM7510 multimeter by soldering copper wires on the copper tapes on both electrodes

(Al and MAX), with short-circuit current of 3 μ A. We used the PASCO Force sensor to measure the applied force from human-arms, is of \sim 15 N.

We have confirmed the highly metallic nature with *p*-type charge carrier of MAX films; we proceeded to explore the efficacy of these films as an electron-accepting electrode in the triboelectric nanogenerator (TENG) application. In general, TENG devices are in high demand for sensing as well as tribotronics or mechanical energy harvesting applications.^{62, 63} Indeed, energy harvesting from human movements for portable and wearable electronic devices has received considerable attention these days. However, the materials currently in use are limited to a few polymeric systems (including some wherein active materials are embedded in polymers thereby forming composites) wherein issues of efficient charge transport, and transfer, as well as bond-cleaving, wear and physical transfer of material are matters of continuing concern.⁴⁷ Recently, several novel designs of TENGs including use of 2D materials and biomaterials have been researched with very impressive outcomes [40]. Indeed, MXene based TENG devices have shown high open-circuit output voltage (V_{oc}) \sim 500 V to \sim 650 V.⁶⁴ Since MXene has slidable layers laterally with low out-of-plane conductivity, we conjectured that even thin films of the robust MAX phase with excellent mechanical stability and high conductivity could render interesting TENG effects. Thus, we fabricated and tested TENG devices by using MAX films grown on a flexible Kapton substrate, which enables homologous interface contact between the actuator and the device. This also suits the TENG requirement to adapt to flexible/wearable devices.

The schematic of a typical TENG device is shown (Figure 9(a)) where *p*-type conducting MAX was used as a part of the touch sensor device. As stated above, the MAX does not only provides +ve charges (*p*-type) but also acts as a highly conducting bottom electrode for the contact. In contrast, glass microfiber filter paper was used to supply -ve charge carriers. On top of it, aluminium was used as a top electrode. Functionally, when both the layers are almost in contact with each other (by pressing), both *p* and *n*-type carriers feel dipolar forces and exchange of carriers takes place at the interface; generating triboelectric surface charges at the interface. When the pressure is released, the charges (both +ve and -ve) move away from each other. However, to compensate the interfacial triboelectric effect, they build up opposite charges on the bottom surface (of MAX) and the top surface (of aluminium), generating a potential difference. Our TENG device showed impressive peak-to-peak open-circuit output voltage (V_{oc}) \sim 80 V (Figure 9(b)) which could be attributed to efficient contact electrification that can be enhanced by the interface texture of the MAX grown on Kapton.

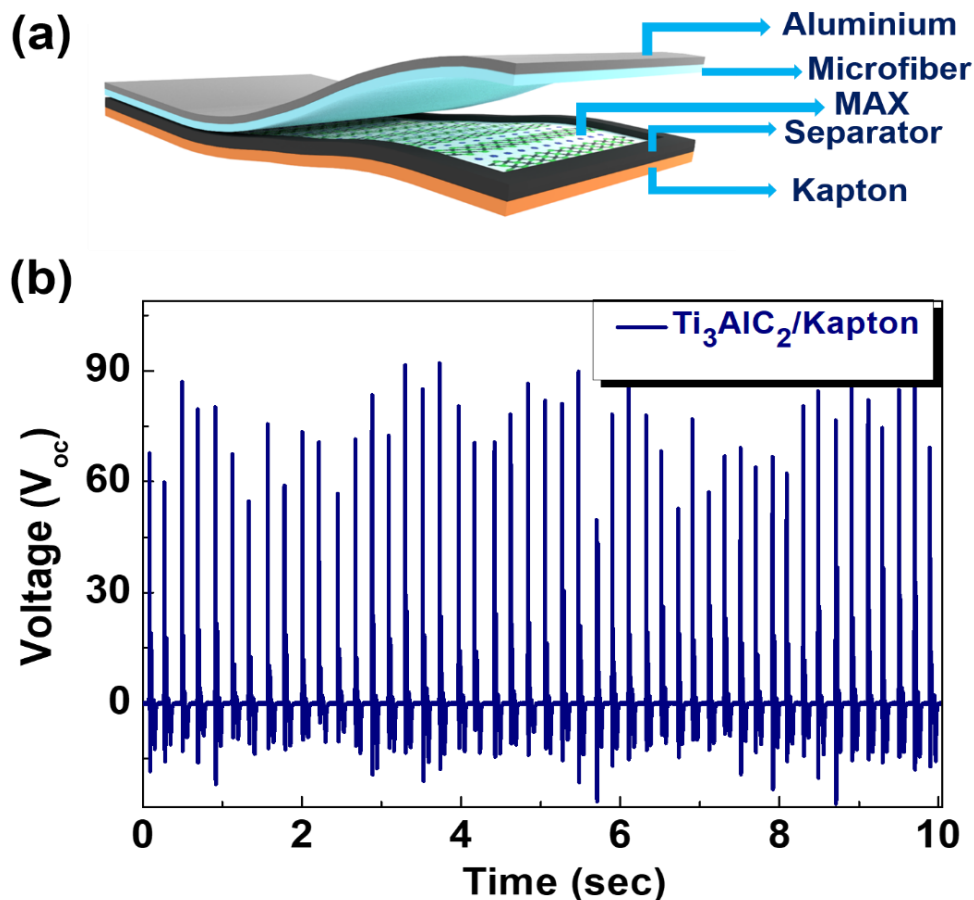


Figure 9 (a) Schematic of a triboelectric nanogenerator (TENG) device containing Ti_3AlC_2 (MAX) film grown on a flexible Kapton substrate. (b) Open circuit voltage (V_{oc}) of the TENG based touch sensor device.

5.4 Conclusions

The work presented in these chapter highlights the property strengths of some emergent classes of materials, their specific morphological and chemical constitutions in rendering an impressive NG or TENG performance.

In the case of $LuFeO_3$, we have fabricated a flexible piezoelectric nanogenerator based on $LuFeO_3$ NPs/NFs–PDMS composite structure for scavenging mechanical energy. The output voltage of the PENG reached up to ~ 3.5 V for NPs-PDMS and ~ 6.7 V for NFs-PDMS under repeating force impacting. A significant structural difference in the two phases and different proportions of -o and -h phases in the nanoparticle and nanofiber systems enable the nanomaterials to demonstrate extraordinary polarization and nanogenerator properties. Impressive nanogenerator performance

of the nanofibers compared to that of nanoparticles is consistent with the higher ferroelectric (-h) phase content therein.

In the case of PLD grown MoS₂, hBN and MoS₂-hBN, the biphasic MoS₂-hBN composite film as an electron acceptor exhibits more than twofold (six-fold) enhanced peak-to-peak output voltage as compared to the pristine MoS₂ (hBN) films. In the composite case, the voltage output of 6V was realized with a force of 10N, which is good for touch sensor application. This study signifies that an increase in the voltage output of the TENGs can be attributed to efficient electron capture in MoS₂-hBN composite film as compared to the MoS₂ and hBN films.

In the case of the PLD grown MAX thin film, a remarkable TENG-based biomechanical touch-sensing capability was noted. In a vertical contact mode configuration of TENG with PLD grown MAX thin film and microfiber paper, the V_{oc} of TENG was found to be 80V for a force of 15 N. We established both rigid and flexible TENGs for harnessing mechanical power in vertical contact mode configuration using MAX as an active triboelectric layer. The flexible MAX based mechanical harvester can be easily integrated into wearable devices to harvest mechanical energy from human motions.

5.7 References

1. Nan, C.-W.; Bichurin, M. I.; Dong, S.; Viehland, D.; Srinivasan, G., Multiferroic magnetoelectric composites: Historical perspective, status, and future directions. *Journal of Applied Physics* **2008**, *103* (3), 031101.
2. Yu, P.; Chu, Y. H.; Ramesh, R., Emergent phenomena at multiferroic heterointerfaces. *Philosophical Transactions of the Royal Society A: Mathematical, Physical and Engineering Sciences* **2012**, *370* (1977), 4856-4871.
3. Dong, S.; Liu, J.-M.; Cheong, S.-W.; Ren, Z., Multiferroic materials and magnetoelectric physics: symmetry, entanglement, excitation, and topology. *Advances in Physics* **2015**, *64* (5-6), 519-626.
4. Spaldin, N. A.; Cheong, S.-W.; Ramesh, R., Multiferroics: Past, present, and future. *Physics Today* **2010**, *63* (10), 38-43.
5. Wang, J.; Neaton, J. B.; Zheng, H.; Nagarajan, V.; Ogale, S. B.; Liu, B.; Viehland, D.; Vaithyanathan, V.; Schlom, D. G.; Waghmare, U. V.; Spaldin, N. A.; Rabe, K. M.; Wuttig, M.; Ramesh, R., Epitaxial BiFeO₃ Multiferroic Thin Film Heterostructures. *Science* **2003**, *299* (5613), 1719-1722.
6. Vaz, C. A. F., Electric field control of magnetism in multiferroic heterostructures. *Journal of Physics: Condensed Matter* **2012**, *24* (33), 333201.
7. Mundy, J. A.; Brooks, C. M.; Holtz, M. E.; Moyer, J. A.; Das, H.; Rébola, A. F.; Heron, J. T.; Clarkson, J. D.; Disseler, S. M.; Liu, Z.; Farhan, A.; Held, R.; Hovden, R.; Padgett, E.; Mao, Q.; Paik, H.; Misra, R.; Kourkoutis, L. F.; Arenholz, E.; Scholl, A.; Borchers, J. A.; Ratcliff, W. D.; Ramesh, R.; Fennie, C. J.; Schiffer, P.; Muller, D. A.; Schlom, D. G., Atomically engineered

ferroic layers yield a room-temperature magnetoelectric multiferroic. *Nature* **2016**, 537 (7621), 523-527.

8. Hur, N.; Park, S.; Sharma, P. A.; Ahn, J. S.; Guha, S.; Cheong, S. W., Electric polarization reversal and memory in a multiferroic material induced by magnetic fields. *Nature* **2004**, 429 (6990), 392-395.

9. Hill, N. A., Why Are There so Few Magnetic Ferroelectrics? *The Journal of Physical Chemistry B* **2000**, 104 (29), 6694-6709.

10. Martin, L. W.; Crane, S. P.; Chu, Y. H.; Holcomb, M. B.; Gajek, M.; Huijben, M.; Yang, C. H.; Balke, N.; Ramesh, R., Multiferroics and magnetoelectrics: thin films and nanostructures. *Journal of Physics: Condensed Matter* **2008**, 20 (43), 434220.

11. Schmid, H., Some symmetry aspects of ferroics and single phase multiferroics*. *Journal of Physics: Condensed Matter* **2008**, 20 (43), 434201.

12. Shi, D.-W.; Javed, K.; Ali, S. S.; Chen, J.-Y.; Li, P.-S.; Zhao, Y.-G.; Han, X.-F., Exchange-biased hybrid ferromagnetic–multiferroic core–shell nanostructures. *Nanoscale* **2014**, 6 (13), 7215-7220.

13. Jeong, Y. K.; Lee, J.-H.; Ahn, S.-J.; Jang, H. M., Epitaxially Constrained Hexagonal Ferroelectricity and Canted Triangular Spin Order in LuFeO₃ Thin Films. *Chemistry of Materials* **2012**, 24 (13), 2426-2428.

14. Wang, W.; Zhao, J.; Wang, W.; Gai, Z.; Balke, N.; Chi, M.; Lee, H. N.; Tian, W.; Zhu, L.; Cheng, X.; Keavney, D. J.; Yi, J.; Ward, T. Z.; Snijders, P. C.; Christen, H. M.; Wu, W.; Shen, J.; Xu, X., Room-Temperature Multiferroic Hexagonal $\{\mathrm{LuFeO}\}_3$ Films. *Physical Review Letters* **2013**, 110 (23), 237601.

15. Wang, H.; Solovyev, I. V.; Wang, W.; Wang, X.; Ryan, P. J.; Keavney, D. J.; Kim, J.-W.; Ward, T. Z.; Zhu, L.; Shen, J.; Cheng, X. M.; He, L.; Xu, X.; Wu, X., Structural and electronic origin of the magnetic structures in hexagonal $\{\mathrm{LuFeO}\}_3$. *Physical Review B* **2014**, 90 (1), 014436.

16. Akbashev, A. R.; Roddatis, V. V.; Vasiliev, A. L.; Lopatin, S.; Amelichev, V. A.; Kaul, A. R., Reconstruction of the polar interface between hexagonal LuFeO₃ and intergrown Fe₃O₄ nanolayers. *Scientific Reports* **2012**, 2 (1), 672.

17. Schwemmer, C.; Knips, L.; Tran, M. C.; de Rosier, A.; Laskowski, W.; Paterek, T.; Weinfurter, H., Genuine Multipartite Entanglement without Multipartite Correlations. *Physical Review Letters* **2015**, 114 (18), 180501.

18. Xu, X.; Wang, W., Multiferroic hexagonal ferrites (h-RFeO₃, R = Y, Dy-Lu): a brief experimental review. *Modern Physics Letters B* **2014**, 28 (21), 1430008.

19. Wang, W.; Wang, H.; Xu, X.; Zhu, L.; He, L.; Wills, E.; Cheng, X.; Keavney, D. J.; Shen, J.; Wu, X.; Xu, X., Crystal field splitting and optical bandgap of hexagonal LuFeO₃ films. *Applied Physics Letters* **2012**, 101 (24), 241907.

20. Roddatis, V. V.; Akbashev, A. R.; Lopatin, S.; Kaul, A. R., Complex structural-ferroelectric domain walls in thin films of hexagonal orthoferrites RFeO₃ (R = Lu, Er). *Applied Physics Letters* **2013**, 103 (11), 112907.

21. Suresh, P.; Laxmi, K. V.; Kumar, P. S. A., Synthesis and structural properties of hexagonal-LuFeO₃ nanoparticles. *AIP Conference Proceedings* **2016**, 1728 (1), 020472.

22. Chowdhury, U.; Goswami, S.; Bhattacharya, D.; Ghosh, J.; Basu, S.; Neogi, S., Room temperature multiferroicity in orthorhombic LuFeO₃. *Applied Physics Letters* **2014**, 105 (5), 052911.

23. Zhou, M.; Yang, H.; Xian, T.; Li, R. S.; Zhang, H. M.; Wang, X. X., Sonocatalytic degradation of RhB over LuFeO₃ particles under ultrasonic irradiation. *Journal of Hazardous Materials* **2015**, *289*, 149-157.
24. Qin, Y.; Liu, X. Q.; Chen, X. M., Dielectric, ferroelectric and magnetic properties of Mn-doped LuFeO₃ ceramics. *Journal of Applied Physics* **2013**, *113* (4), 044113.
25. Ahmad, T.; Lone, I. H., Development of multifunctional lutetium ferrite nanoparticles: Structural characterization and properties. *Materials Chemistry and Physics* **2017**, *202*, 50-55.
26. Chaturvedi, S.; Singh, S. K.; Shyam, P.; Shirolkar, M. M.; Krishna, S.; Boomishankar, R.; Ogale, S., Nanoscale LuFeO₃: shape dependent ortho/hexa-phase constitution and nanogenerator application. *Nanoscale* **2018**, *10* (45), 21406-21413.
27. Navrotsky, A.; Mazeina, L.; Majzlan, J., Size-Driven Structural and Thermodynamic Complexity in Iron Oxides. *Science* **2008**, *319* (5870), 1635-1638.
28. Scott, J. F.; Gardner, J., Ferroelectrics, multiferroics and artifacts: Lozenge-shaped hysteresis and things that go bump in the night. *Materials Today* **2018**, *21* (5), 553-562.
29. Cao, S.; Zhang, X.; Paudel, T. R.; Sinha, K.; Wang, X.; Jiang, X.; Wang, W.; Brutsche, S.; Wang, J.; Ryan, P. J.; Kim, J.-W.; Cheng, X.; Tsymbal, E. Y.; Dowben, P. A.; Xu, X., On the structural origin of the single-ion magnetic anisotropy in LuFeO₃. *Journal of Physics: Condensed Matter* **2016**, *28* (15), 156001.
30. Kim, J.; Koo, Y. M.; Sohn, K.-S.; Shin, N., Symmetry-mode analysis of the ferroelectric transition in YMnO₃. *Applied Physics Letters* **2010**, *97* (9), 092902.
31. Remsen, S.; Dabrowski, B.; Chmaissem, O.; Mais, J.; Szewczyk, A., Synthesis and oxygen content dependent properties of hexagonal DyMnO_{3+δ}. *Journal of Solid State Chemistry* **2011**, *184* (8), 2306-2314.
32. Selbach, S. M.; Nordli Løvik, A.; Bergum, K.; Tolchard, J. R.; Einarsrud, M.-A.; Grande, T., Crystal structure, chemical expansion and phase stability of HoMnO₃ at high temperature. *Journal of Solid State Chemistry* **2012**, *196*, 528-535.
33. Novoselov, K. S.; Geim, A. K.; Morozov, S. V.; Jiang, D.; Zhang, Y.; Dubonos, S. V.; Grigorieva, I. V.; Firsov, A. A., Electric Field Effect in Atomically Thin Carbon Films. *Science* **2004**, *306* (5696), 666-669.
34. Ferrari, A. C.; Bonaccorso, F.; Fal'ko, V.; Novoselov, K. S.; Roche, S.; Bøggild, P.; Borini, S.; Koppens, F. H. L.; Palermo, V.; Pugno, N.; Garrido, J. A.; Sordan, R.; Bianco, A.; Ballerini, L.; Prato, M.; Lidorikis, E.; Kivioja, J.; Marinelli, C.; Ryhänen, T.; Morpurgo, A.; Coleman, J. N.; Nicolosi, V.; Colombo, L.; Fert, A.; Garcia-Hernandez, M.; Bachtold, A.; Schneider, G. F.; Guinea, F.; Dekker, C.; Barbone, M.; Sun, Z.; Galiotis, C.; Grigorenko, A. N.; Konstantatos, G.; Kis, A.; Katsnelson, M.; Vandersypen, L.; Loiseau, A.; Morandi, V.; Neumaier, D.; Treossi, E.; Pellegrini, V.; Polini, M.; Tredicucci, A.; Williams, G. M.; Hee Hong, B.; Ahn, J.-H.; Min Kim, J.; Zirath, H.; van Wees, B. J.; van der Zant, H.; Occhipinti, L.; Di Matteo, A.; Kinloch, I. A.; Seyller, T.; Quesnel, E.; Feng, X.; Teo, K.; Rupesinghe, N.; Hakonen, P.; Neil, S. R. T.; Tannock, Q.; Löfwander, T.; Kinaret, J., Science and technology roadmap for graphene, related two-dimensional crystals, and hybrid systems. *Nanoscale* **2015**, *7* (11), 4598-4810.
35. Han, W., Perspectives for spintronics in 2D materials. *APL Materials* **2016**, *4* (3), 032401.
36. Liu, Y.; Weiss, N. O.; Duan, X.; Cheng, H.-C.; Huang, Y.; Duan, X., Van der Waals heterostructures and devices. *Nature Reviews Materials* **2016**, *1* (9), 16042.
37. Ramakrishna Matte, H. S. S.; Gomathi, A.; Manna, A. K.; Late, D. J.; Datta, R.; Pati, S. K.; Rao, C. N. R., MoS₂ and WS₂ Analogues of Graphene. *Angewandte Chemie International Edition* **2010**, *49* (24), 4059-4062.

38. Duan, X.; Wang, C.; Pan, A.; Yu, R.; Duan, X., Two-dimensional transition metal dichalcogenides as atomically thin semiconductors: opportunities and challenges. *Chemical Society Reviews* **2015**, *44* (24), 8859-8876.
39. Lin, Z.; McCreary, A.; Briggs, N.; Subramanian, S.; Zhang, K.; Sun, Y.; Li, X.; Borys, N. J.; Yuan, H.; Fullerton-Shirey, S. K.; Chernikov, A.; Zhao, H.; McDonnell, S.; Lindenberg, A. M.; Xiao, K.; LeRoy, B. J.; Drndić, M.; Hwang, J. C. M.; Park, J.; Chhowalla, M.; Schaak, R. E.; Javey, A.; Hersam, M. C.; Robinson, J.; Terrones, M., 2D materials advances: from large scale synthesis and controlled heterostructures to improved characterization techniques, defects and applications. *2D Materials* **2016**, *3* (4), 042001.
40. Manzeli, S.; Ovchinnikov, D.; Pasquier, D.; Yazyev, O. V.; Kis, A., 2D transition metal dichalcogenides. *Nature Reviews Materials* **2017**, *2* (8), 17033.
41. Wang, Q. H.; Kalantar-Zadeh, K.; Kis, A.; Coleman, J. N.; Strano, M. S., Electronics and optoelectronics of two-dimensional transition metal dichalcogenides. *Nature Nanotechnology* **2012**, *7* (11), 699-712.
42. Ye, J. T.; Zhang, Y. J.; Akashi, R.; Bahramy, M. S.; Arita, R.; Iwasa, Y., Superconducting Dome in a Gate-Tuned Band Insulator. *Science* **2012**, *338* (6111), 1193-1196.
43. Chen, X.; Wu, Z.; Xu, S.; Wang, L.; Huang, R.; Han, Y.; Ye, W.; Xiong, W.; Han, T.; Long, G.; Wang, Y.; He, Y.; Cai, Y.; Sheng, P.; Wang, N., Probing the electron states and metal-insulator transition mechanisms in molybdenum disulphide vertical heterostructures. *Nature Communications* **2015**, *6* (1), 6088.
44. Qian, X.; Liu, J.; Fu, L.; Li, J., Quantum spin Hall effect in two-dimensional transition metal dichalcogenides. *Science* **2014**, *346* (6215), 1344-1347.
45. Lin, Z.; Carvalho, B. R.; Kahn, E.; Lv, R.; Rao, R.; Terrones, H.; Pimenta, M. A.; Terrones, M., Defect engineering of two-dimensional transition metal dichalcogenides. *2D Materials* **2016**, *3* (2), 022002.
46. Hu, Z.; Zhang, S.; Zhang, Y.-N.; Wang, D.; Zeng, H.; Liu, L.-M., Modulating the phase transition between metallic and semiconducting single-layer MoS₂ and WS₂ through size effects. *Physical Chemistry Chemical Physics* **2015**, *17* (2), 1099-1105.
47. Seol, M.; Kim, S.; Cho, Y.; Byun, K.-E.; Kim, H.; Kim, J.; Kim, S. K.; Kim, S.-W.; Shin, H.-J.; Park, S., Triboelectric Series of 2D Layered Materials. *Advanced Materials* **2018**, *30* (39), 1801210.
48. Wang, S.; Wang, X.; Warner, J. H., All Chemical Vapor Deposition Growth of MoS₂:h-BN Vertical van der Waals Heterostructures. *ACS Nano* **2015**, *9* (5), 5246-5254.
49. Duerloo, K.-A. N.; Ong, M. T.; Reed, E. J., Intrinsic Piezoelectricity in Two-Dimensional Materials. *The Journal of Physical Chemistry Letters* **2012**, *3* (19), 2871-2876.
50. Qi, J.; Qian, X.; Qi, L.; Feng, J.; Shi, D.; Li, J., Strain-Engineering of Band Gaps in Piezoelectric Boron Nitride Nanoribbons. *Nano Letters* **2012**, *12* (3), 1224-1228.
51. Michel, K. H.; Verberck, B., Phonon dispersions and piezoelectricity in bulk and multilayers of hexagonal boron nitride. *Physical Review B* **2011**, *83* (11), 115328.
52. Parmar, S.; Biswas, A.; Kumar Singh, S.; Ray, B.; Parmar, S.; Gosavi, S.; Sathe, V.; Janay Choudhary, R.; Datar, S.; Ogale, S., Coexisting 1T/2H polymorphs, reentrant resistivity behavior, and charge distribution in MoS₂-hBN 2D/2D composite thin films. *Physical Review Materials* **2019**, *3* (7), 074007.
53. Lee, J.-H.; Park, J. Y.; Cho, E. B.; Kim, T. Y.; Han, S. A.; Kim, T.-H.; Liu, Y.; Kim, S. K.; Roh, C. J.; Yoon, H.-J.; Ryu, H.; Seung, W.; Lee, J. S.; Lee, J.; Kim, S.-W., Reliable

- Piezoelectricity in Bilayer WSe₂ for Piezoelectric Nanogenerators. *Advanced Materials* **2017**, 29 (29), 1606667.
54. Barsoum, M. R. a. M. W., MAX phases: Bridging the gap between metals and ceramics. *American Ceramic Society Bulletin* **2013**, 92 (20).
55. Barsoum, M. W., The MN+1AXN phases: A new class of solids: Thermodynamically stable nanolaminates. *Progress in Solid State Chemistry* **2000**, 28 (1), 201-281.
56. Barsoum, M. W.; Radovic, M., Elastic and Mechanical Properties of the MAX Phases. *Annual Review of Materials Research* **2011**, 41 (1), 195-227.
57. Tzenov, N. V.; Barsoum, M. W., Synthesis and Characterization of Ti₃AlC₂. *Journal of the American Ceramic Society* **2000**, 83 (4), 825-832.
58. Tang, H.; Hu, Q.; Zheng, M.; Chi, Y.; Qin, X.; Pang, H.; Xu, Q., MXene–2D layered electrode materials for energy storage. *Progress in Natural Science: Materials International* **2018**, 28 (2), 133-147.
59. Mandal, R.; Babar, R.; Tripathi, M.; Datta, S.; Rawat, R.; Choudhary, R. J.; Kabir, M.; Ogale, S., Modulation of ferromagnetism and transport in B_xC_yN_z thin films via nitrogen doping and defects. *Journal of Magnetism and Magnetic Materials* **2019**, 479, 67-73.
60. Abhijit Biswas, A. S., Umashankar Rajput, Sachin Kumar Singh, Vivek Antad, Swati Parmar, Dibyata Rout, Aparna Deshpande, Sunil Nair and Satishchandra Ogale, Growth, Properties and Applications of Layered Nanolaminate Ti₃AlC₂ MAX Phase Thin Films. *Physical Review Applied* **2019**, Under Review
61. Spanier, J. E.; Gupta, S.; Amer, M.; Barsoum, M. W., Vibrational behavior of the Mn+1AX_n phases from first-order Raman scattering (M=Ti,V,Cr, A=Si, X=C,N). *Physical Review B* **2005**, 71 (1), 012103.
62. Fan, F.-R.; Tian, Z.-Q.; Lin Wang, Z., Flexible triboelectric generator. *Nano Energy* **2012**, 1 (2), 328-334.
63. Wu, C.; Wang, A. C.; Ding, W.; Guo, H.; Wang, Z. L., Triboelectric Nanogenerator: A Foundation of the Energy for the New Era. *Advanced Energy Materials* **2019**, 9 (1), 1802906.
64. Dong, Y.; Mallineni, S. S. K.; Maleski, K.; Behlow, H.; Mochalin, V. N.; Rao, A. M.; Gogotsi, Y.; Podila, R., Metallic MXenes: A new family of materials for flexible triboelectric nanogenerators. *Nano Energy* **2018**, 44, 103-110.

Chapter 6

Conclusion and future perspectives

6.1 Thesis Summary

In summary, this thesis presents the generation of electrical energy utilizing a clean and renewable energy source to scale down the burden of conventional fossil fuel consumption. In the first part, the thesis discusses the synthesis of PDMS-polymer composite films of a 2D material (black phosphorus) and its application in the field of self-powered devices which can harvest energy from different mechanical/motional sources. The BP-PDMS composite films exhibited outstanding stability for several months which makes them potential materials for durable electronics. In another work, seed-based TENGs were fabricated and shown to exhibit excellent output performance in terms of the generated power densities. This study demonstrates the effectiveness of clean energy production from naturally abundant materials.

In the subsequent chapter, a synthetic hybrid organic-inorganic ferroelectric material for nanogenerator application has also been explored. A 1D-coordination polymer made up of weakly coordinating Rb cation, and moderately basic diisopropyl imido anion was synthesised and shown to exhibit a good remnant polarization value. A preliminary device of the complex has been fabricated along with the PVA polymer offered an excellent flexibility and output performance towards piezoelectric nanogenerator application. Finally, polymer devices made up of emergent nanomaterials such as metal-oxides and MAX have been prepared and shown to exhibit excellent device attributes.

6.2 Future Direction

Researchers have demonstrated nanogenerators as self-powered devices which can harvest mechanical energy from several approaches. But there are many aspects where this technology requires considerable attention to be realised as a commercial product. To explore nanogenerator as an innovative research field in the future, one has to consider the following important aspects:

(1) The charge transfer mechanism via contact electrification is not thoroughly understood. Fundamental aspects behind this phenomenon need experimental proofs. Mass transfer or charge

transfer, the science of these two directions should be taken up in the upcoming days which will boost the performance of TENG.

(2) Nanogenerator devices necessitate good polymer packaging so that they can sustain even in harsh environments without any significant decrease in their output performances.

(3) Though TENG furnishes high output voltage and low current they are still not at par with the solar and thermoelectric cells. This calls for the proper research on the power management circuit which can deliver the best performance without any significant amount of energy loss.

(4) Hybrid energy cells that can exhibit multi-modal energy harvesting can also afford a promising and meaningful direction in research. Such multi-mode energy harvesting might involve hybrid energy cells such as Solar NG and battery NG that can lay a substantial pathway towards self-powered technology.

Permissions

Chapter 1

Figure 1

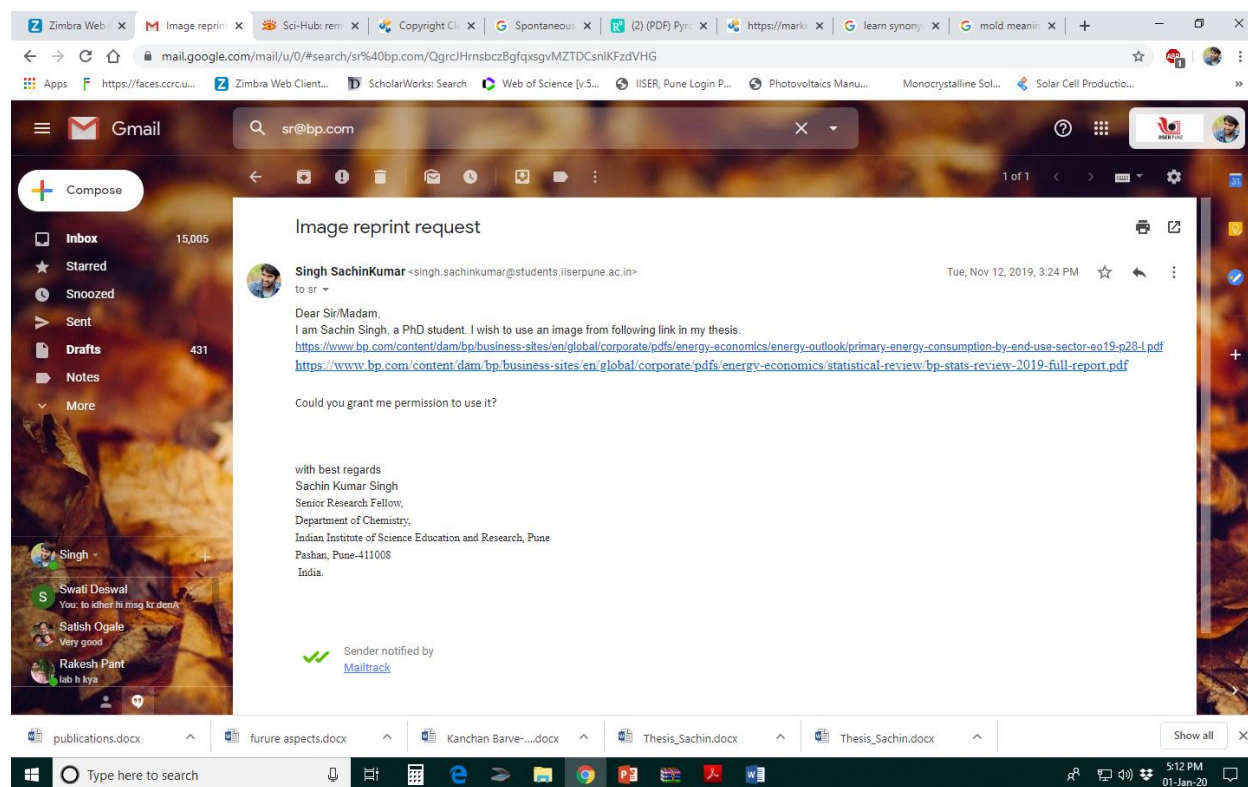


Figure 2

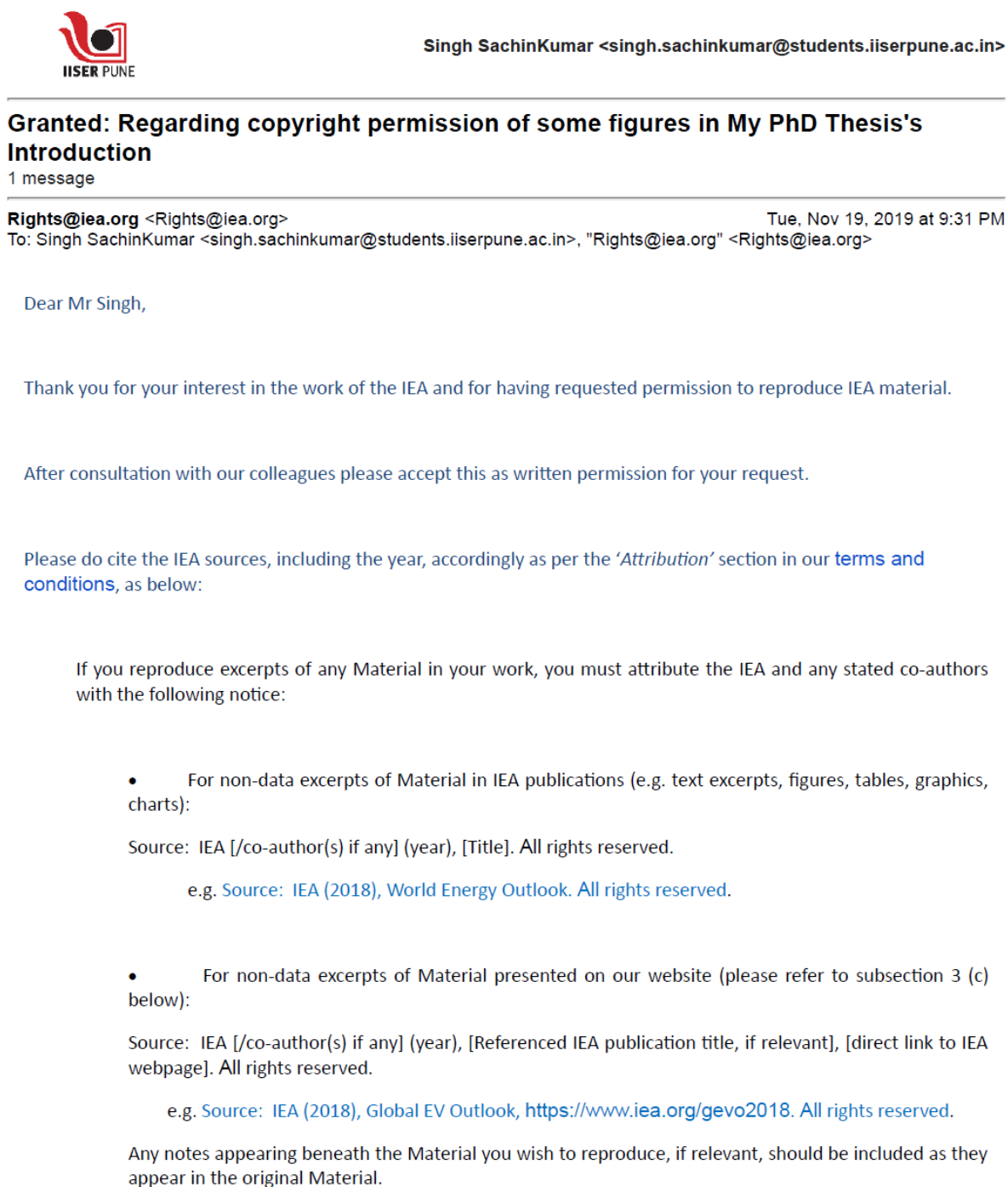
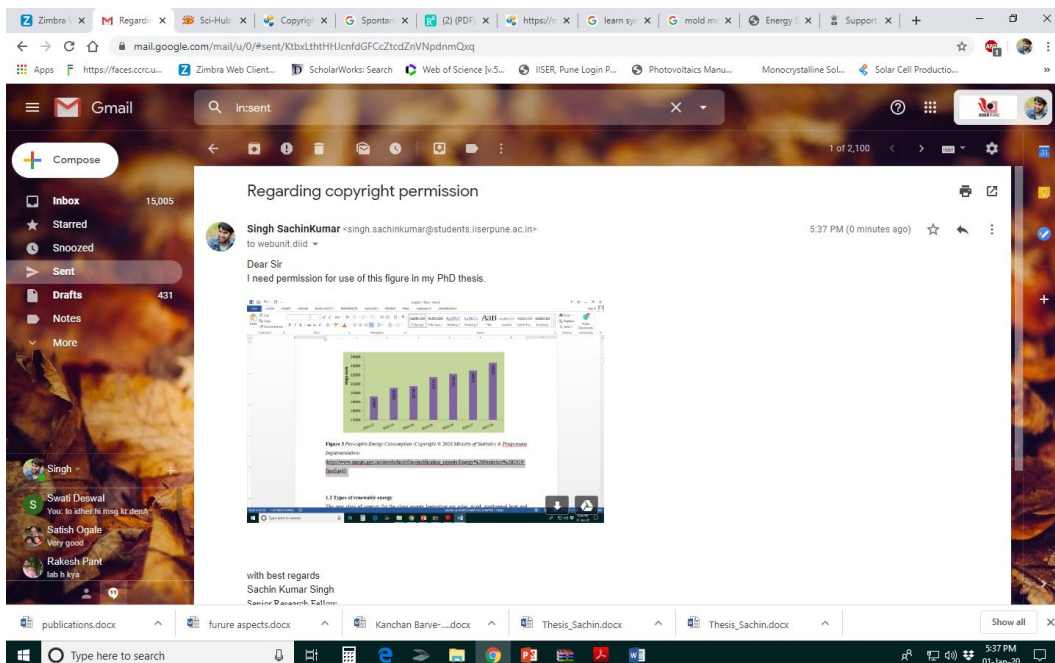
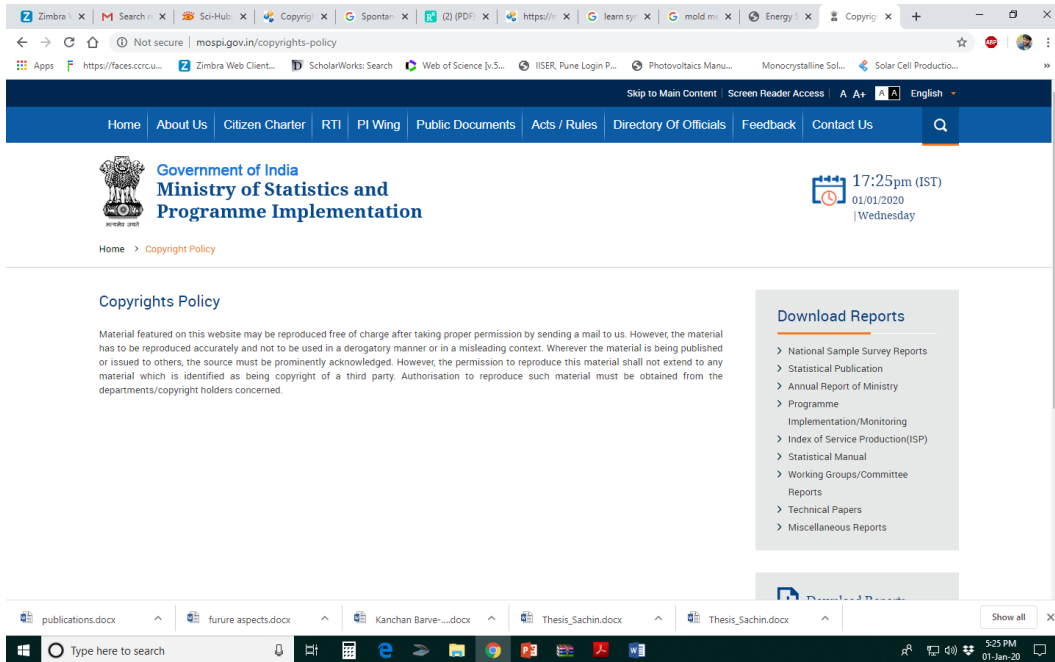


Figure 3





Singh SachinKumar <singh.sachinkumar@students.iiserpune.ac.in>

Thank you for your order with RightsLink / Elsevier

2 messages

no-reply@copyright.com <no-reply@copyright.com>
To: singh.sachinkumar@students.iiserpune.ac.in

Tue, Dec 31, 2019 at 5:16 PM



Thank you for your order!

Dear Mr. Sachin Singh,

Thank you for placing your order through Copyright Clearance Center's RightsLink® service.

Order Summary

Licensee: Mr. Sachin Singh
Order Date: Dec 31, 2019
Order Number: 4739300650244
Publication: Elsevier Books
Title: Electrochemical Energy Storage for Renewable Sources and Grid Balancing
Type of Use: reuse in a thesis/dissertation
Order Total: 0.00 USD

View or print complete [details](#) of your order and the publisher's terms and conditions.

Sincerely,

Copyright Clearance Center

Tel: +1-855-239-3415 / +1-978-646-2777
customer@copyright.com
<https://myaccount.copyright.com>



Figure 5

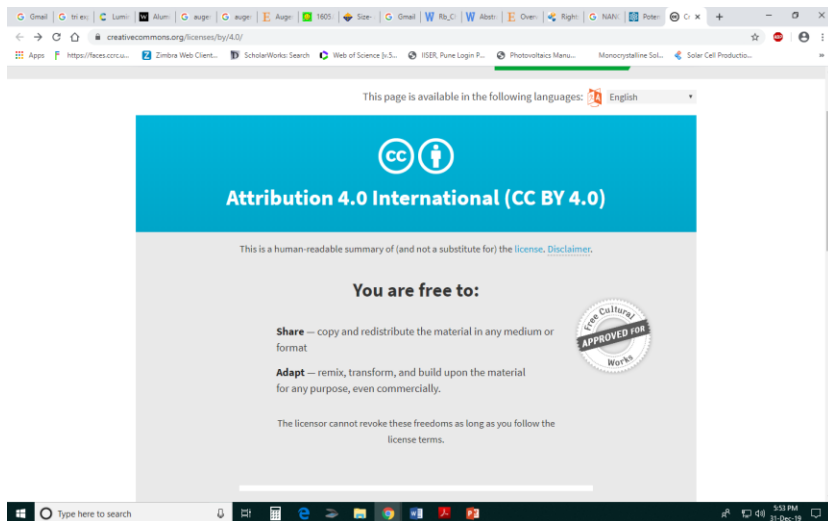
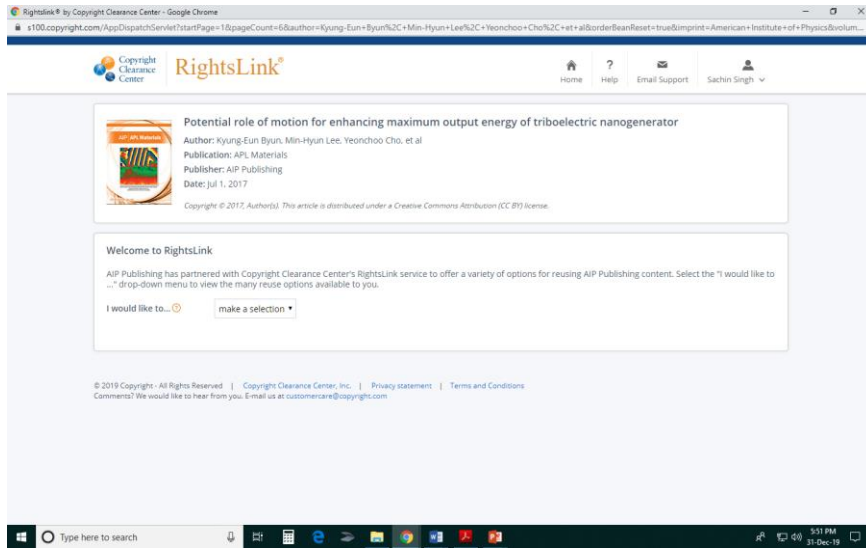
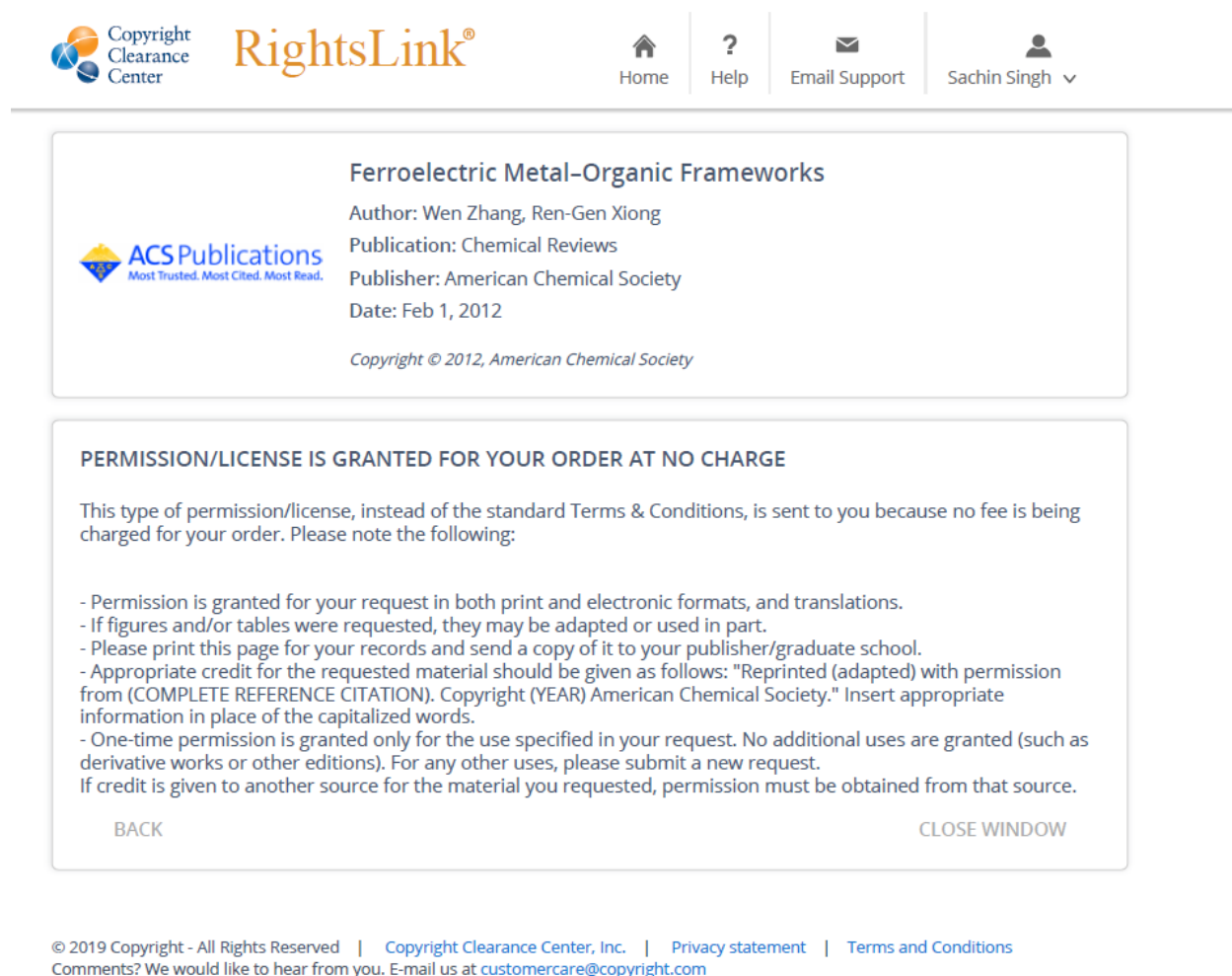


Figure 7



The screenshot shows the RightsLink interface. At the top, there are logos for the Copyright Clearance Center and RightsLink®, along with navigation links for Home, Help, Email Support, and a user profile for Sachin Singh. The main content area displays the title 'Ferroelectric Metal-Organic Frameworks' and provides author, publication, publisher, and date information. Below this, a message states that a permission/license is granted for the order at no charge, followed by a list of conditions and a 'BACK' button. At the bottom of the page, there is a copyright notice and contact information for the Copyright Clearance Center, Inc.

Copyright Clearance Center RightsLink®

Home ? Email Support Sachin Singh ▾

Ferroelectric Metal-Organic Frameworks

Author: Wen Zhang, Ren-Gen Xiong
 Publication: Chemical Reviews
 Publisher: American Chemical Society
 Date: Feb 1, 2012

ACS Publications
 Most Trusted. Most Cited. Most Read.

Copyright © 2012, American Chemical Society

PERMISSION/LICENSE IS GRANTED FOR YOUR ORDER AT NO CHARGE

This type of permission/license, instead of the standard Terms & Conditions, is sent to you because no fee is being charged for your order. Please note the following:

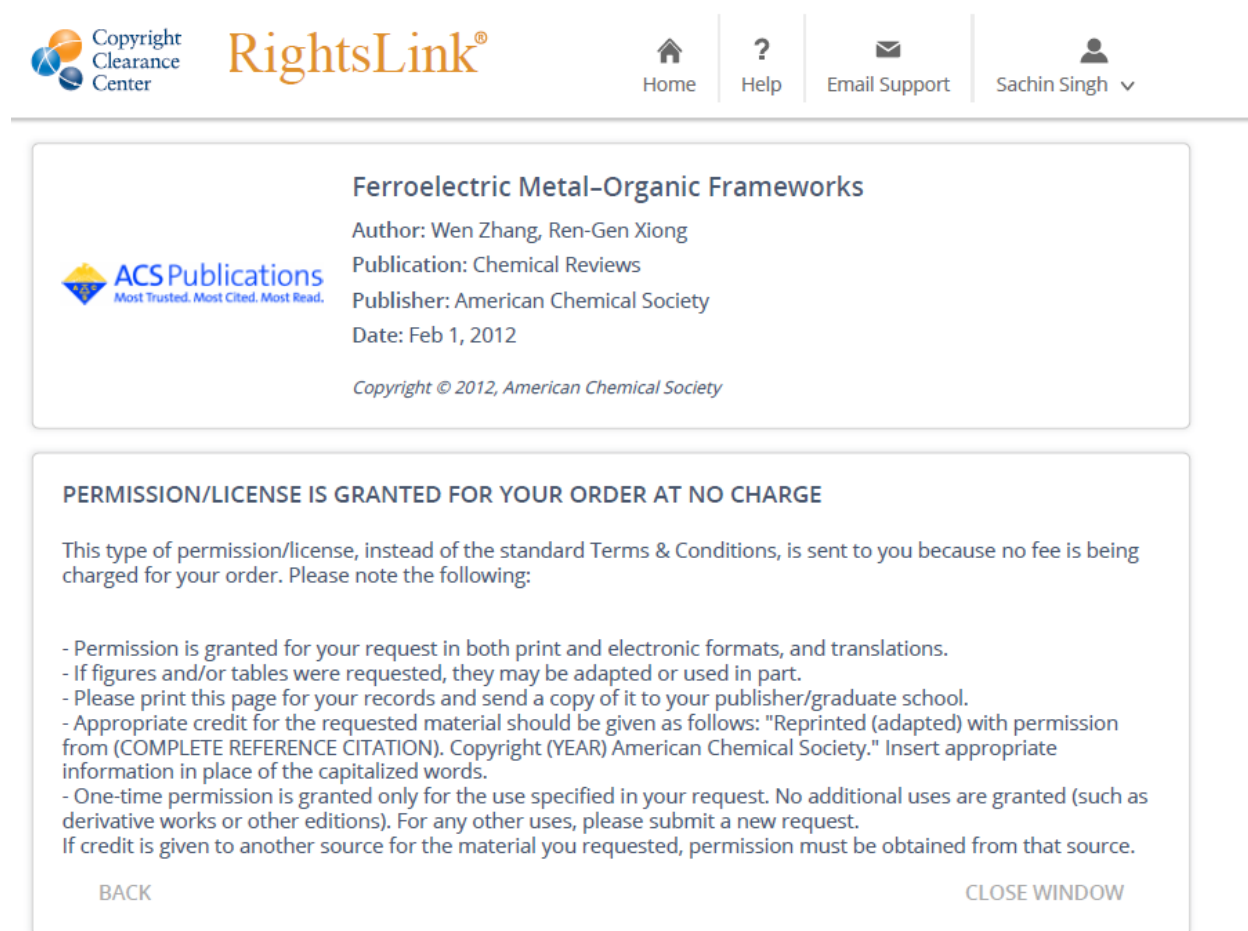
- Permission is granted for your request in both print and electronic formats, and translations.
- If figures and/or tables were requested, they may be adapted or used in part.
- Please print this page for your records and send a copy of it to your publisher/graduate school.
- Appropriate credit for the requested material should be given as follows: "Reprinted (adapted) with permission from (COMPLETE REFERENCE CITATION). Copyright (YEAR) American Chemical Society." Insert appropriate information in place of the capitalized words.
- One-time permission is granted only for the use specified in your request. No additional uses are granted (such as derivative works or other editions). For any other uses, please submit a new request.

If credit is given to another source for the material you requested, permission must be obtained from that source.

BACK CLOSE WINDOW

© 2019 Copyright - All Rights Reserved | Copyright Clearance Center, Inc. | Privacy statement | Terms and Conditions
 Comments? We would like to hear from you. E-mail us at customer care@copyright.com

Figure 8



Copyright Clearance Center **RightsLink**[®] Home ? Email Support Sachin Singh ▾

Ferroelectric Metal-Organic Frameworks
 Author: Wen Zhang, Ren-Gen Xiong
 Publication: Chemical Reviews
 Publisher: American Chemical Society
 Date: Feb 1, 2012
 Copyright © 2012, American Chemical Society

ACS Publications
 Most Trusted. Most Cited. Most Read.

PERMISSION/LICENSE IS GRANTED FOR YOUR ORDER AT NO CHARGE

This type of permission/license, instead of the standard Terms & Conditions, is sent to you because no fee is being charged for your order. Please note the following:

- Permission is granted for your request in both print and electronic formats, and translations.
- If figures and/or tables were requested, they may be adapted or used in part.
- Please print this page for your records and send a copy of it to your publisher/graduate school.
- Appropriate credit for the requested material should be given as follows: "Reprinted (adapted) with permission from (COMPLETE REFERENCE CITATION). Copyright (YEAR) American Chemical Society." Insert appropriate information in place of the capitalized words.
- One-time permission is granted only for the use specified in your request. No additional uses are granted (such as derivative works or other editions). For any other uses, please submit a new request.

If credit is given to another source for the material you requested, permission must be obtained from that source.

BACK CLOSE WINDOW

Marketplace™

Dear Sachin Singh,
 Thank you for placing your order on [Marketplace™](#).

Order Summary:
 Order date: 01 Jan 2020
 Order number: 1011278
 No. of items: 1
 Order total: 0.00 USD

Billing Summary:
 Payment method: Invoice
 An invoice will be generated and emailed within 24 hours.

To view your order details, click the following link, sign in, and search for your order:
[Manage Account](#)

Please do not reply to this message.

To speak with a Customer Service Representative, call +1-855-239-3415 toll free or +1-978-646-2600 (24 hours a day), or email your questions and comments to support@copyright.com.

Sincerely,
 The CCC Marketplace Team

Tel: 1-855-239-3415 / +1-978-646-2600
support@copyright.com
[Manage Account](#)


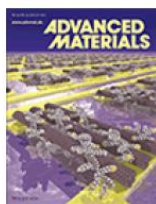


Figure 9



Thank you for your order!

Dear Mr. Sachin Singh,

Thank you for placing your order through Copyright Clearance Center's RightsLink® service.

Order Summary

Licensee: Mr. Sachin Singh
 Order Date: Dec 31, 2019
 Order Number: 4739390859688
 Publication: Advanced Materials
 Title: Flexible Nanogenerators for Energy Harvesting and Self-Powered Electronics
 Type of Use: Dissertation/Thesis
 Order Total: 0.00 USD

View or print complete [details](#) of your order and the publisher's terms and conditions.

Sincerely,

Copyright Clearance Center

Tel: +1-855-239-3415 / +1-978-646-2777
 customer@copyright.com
<https://myaccount.copyright.com>



Figure 10

IEEE copyright line © 2011 IEEE

The screenshot shows a web browser window with the URL `s100.copyright.com/AppDispatchServlet#formTop`. The main content area displays the following information:

Piezoelectric Nanogenerators for Self-Powered Nanodevices
 Author: Zhong Lin Wang
 Publication: IEEE Pervasive Computing Magazine
 Publisher: IEEE
 Date: Jan.-March 2008
 Copyright © 2008, IEEE

Below this, there is a section titled "Thesis / Dissertation Reuse" with the following text:

The IEEE does not require individuals working on a thesis to obtain a formal reuse license, however, you may print out this statement to be used as a permission grant:

Requirements to be followed when using any portion (e.g., figure, graph, table, or textual material) of an IEEE copyrighted paper in a thesis:

- 1) In the case of textual material (e.g., using short quotes or referring to the work within these papers) users must give full credit to the original source (author, paper, publication) followed by the IEEE copyright line © 2011 IEEE.
- 2) In the case of illustrations or tabular material, we require that the copyright line © [Year of original publication] IEEE appear prominently with each reprinted figure and/or table.
- 3) If a substantial portion of the original paper is to be used, and if you are not the senior author, also obtain the senior author's approval.

Requirements to be followed when using an entire IEEE copyrighted paper in a thesis:

- 1) The following IEEE copyright/ credit notice should be placed prominently in the references: © [year of original publication] IEEE. Reprinted, with permission, from [author names, paper title, IEEE publication title, and month/year of publication]
- 2) Only the accepted version of an IEEE copyrighted paper can be used when posting the paper or your thesis on-line.
- 3) In placing the thesis on the author's university website, please display the following message in a prominent place on the website: In reference to IEEE copyrighted material which is used with permission in this thesis, the IEEE does not endorse any of [university/educational entity's name goes here]'s products or services. Internal or personal use of this material is permitted. If interested in reprinting/republishing IEEE copyrighted material for advertising or promotional purposes or for creating new collective works for resale or redistribution, please go to http://www.ieee.org/publications_standards/publications/rights/rights_link.html to learn how to obtain a License from RightsLink.

If applicable, University Microfilms and/or ProQuest Library, or the Archives of Canada may supply single copies of the dissertation.

At the bottom of the content area, there are two buttons: "BACK" and "CLOSE".

The footer of the page contains the following text: © 2020 Copyright - All Rights Reserved | Copyright Clearance Center, Inc. | Privacy statement | Terms and Conditions
 Comments? We would like to hear from you. E-mail us at customer-care@copyright.com

The Windows taskbar at the bottom shows the search bar with "Type here to search", several application icons, and the system tray with the time "10:49 PM" and date "01-Jan-20".

Figure 11



Singh SachinKumar <singh.sachinkumar@students.iiserpune.ac.in>

Thank you for your order with RightsLink / Springer Nature

1 message

no-reply@copyright.com <no-reply@copyright.com>
 To: singh.sachinkumar@students.iiserpune.ac.in

Tue, Dec 31, 2019 at 9:39 PM

Thank you for your order!

Dear Mr. Sachin Singh,

Thank you for placing your order through Copyright Clearance Center's RightsLink[®] service.

Order Summary

Licensee: Mr. Sachin Singh
 Order Date: Dec 31, 2019
 Order Number: 4739401263188
 Publication: Nature Nanotechnology
 Title: Power generation with laterally packaged piezoelectric fine wires
 Type of Use: Thesis/Dissertation
 Order Total: 0.00 USD

View or print complete [details](#) of your order and the publisher's terms and conditions.

Sincerely,

Copyright Clearance Center

Tel: +1-855-239-3415 / +1-978-646-2777
 customercare@copyright.com
 https://myaccount.copyright.com

RightsLink[®]

Figure 12 and 13



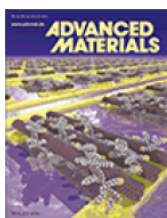
Singh SachinKumar <singh.sachinkumar@students.iiserpune.ac.in>

Thank you for your order with RightsLink / John Wiley and Sons

4 messages

 no-reply@copyright.com <no-reply@copyright.com>
 To: singh.sachinkumar@students.iiserpune.ac.in

Tue, Dec 31, 2019 at 9:07 PM



Thank you for your order!

Dear Mr. Sachin Singh,

Thank you for placing your order through Copyright Clearance Center's RightsLink® service.

Order Summary

Licensee: Mr. Sachin Singh
 Order Date: Dec 31, 2019
 Order Number: 4739390859688
 Publication: Advanced Materials
 Title: Flexible Nanogenerators for Energy Harvesting and Self-Powered Electronics
 Type of Use: Dissertation/Thesis
 Order Total: 0.00 USD

View or print complete [details](#) of your order and the publisher's terms and conditions.

Sincerely,

Copyright Clearance Center

Tel: +1-855-239-3415 / +1-978-646-2777
 customercare@copyright.com
 https://myaccount.copyright.com



RightsLink®

Figure 14



The screenshot displays the Copyright Clearance Center RightsLink interface. At the top left is the Copyright Clearance Center logo. To its right is the RightsLink logo. The navigation bar includes links for Home, Help, Email Support, and a user profile for Sachin Singh. The main content area features a box for the article "Quantifying the triboelectric series" by Haiyang Zou et al., published in Nature Communications by Springer Nature on March 29, 2019. Below this is a Creative Commons section explaining the CC BY license and providing contact information for Springer Nature.

Copyright Clearance Center
RightsLink®

Home Help Email Support Sachin Singh ▾

SPRINGER NATURE

Quantifying the triboelectric series
Author: Haiyang Zou et al
Publication: Nature Communications
Publisher: Springer Nature
Date: Mar 29, 2019
Copyright © 2019, Springer Nature

Creative Commons
This is an open access article distributed under the terms of the [Creative Commons CC BY](#) license, which permits unrestricted use, distribution, and reproduction in any medium, provided the original work is properly cited.
You are not required to obtain permission to reuse this article.
To request permission for a type of use not listed, please contact [Springer Nature](#)

© 2019 Copyright - All Rights Reserved | [Copyright Clearance Center, Inc.](#) | [Privacy statement](#) | [Terms and Conditions](#)
Comments? We would like to hear from you. E-mail us at customercare@copyright.com

Figure 15

To: singh.sachinkumar@students.iiserpune.ac.in



Thank you for your order!

Dear Mr. Sachin Singh,

Thank you for placing your order through Copyright Clearance Center's RightsLink® service.

Order Summary

Licensee: Mr. Sachin Singh
Order Date: Dec 31, 2019
Order Number: 4739420612125
Publication: Advanced Energy Materials
Title: Triboelectric Nanogenerators Driven Self-Powered Electrochemical Processes for Energy and Environmental Science
Type of Use: Dissertation/Thesis
Order Total: 0.00 USD

View or print complete [details](#) of your order and the publisher's terms and conditions.

Sincerely,

Copyright Clearance Center

Tel: +1-855-239-3415 / +1-978-646-2777
customer@copyright.com
<https://myaccount.copyright.com>



RightsLink®

Figure 17



Singh SachinKumar <singh.sachinkumar@students.iiserpune.ac.in>

Thank you for your order with RightsLink / Elsevier

no-reply@copyright.com <no-reply@copyright.com>
To: singh.sachinkumar@students.iiserpune.ac.in

Tue, Dec 31, 2019 at 10:42 PM



Thank you for your order!

Dear Mr. Sachin Singh,

Thank you for placing your order through Copyright Clearance Center's RightsLink® service.

Order Summary

Licensee: Mr. Sachin Singh
Order Date: Dec 31, 2019
Order Number: 4739430506682
Publication: Nano Energy
Title: Nanogenerators, self-powered systems, blue energy, piezotronics and piezo-phototronics – A recall on the original thoughts for coining these fields
Type of Use: reuse in a thesis/dissertation
Order Total: 0.00 USD

[View or print complete details](#) of your order and the publisher's terms and conditions.

Sincerely,

Copyright Clearance Center

Figure 18



Singh SachinKumar <singh.sachinkumar@students.iiserpune.ac.in>

Thank you for your order with RightsLink / John Wiley and Sons

no-reply@copyright.com <no-reply@copyright.com>
To: singh.sachinkumar@students.iiserpune.ac.in

Tue, Dec 31, 2019 at 10:27 PM

**Thank you for your order!**

Dear Mr. Sachin Singh,

Thank you for placing your order through Copyright Clearance Center's RightsLink® service.

Order Summary

Licensee: Mr. Sachin Singh
Order Date: Dec 31, 2019
Order Number: 4739421169428
Publication: Advanced Energy Materials
Title: Triboelectric Nanogenerator: A Foundation of the Energy for the New Era
Type of Use: Dissertation/Thesis
Order Total: 0.00 USD

View or print complete [details](#) of your order and the publisher's terms and conditions.

Sincerely,

Chapter 2

New Tab x | Gmail x | Gmail x | Verification x | Metallic Int x | Sachin Kum x | High powe x | New Tab x | IISER, Pune x | + -

pubs.rsc.org/en/content/articlelanding/2019/se/c9se00267g#divAbstract

High power mechanical energy harvester based on exfoliated black phosphorous-polymer composite and its multiple applications†

Sachin Kumar Singh^{a*}, Subas Muduli^b, Dijo Dhakras^c, Rina Pandey^c, Rohit Babar^c, Ankur Singh^b, Dinesh Kabra^d, Mukul Kabir^e, Ramamoorthy Boomishankar^{f*} and Satishchandra Ogale^g

Author affiliations

Abstract

Black phosphorous (BP) and its 2D analogue phosphorene are endowed with several striking properties due to their unique puckered structure. One attribute that can potentially attract multiple applications of interest, and yet not fully addressed, is their mechano-electric response. Herein, we demonstrate the utility of an uniformly dense dispersion of few layer BP (FLBP) nanosheets in PDMS (polydimethylsiloxane) matrix, with a high 2D-dielectric interface density, exhibiting a remarkably strong mechanical energy harvesting effect. A highest peak-to-peak voltage output of about 350 V is achieved with a maximum current density of 12.8 mA m⁻² under an applied impact force of 40 N, at a frequency range of 20–25 Hz. This corresponds to a volume power density of 2 kW m⁻³ with active material (BP) contribution of 0.35 W g⁻¹. Notably, the 2D BP nanosheets themselves are found to exhibit a fairly high piezoelectric coefficient of ~20 pm V⁻¹ as revealed by the piezoresponse force microscopy (PFM). First principles DFT calculations suggest the existence of strain-induced polarization in the BP layers via deformation-induced redistribution of intra-layer electron charge density. Based on the experimental and theoretical findings, we propose a synergistic multi-polarization mechanism that contributes to the strength of the observed energy harvesting effect. We also present three interesting practical modes of energy harvesting by subjecting them to the rapid flow of water, bicycle wheel motion and tapping induced LED

High power mechanical energy harvester based on exfoliated black phosphorous-polymer composite and its multiple applications

S. K. Singh, S. Muduli, D. Dhakras, R. Pandey, R. Babar, A. Singh, D. Kabra, M. Kabir, R. Boomishankar and S. Ogale, *Sustainable Energy Fuels*, 2019, 3, 1943
DOI: 10.1039/C9SE00267G

If you are not the author of this article and you wish to reproduce material from it in a third party non-RSC publication you must [formally request permission](#) using Copyright Clearance Center. Go to our [instructions for using Copyright Clearance Center page](#) for details.

Authors contributing to RSC publications (journal articles, books or book chapters) do not need to formally request permission to reproduce material contained in this article provided that the correct acknowledgement is given with the reproduced material.

Reproduced material should be attributed as follows:

- For reproduction of material from NJC:
Reproduced from Ref. XX with permission from the Centre National de la Recherche Scientifique (CNRS) and The Royal Society of Chemistry.
- For reproduction of material from PCCP:
Reproduced from Ref. XX with permission from the PCCP Owner Societies.
- For reproduction of material from PPS:
Reproduced from Ref. XX with permission from the European Society for Photobiology, the European Photochemistry Association, and The Royal Society of Chemistry.
- For reproduction of material from all other RSC journals and

Rightlink® by C...html ^ Rensselaer Polyte...docx ^ Show all X

Type here to search

ENG IN 16:44 30-12-2019

Chapter 3

12/30/2019

Rightslink® by Copyright Clearance Center



RightsLink®



Home



Help



Email Support



Sign in



Create Account

Seed Power: Natural Seed and Electrospun Poly(vinyl difluoride) (PVDF) Nanofiber Based Triboelectric Nanogenerators with High Output Power Density

Author: Sachin Kumar Singh, Piyush Kumar, Rushikesh Magdum, et al

Publication: ACS Applied Bio Materials

Publisher: American Chemical Society

Date: Aug 1, 2019

*Copyright © 2019, American Chemical Society***PERMISSION/LICENSE IS GRANTED FOR YOUR ORDER AT NO CHARGE**

This type of permission/license, instead of the standard Terms & Conditions, is sent to you because no fee is being charged for your order. Please note the following:

- Permission is granted for your request in both print and electronic formats, and translations.
- If figures and/or tables were requested, they may be adapted or used in part.
- Please print this page for your records and send a copy of it to your publisher/graduate school.
- Appropriate credit for the requested material should be given as follows: "Reprinted (adapted) with permission from (COMPLETE REFERENCE CITATION). Copyright (YEAR) American Chemical Society." Insert appropriate information in place of the capitalized words.
- One-time permission is granted only for the use specified in your request. No additional uses are granted (such as derivative works or other editions). For any other uses, please submit a new request.

[BACK](#)[CLOSE WINDOW](#)

© 2019 Copyright - All Rights Reserved | [Copyright Clearance Center, Inc.](#) | [Privacy statement](#) | [Terms and Conditions](#)
Comments? We would like to hear from you. E-mail us at customer@copyright.com

Chapter 5

New Tab x | Gmail x | Gmail x | Verification | S | X | Metallic Intern x | Sachin Kumar x | High power m x | Nanoscale LuF x | + -

pubs.rsc.org/en/content/articlelanding/2018/nr/c8nr07825d#divAbstract

From the journal:
Nanoscale

Nanoscale LuFeO₃: shape dependent ortho/hexa-phase constitution and nanogenerator application†

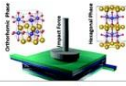
Check for updates

Smita Chaturvedi ¹, Sachin Kumar Singh ², Priyank Shyam ¹, Mandar M. Shirolkar ¹, Swathi Krishna ¹, Boomishankar ¹ and Satishchandra Ogale ¹

Author affiliations

Abstract

In multiferroic LuFeO₃ the hexagonal (-h) phase is an intermediate metastable phase encountered during the amorphous to orthorhombic (-o) transformation and is ferroelectric in nature. Thus far it has only been stabilized in a substrate-supported few layered ultrathin film form. Herein we show that the surface-induced strain field intrinsically present in nano-systems can self-stabilize this phase and the hexagonal to orthorhombic phase constitution ratio depends on the shape of the nanomaterial. Thus, nanoparticles (nanofibres) strain-stabilize the o:h ratio of about 75:25 (23:77). The inclusion of nano-LuFeO₃ into PDMS renders impressive nanogenerator performance, consistent with the ferroelectric phase content.



Nanoscale LuFeO₃: shape dependent ortho/hexa-phase constitution and nanogenerator application

S. Chaturvedi, S. K. Singh, P. Shyam, M. M. Shirolkar, S. Krishna, R. Boomishankar and S. Ogale, *Nanoscale*, 2018, **10**, 21406
DOI: 10.1039/C8NR07825D

If you are not the author of this article and you wish to reproduce material from it in a third party non-RSC publication you must [formally request permission](#) using Copyright Clearance Center. Go to our [Instructions for using Copyright Clearance Center page](#) for details.

Authors contributing to RSC publications (journal articles, books or book chapters) do not need to formally request permission to reproduce material contained in this article provided that the correct acknowledgement is given with the reproduced material.

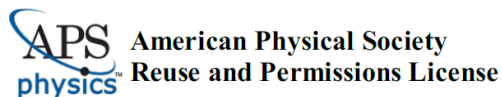
Reproduced material should be attributed as follows:

- For reproduction of material from NJC:
Reproduced from Ref. XX with permission from the Centre National de la Recherche Scientifique (CNRS) and The Royal Society of Chemistry.
- For reproduction of material from PCCP:
Reproduced from Ref. XX with permission from the PCCP Owner Societies.
- For reproduction of material from PPS:
Reproduced from Ref. XX with permission from the European Society for Photobiology, the European Photochemistry Association, and The Royal Society of Chemistry.

Rightslink® by C...html | Rensselaer Polyte...docx | Show all X

Type here to search | ENG IN | 16:50 | 30-12-2019

Chapter 5



30-Dec-2019

This license agreement between the American Physical Society ("APS") and Sachin Singh ("You") consists of your license details and the terms and conditions provided by the American Physical Society and SciPris.

Licensed Content Information

License Number: RNP/19/DEC/021501
License date: 30-Dec-2019
DOI: 10.1103/PhysRevMaterials.3.074007
Title: Coexisting 1T/2H polymorphs, reentrant resistivity behavior, and charge distribution in MoS_2 - hBN 2D/2D composite thin films
Author: Swati Parmar et al.
Publication: Physical Review Materials
Publisher: American Physical Society
Cost: USD \$ 0.00

Request Details

Does your reuse require significant modifications: No
Specify intended distribution locations: Worldwide
Reuse Category: Reuse in a thesis/dissertation
Requestor Type: Student
Items for Reuse: Whole Article
Format for Reuse: Electronic

Information about New Publication:

University/Publisher: IISER PUNE
Title of dissertation/thesis: Design and synthesis of organic and organic-inorganic hybrid device-materials for mechanical energy harvesting applications
Author(s): Sachin Kumar Singh
Expected completion date: Feb. 2019

License Requestor Information

Name: Sachin Singh
Affiliation: Individual
Email Id: singh.sachinkumar@students.iiserpune.ac.in
Country: India